MODELING AND OPTIMAL CONTROL OF RANGE EXTENDED ELECTRIC VEHICLES

by

Orhan BUĞUR

B.S., Electrical & Electronics Engineering, Boğaziçi University, 2009

Submitted to the Institute for Graduate Studies in
Science and Engineering in partial fulfillment of
the requirements for the degree of
Master of Science

Graduate Program in Electrical & Electronics Engineering
Boğaziçi University
2012

ACKNOWLEDGEMENTS

I would like to express my sincere thanks to Prof. Okyay KAYNAK for his invaluable support throughout this study. I would like to mention his excellent approach to his students, which will give me inspiration and motivation for the rest of my life.

I am greatly thankful to my parents, Nurhan and Bekir BUĞUR, and my brother Serkan BUĞUR for their never ending support and patience during my education life.

Finally, I wish to thank all my friends and colleagues for their support through the thesis.

ABSTRACT

MODELING AND OPTIMAL CONTROL OF RANGE EXTENDED ELECTRIC VEHICLES

Over the last few years, the world has started to witness a change in vehicular technology due to increasing gasoline prices and environmental concerns. Hybrid and Electric vehicles have been introduced to society. The level of usage for these vehicles is directly related to advance in battery technology and control strategies. Modern battery technology, even after recent developments, does not allow for electric vehicle (EV) ranges to be more than a couple hundred kilometers. Even though this range is statistically sufficient for more than 80% of the journeys, most drivers suffer from range anxiety which in turn prevents EVs from becoming a viable option. As a solution, Range Extended Electric Vehicle (REEV) has been proposed. REEV has the same architecture as a Series Hybrid Electric Vehicle (SHEV) which is one of the main hybrid vehicle architectures. In SHEVs, 100% of the propulsion is provided by an Electric Motor (EM). When the state of charge (SOC) of the battery reaches low levels, the electricity necessary for the operation of EM is supplied by a generator which is driven by an Internal Combustion Engine (ICE). The main goal of this thesis is to develop, by the use of contemporary IT methodologies, a novel optimal control strategy for REEVs in order to offer better energy management and/or component life. The project can therefore roughly be divided in 2 parts, Range Extended Electric Vehicle modeling and implementation of optimal controller for energy management problem.

ÖZET

MENZİLİ UZATILMIŞ ELEKTRİKLİ ARAÇLARIN MODELLEMESİ VE OPTİMAL KONTROLÜ

Artan petrol fiyatları ve çevresel etkiler nedeniyle son yıllarda araç teknolojisinde birçok yenilik ortaya çıkmıştır. Hibrit ve elektrikli araçların kullanımı yaygınlaşmıştır. Elektrikli araçlar her ne kadar yaygınlaştıysalar da batarya teknolojisinin kısıtlamaları nedeniyle benzinli ve dizel araçlarla yarışacak düzeye gelememişlerdir. Bunun önemli sebeplerinden biri de elektrikli araçların yaygınlaşmasıyla ortaya çıkan "menzil kaygısı"dır. Menzil kaygısını ortadan kaldırmak için ortaya atılan çözümlerden birisi, içten yanmalı motor ve jeneratörden oluşan menzil uzatıcı üniteler aracılığıyla bataryanın gerektiğinde şarj edilmesidir. Menzil uzatıcı ünitenin tekerleklere herhangi bağlantısı yoktur, sadece batarya aracılığıyla elektriksel güç takviyesi yapabilir. Bu nedenle menzili uzatılmış araçlar, seri hibrit elekrikli araçlarla aynı mimariye sahiptir. Tezde seri hibrit araçların modellenmesi ve enerji verimliliğini azami seviyeye çıkaracak optimal kontrolcü tasarımı anlatılacaktır.

TABLE OF CONTENTS

LIST OF FIGURES

LIST OF TABLES

LIST OF SYMBOLS

C_{nom}	Nominal charge of the battery
C_{tl}	Capacitance value for long time constant
C_{ts}	Capacitance value for short time constant
d	Desired full electric range for RE-EV
DoD	Depth of discharge
E_{avg}	Average energy per unit distance
E_{nom}	Nominal energy of the battery
$E_{specific}$	Specific energy of the battery Wh/kg
I_d	Stator current d-axis component
I_q	Stator currents q-axis component
L_d	Magnetizing inductance components for d axis
LIFE	Number of cycles in life at given DoD
$LIFE_{zero}$	Number of cycles in life at zero DoD
L_q	Magnetizing inductance components for q axis
m	Slope of natural logarithm of LIFE/ $LIFE_{zero}$ versus DoD
$M_{battery}$	Mass of the battery
p	Number of pole pairs
$P_{battery}$	Required battery power during the simulation
P_{peak}	Peak power
P_{RE}	Power from RE
$P_{specific}$	Specific power of the battery W/kg
R_s	Stator resistance
R_{series}	Internal resistance of the battery, models instantaneous voltage drop
R_{tl}	Resistance value for long time constant
R_{ts}	Resistance value for short time constant
S_{total}	Total driving distance
V_d	Stator voltage component of d axis
V_q	Stator voltage component of q axis

β	Angle of stator current to direct axis
$\eta(P_{RE})$	Overall efficiency of the RE
$\eta_{battery}$	Average efficiency of battery
$\eta_{batterypeak}$	Efficiency of battery at maximum power
$\eta_{charging}$	Charging efficiency
η_{grid}	Average grid efficiency for electricity generation
θ_L	Angle of overall flux linkage vector to direct axis
ψ_d	Flux linkage due to d-axis current ($\psi_d = L_d\, i_d$)
ψ_M	Flux linkage of the permanent magnets
ψ_q	Flux linkage due to q-axis current ($\psi_q = L_q\, i_q$)
ψ_S	Total flux linkage
ω	Electrical speed
ω_m	Mechanical speed(rotor speed)

LIST OF ACRONYMS / ABBREVIATIONS

AC	Alternating Current
AER	All Electric Range
CI	Compression Ignition
DC	Direct Current
DOD	Depth of Discharge
DP	Dynamic Programming
EM	Electric Motor/Machine
EV	Electric Vehicle
FOC	Field Oriented Control
GIS	Geographical Information System
GPS	Global Positioning System
HEV	Hybrid Electric Vehicle
ICE	Internal Combustion Engine
IM	Induction Machine
IPM	Interior Permanent Magnet Synchronous Machine
Li-ion	Lithium Ion
MPTF	Maximum Torque Per Flux
MTPA	Maximum Torque Per Ampere
NEDC	New European Drive Cycle
PHEV	Plug-in Hybrid Electric Vehicle
PMSM	Permanent Magnet Synchronous Machine
RE	Range Extender
REEV	Range Extended Electric Vehicle
SHEV	Series Hybrid Electric Vehicle
SI	Spark Ignition
SIPM	Surface Inset Permanent Magnet Synchronous Machine
SMPC	Stochastic Model Predictive Control
SOC	State of Charge
SOH	State of Health
SPM	Surface Mounted Permanent Magnet Synchronous Machine

SRM	Switched Reluctance Machine
SVPWM	Space Vector Pulse Width Modulation

1. INTRODUCTION

Air pollution caused by increased greenhouse gas emissions is a serious problem of today's world and one of the largest sources of greenhouse gas emissions is transportation sector. Although greenhouse emissions per unit distance travelled have decreased due to advances in vehicular technology, emissions caused by transportation sector have increased rapidly in the last few years because of increased private transportation [1].

Increasing gasoline prices along with environmental issues are forcing automotive industry to a change in vehicular technology, which shall reduce fossil based fuel consumption. At the time, electric vehicles (EV) are the most promising and feasible solution to the addressed problems. In EVs, propulsion is provided by an electric motor and electrical energy is stored by a battery.

However modern battery technology, even after recent developments, does not allow for all electric ranges (AER) more than a couple hundred kilometers. Even though this range is statistically sufficient for more than 80% of the daily journeys, there has to be a solution for the long journeys in order to make EVs as a viable option, since no one would like to keep a second car just for long trips. Yet another issue called "Range Anxiety" prevents EVs from becoming a viable option, which is caused by the uncertainty in available battery energy estimation. Most drivers do not prefer EVs just because of range anxiety. Anxiety can be solved simply by adding a secondary power source to the vehicle, which shall provide necessary electrical energy when energy level is too low or battery cannot supply power for some other reason.

The concept of separate two power sources, one being battery, indicates hybrid electric vehicle (HEV) architecture. HEVs that can use grid electricity are called plug-in HEVs (PHEV), where battery energy allows reasonable ranges on its own. Mentioned configuration in previous paragraph, is a type of PHEV called Range Extended EVs (REEV). Other than being plug-in or not, HEVs are classified according to power source that supplies traction. Mainly there are 3 HEV architectures, which are:

- Parallel: Electric motor and an internal combustion engine (ICE) provide traction, where both of them can provide torque at the same time or one of them is disengaged and other one supplies traction torque on its own.
- Series: Electric motor is the only source of traction torque, where ICE has no mechanical connection to drive shaft but to a generator. ICE and generator set is only responsible for supplying electrical energy. Size of the battery in a series hybrid electric vehicle (SHEV) introduces a degree of freedom, which allows ICE-generator set can operate at optimal points.
- Series-Parallel: Combination of series and parallel architecture. Traction torque can be supplied by ICE, electric motor and even generator. It has a complex power splitting gearbox, which enables switching between series and parallel architectures.

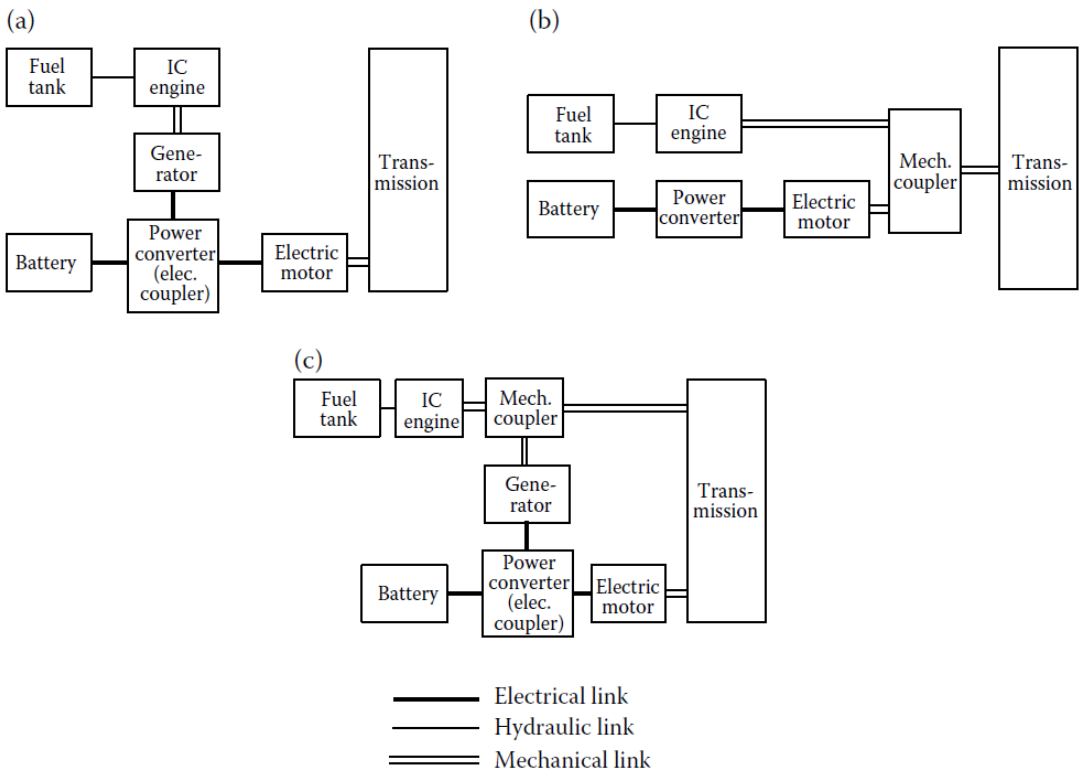

Figure 1.1. (a) Series architecture (b) Parallel architecture (c) Series-parallel architecture [2].

REEVs have the same architecture as SHEVs, only with a much larger battery such that ICE-generator set no longer acts as a primary power source but as an emergency or

supplementary power source. ICE-generator set is sometimes called auxiliary power unit (APU), but more common way of saying in literature is “Range Extender”.

Expected AER of a REEV shall be determined, keeping in mind that it should be sufficient for more than 80-90% of all journeys. Using statistical data, minimum acceptable AER is determined as 100-150km, whereas extended range should be at least 500km. Battery energy, maximum battery and electric motor powers determine AER of REEV along with vehicle parameters and drive cycle. Maximum power available by RE unit depends on vehicle parameters and extreme drive cycle, since maximum traction power can be determined from vehicle parameters and extreme drive cycle. Finally size of the fuel tank depends on the extended range. Also the efficiency of the vehicle depends heavily on the size of the battery, electric motor and RE. Larger battery, electric motor or ICE can be selected for better efficiency. Over a distribution of drive cycles, operating region must coincide with highest efficiency region of the component.

Energy capacity and power limits of the battery depend on the size and the type of the battery. Higher energy capacity of a battery results in increased weight. Power limit of the battery determines the acceleration limit and performance of the EV. Also the efficiency of the regenerative braking is determined by the power limit of the electric motor and battery. Maximum power of the electric motor determines the acceleration limit and the maximum regenerative power of the EV. The type of the electric motor is also important such that efficiency for given speed and torque alters significantly. Type of ICE is important in the sense of fuel economy and energy efficiency. The possible selections are rotary Wankel engine, otto 4-cycle 2-cylinder or diesel 4-cycle 2-cylinder. Optimal component sizes are used from QSS toolbox [3] after assuming use of internal permanent magnet synchronous machine as electric motor and Li-ion battery.

The main goal of this thesis is to develop, by the use of contemporary IT methodologies, an optimal control strategy for REEVs in order to offer better energy management and/or component life. The project can therefore roughly be divided in two parts, which are the following:

- Dynamic battery, electric motor and vehicle models are developed for designing local controllers.
- Objective function derivation for energy management and implementation of optimal controller which minimizes overall energy loss over a drive cycle by controlling power of range extender unit.

Supervisory control strategy is used for designing the optimal controller, which requires use of simple models in order to determine power reference for each subsystem. Local controllers are used at subsystems for tracking power references determined by supervisory controller. Such an example is ICE-generator set (RE unit); optimal power output of RE is calculated by the supervisory controller and then optimal operating point, torque versus speed, of ICE and generator is determined by the local controller. Several optimal control techniques are developed for HEVs, where some of them are sub-optimal solutions and can be implemented online. Others are global optimal solutions but require priori knowledge of drive cycle.

Application of pontryagin's minimum principle for minimizing total CO_2 emissions of a series-parallel HEV is presented in [4]. Optimal torque split between three different sources of mechanical energy is calculated for a given driver torque demand. Dynamic programming (DP) solution to fuel minimization problem is presented in [6], where drive cycle is constructed using Global Positioning System (GPS), Geographical Information System (GIS) and traffic flow modeling. Global optimal solution is obtained for drive cycle calculated from GPS, GIS and traffic flow data [6]. Time independent, online implementable, sub-optimal control for a series hybrid electric vehicle is presented in [7], where control input is the power split factor between auxiliary power unit (ICE-generator set) and battery. A stochastic approach is presented in [8], where future power demand of the driver is modeled as Markov chain and stochastic model predictive control (SMPC) approach is used for obtaining optimal power split between battery and auxiliary power unit. SMPC can be solved with quadratic programming; hence it is online implementable. Equivalent consumption minimization strategy shows close solutions to global optimum and it can be implemented online [5]. It is based on an equivalence factor between fuel and electrical energy, which enables optimal solution for variable State of Charge (SOC).

Optimal controller proposed in this thesis is a synthesis of one presented by [5] and [6]. For the proposed system, state of the system is the SOC level of the battery and control input is the RE power. Driver power demand is modeled as a disturbance coming from the dynamic vehicle model.

Dynamic programming approach is used for minimizing overall energy consumption from well to wheel. Fuel power efficiency is calculated by utilizing engine efficiency maps, whereas a variable is assigned for representing the efficiency of the grid power. Grid power efficiency is combination of average electricity generation efficiency and electricity transmission efficiency. Supervisory controller minimizes the fuel consumption over the drive cycle, where final state cost is associated to battery energy level. Final state cost is zero if initial and final battery energy levels are the same. Final state cost is assigned a negative value if final SOC is larger than initial. Drive cycle is accepted as NEDC for implementing and testing the performance of the controller.

2. VEHICLE MODELING

Dynamic model for a series hybrid vehicle is constructed as shown in Figure 2.1. Bond graph modeling technique is used, where connections between components represent bi-directional energy flow, either current times voltage or torque times angular speed. Usage of bond graph technique simplifies the power flow and efficiency equations.

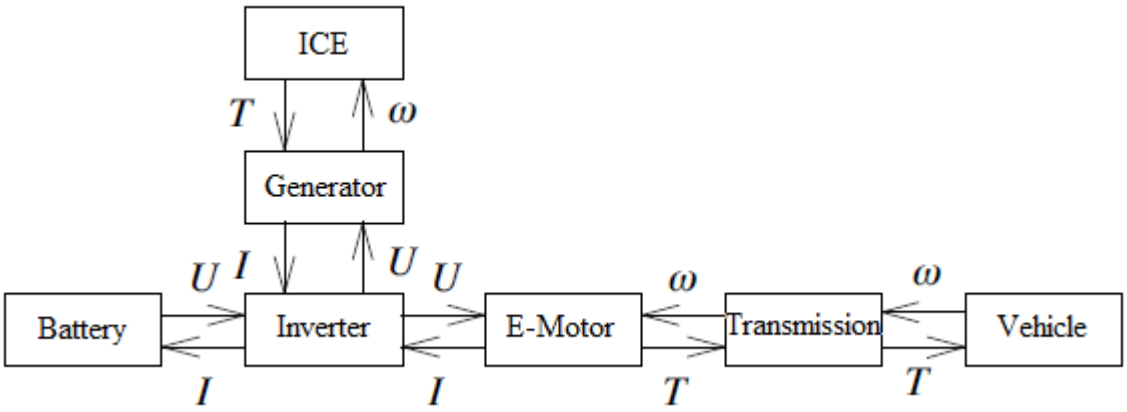

Figure 2.1. Dynamic SHEV model, I: Current, U: Voltage, T: Torque, ω: Angular speed.

Vehicle model in Figure 2.1 is constructed by 5 major components, which are:

- Battery Model: 25kWh Li-ion battery
- Electric Motor Model: Permanent Magnet Synchronous Machine Model and
- Range Extender Model: Consists of ICE and generator model, due to high complexity, dynamic ICE model is replaced with a quasi-static model [3].
- Inverter Model: SVPWM controlled inverter model used for calculating power loss
- Vehicle Model: Dynamic model capable of modeling longitudinal dynamics of the vehicle.

2.1 Battery

Today, most fundamental issue regarding EVs and HEVs is problem of portable source of electrical energy. Batteries, among other alternatives, have been the most popular on-board energy source for EVs and HEVs [10]. Battery technology can be addressed as the bottleneck of EV and HEV market, since high cost and relatively low performance of today's batteries are the main reason for the delayed spread of EVs and HEVs.

In most of the EV and HEV applications, batteries consist of several battery cells which store electrical energy in the form of potential chemical energy. Each cell consists of a cathode and an anode with electrolyte solution between them, depending on the type of the cell there may be other major components. Charge and discharge are achieved by reversible reactions between anode, cathode and electrolyte. Figure 2.2 shows common cell structure, in this case for Lithium-ion.

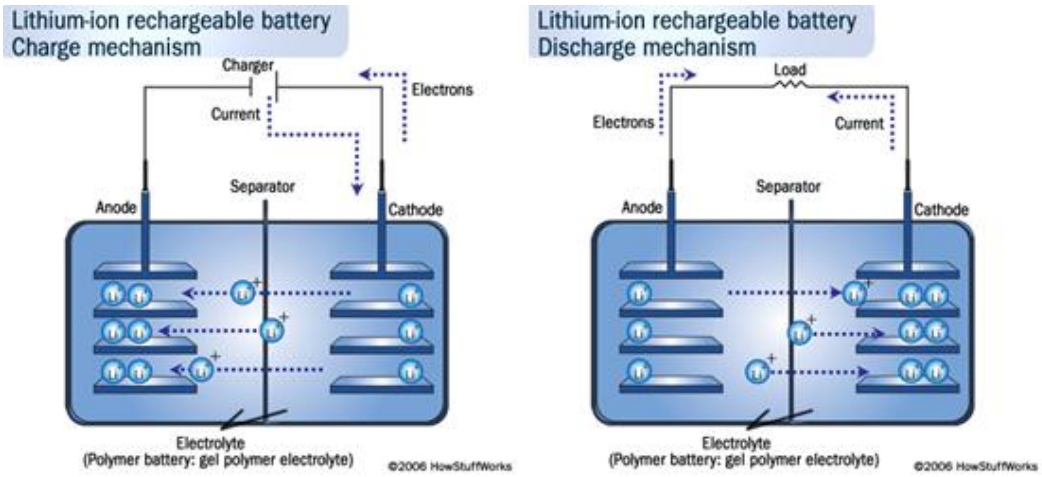

Figure 2.2. Lithium-ion cell structure, charging and discharging [9].

Various types of battery cells available on market are compared using some significant specifications such as:

- Specific energy: Amount of stored energy per unit mass (Wh/kg).
- Specific power: Maximum available power per unit mass (W/kg).

- Calendar life: Period of time before performance of a battery diminishes significantly, whether by active or inactive usage.
- Cycle life: Number of charge & discharge cycles that battery can withstand before performance of battery diminishes significantly. (i.e.: 1500 cycles for 80% Depth of Discharge)
- Charge acceptance rate: Ratio of energy stored inside the battery to energy delivered to the terminals of battery, $f_{Charge\_Acceptance}$ (I, SOC, T…).
- Discharge efficiency: Ratio of energy transferred to terminals of battery to energy extracted from the battery, $f_{Discharge\_Efficiency}$ (I, SOC, T…).
- Temperature effects: How the temperature effects other parameters of the battery.
- Output voltage: Voltage across terminals depends on the chemical reaction, so much or less determinate for a cell type.

EV and HEV applications require high specific energy which determines full electric range of the HEV. High specific power assures drivability and safety, since operating near limits of the battery for very long drive cycles may risk safety of the battery hence vehicle. REEV may experience very long drive cycles, so high specific power becomes one of the most significant features.

U.S. Advanced Battery Consortium have defined some performance and cost goals for batteries, prerequisites for battery powered vehicles to compete internal combustion vehicles: “The specific energy should increase from 100-125 to 150 or even 200 Wh/kg and the costs decrease from 700-1200 to 250 $/kWh or lower” [15]. In Figure 2.3, specific power versus specific energy for different types of battery cells that are used in HEV applications are shown.

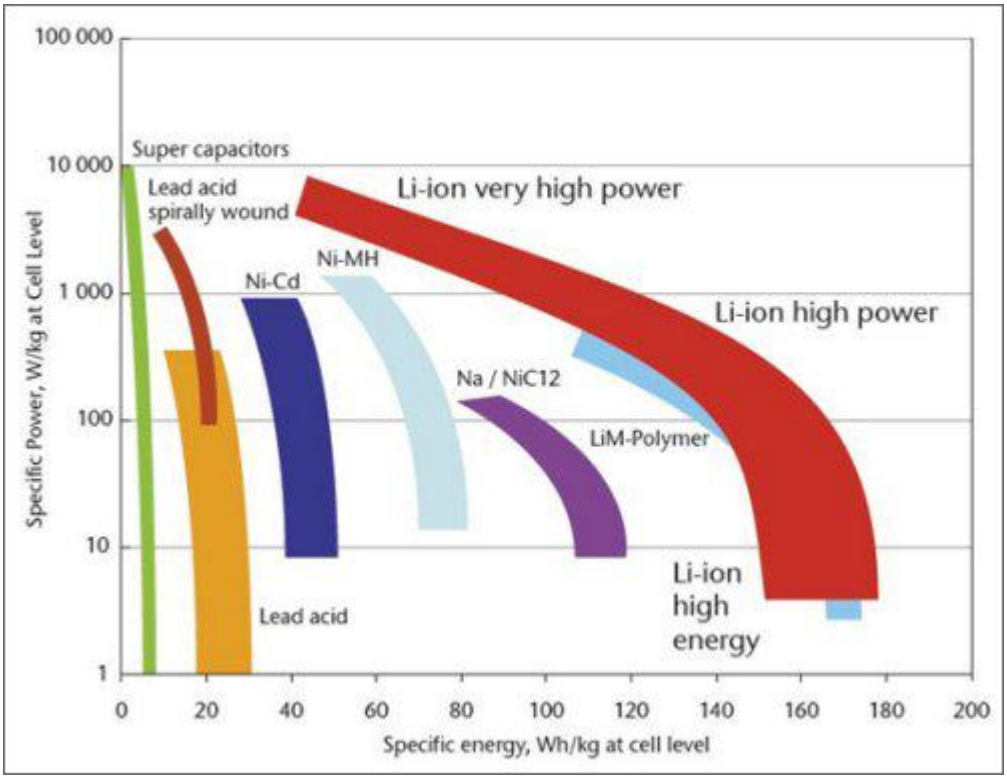

Figure 2.3. Specific power – Specific energy regions for various cell technologies.

Long calendar life and long cycle life are other expected features which determine maximum expected service of the HEVs in terms of years of usage or kilometers before battery replacement. Charging and regenerative braking efficiency rely mostly on charge acceptance rate which depends on temperature among other states such as SOC of the battery. Range of the vehicle is determined by discharge efficiency, which depends mostly on battery states such as SOC, current and temperature. Function of dependency of discharge efficiency on battery states vary significantly among different cell types (i.e. Discharge efficiency reduces more significantly in NiMH than Li-ion as discharge current increases).

Temperature effect is another important feature such that nearly all other specifications are affected by it. Cooling systems that are more expensive and consume more power should be installed for cell types whose performance is influenced significantly by temperature.

Cell voltage is another important factor that in current HEV and EV applications high voltage bus is formed by series configuration of cells. The number of cells in series increase as cell voltage decreases, which in return adds up to the overall internal resistance hence efficiency of the battery.

2.1.1 Battery Types

Lead-acid is the oldest battery technology with history of one and a half century. Lead-acid cell voltage is about 2V. These batteries use metallic lead as anode and lead-dioxide as cathode. During discharge, electrodes are converted to lead sulfate since sulfuric acid solution is used as electrolyte in lead-acid batteries. Special type of lead-acid batteries, valve regulated lead acid is proven to provide safe and maintenance free operation for EV and HEV applications [16]. Even though lead-acid batteries are the cheapest available battery type suitable for EV applications, they have good cycle life and high specific power. Low specific energy, 30-40 Wh/kg, and low calendar life, 3-5 years, of lead-acid batteries prevent them from widespread in EV applications. However they are considered by many researchers for micro HEV applications.

Nickel-cadmium (NiCd), aside from being a 80 year old technology, have many advantages such as long cycle life, high specific power, electrical and mechanical safety and durability, wide operating temperature (-40 °C) and small voltage drop for large currents [4]. Disadvantages are cost, nearly 4 times lead-acid, toxicity and low cell voltage which is about 1.3V. Most important drawback of this battery technology is so called memory effect, which means if battery is cycled many times to a certain SOC, in time cut-off voltage shifts to that SOC level [12]. It can be observed in Figure 2.4.

Nickel-metal-hydride (NiMH), batteries rely on release and absorption of (OH^-) by nickel oxide anode and metal hydride cathode with alkaline electrolyte such as potassium hydroxide [9,16]. It has similar characteristics to NiCd, except toxicity. Like NiCd, these batteries suffer from lazy effect, which is similar to memory effect but with less significant consequences, which can be observed in Figure 2.4. The specific energy of NiMH batteries, which is about 60-70 Wh/kg along with high nickel prices prevent this technology from becoming widespread in EV and HEV applications.

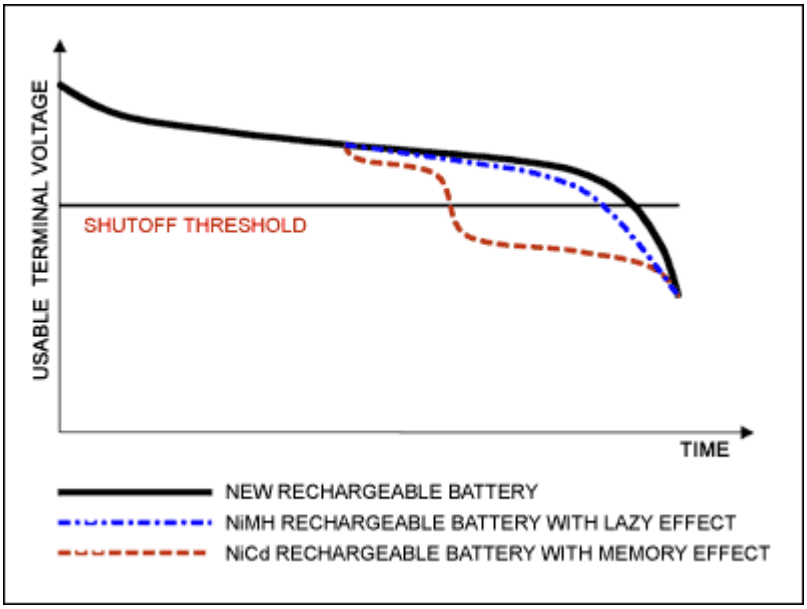

Figure 2.4. Memory and Lazy effect for NiCd and NiMH batteries [9].

Lithium-ion (Li-ion) operates such that during discharge, Lithium ions (Li^+) migrate from negative electrode to positive electrode through non-aqueous electrolyte and separator diaphragm. Lithium absorbed carbons (Li_xC) in the form of graphite are used as negative electrode since graphite can hold lithium ions as LiC_6 composition. For positive electrode, lithium is absorbed by crystal lattice of cobalt forming LiCoO2. Chemical reactions for a lithium-ion cell are shown below [9], where $0 < x < 1$.

Positive electrode reaction (charging from left to right):

$$\mathrm{LiCoO_2} \leftrightarrows \mathrm{Li_{1-x}CoO_2} + x\mathrm{Li^+} + x\mathrm{e^-}$$

Negative electrode reaction (charging from left to right):

$$x\mathrm{Li^+} + x\mathrm{e^-} + 6\mathrm{C} \leftrightarrows \mathrm{Li_xC_6}$$

Lithium-ion batteries have good specific energy and power along with good performance in high temperatures. These batteries do not suffer from memory effect and have low self-discharge. Their cell voltages can be as high as 4 Volts. Above mentioned advantages along with cost levels which become tolerable enough in last few years, allow Li-ion technology to get the largest share in EV and HEV market. Specifications of most common Li-ion battery types can be seen in Table 1.

There are several drawbacks of Li-ion technology, most of which can be passed over with proper management of the battery [12-14]. The issues can be listed as:

- Operating near very low and very high SOC shall not be allowed, depth of cycles shall be kept as low as possible.
- High temperature operation shall not exceed specified time period, else it may lead to battery degradation.
- Low temperature decreases power capacity of Li-ion cells.

In order to avoid permanent loss of battery capacity and to assure optimum operation, a battery model that is capable of estimating state of charge, state of health and state of function is necessary.

Lithium-metal-polymer (LMP) batteries use metallic lithium instead of lithium intercalated material, which is the main difference from Li-ion battery. Basically lithium ions migrate to negative electrode and form metallic lithium via reduction reaction. Higher specific energy is expected due to the usage of metallic lithium. However available LMP batteries with specific energy level around 100 Wh/kg, show no improvement compared to conventional Li-ion batteries [16].

Lithium-sulfur (Li-S) batteries utilize cathodes that are formed by pairing sulfur with carbon, whereas anode can be metallic lithium or any suitable material. Demonstrated specific energy levels are highest compared to other technologies with 350 Wh/kg. However, other features such as specific power, cycle life, efficiency and calendar life need to be improved before usage in EV and HEV industry [16].

Lithium-air (Li-air) batteries rely on oxidation of lithium at anode and reduction of oxygen from ambient air at the cathode. High specific energy levels are demonstrated, 260 Wh/kg. However, other features such as specific power, cycle life, efficiency and calendar life need to be improved [16,9].

Zinc-air batteries rely on zinc in the form of liquid slurry as anode [16]. Level of development is significantly ahead of others, making zinc-air a promising future solution for EV applications. Limiting feature is specific power that in current EV applications, it can drop down to 100 W/kg during deep cycles [10]. Demonstrated specific energy is around 200 Wh/kg.

Table 1.1. Specifications of various battery types.

Battery Type		Specific Energy(Wh/kg)	Specific Power(W/kg)	Cycle life	Cell Voltage(V)	Cost ($/kWh)
Lead-acid		25-40	75-130	200-400	2	~ 75
NiCd		35-65	50-200	400-1200	1.3	~ 100
NiMH		50-90	150-250	600-1500	1.2	100 - 300
Li-ion		100 - 220	300	400-1200		700 - 1200
Li-ion	$LiCoO_2$	165			3.7	
	$LiMn_2O_4$	110			4	
	$LiNiO_2$				3.5	
	$LiFePO_4$	110			3.3	
	Li_2FePO_4				3.6	

2.1.2 Battery Selection

In short term, Li-ion is expected to dominate the market with good enough specific energy and power. Even though prices are not competitive to ICEVs, they are at acceptable levels. Li-air, Li-S and Zinc-air may become good options in the future in the long term. However, due to their level of development many authors believe Li-ions will dominate the market also in medium term [16].

For the energy management problem we are dealing with we decided to use either 2200mAh [17] Li-ion or 850mAh [13] polymer Li-ion. The size of the battery, number of series and parallel cells, are determined using average required energy per km (E_{avg}) and desired full electric range using formulas. E_{avg} is determined using vehicle simulation for NEDC using Equation 2.1.

$$E_{avg} = \frac{\int_{t_0}^{t_f} P_{battery}}{S_{total}} \tag{2.1}$$

$$C_{battery} = \frac{E_{avg}.d}{DoD.\eta_{battery}} \quad (2.2)$$

$$M_{battery} = \frac{C_{battery}}{E_{specific}} \quad (2.3)$$

The calculations are made under assumption that specific energy is decisive for battery weight and capacity. However, conditions for specific power limits shall also be checked using Equation 2.4.

$$M_{battery} \geq \frac{P_{peak}}{P_{specific} \cdot \eta_{batterypeak}} \quad (2.4)$$

where, E_{avg} is the average energy per unit distance, d is desired full electric range for RE-EV, $E_{specific}$ is the specific energy of the battery Wh/kg, S_{total} is the total driving distance, $P_{battery}$ is the required battery power during the simulation, $\eta_{battery}$ is the average efficiency of battery, $\eta_{batterypeak}$ is the efficiency of battery at maximum power, $P_{specific}$ is the specific power of the battery W/kg, P_{peak} is the peak power, DoD is the depth of discharge and $M_{battery}$ is the mass of the battery.

Simulation results yield that E_{avg} is around 200 Wh/km. As we demand 100 km full electric range for our RE-EV, usable battery capacity (E_{avg} times *d*) can be calculated as 20kWh. Accepting DoD as 80% and average battery efficiency as 90%, physical battery capacity ($C_{battery}$) is calculated using Equations 2.2 and 2.3 to be around 27.8 kWh.

If we decide to use 0.85Ah – 4.1V [13] polymer Li-ion cell, battery will be formed with 130 cells in series and 60 modules in parallel. Whereas if we use 2.2Ah – 3.7V [17] Li-ion cell, battery shall be formed with 125 cells in series and 25 modules in parallel, for similar DC bus voltage ~500V.

2.1.3 Dynamic Battery Model

EV and HEV applications require several models for predicting different features of the battery. Most of the HEVs that are either on the market or will be in the near future possess following models for purposes of better efficiency or safety:

- State of charge(SOC) model
- State of health(SOH) model
- State of function(SOF) model
- Temperature model

Even though all of the above models have to be successfully implemented before allowing a prototype vehicle on a public road, SOC and SOF modeling shall be considered for optimal energy management. Effect of SOC and SOF on energy efficiency is much more significant than others in short and medium term.

Effect of temperature on battery performance is also important, such that important parameters of battery such as internal resistance, discharge rate, charge & discharge efficiency show significant variance due to temperature of the cell. However we will assume a perfect cooling system is installed on the vehicle and will skip modeling effects of temperature at this time.

Equivalent circuit model will be used for estimating SOC and SOF of the battery. Extending the equivalent circuit model shown in Figure 2.5 in a manner that resistance and capacitances depend on SOC will serve the purpose of binding SOC and SOF estimation.

R_{series} represents internal resistance of the battery, models instantaneous voltage drop. R_{ts} & C_{ts} are used for modeling short time constant. R_{tl} & C_{tl} are used for modeling long time constant.

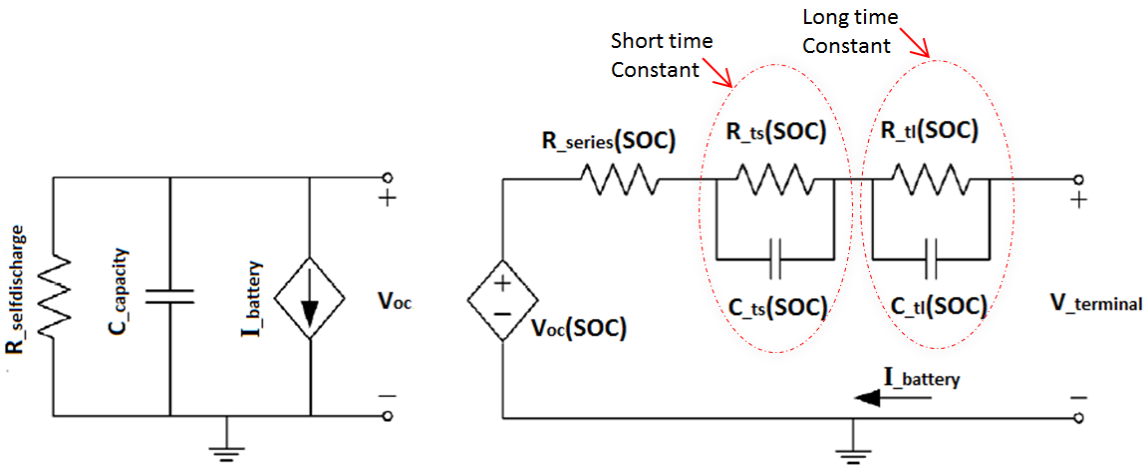

Figure 2.5. Equivalent circuit model for Li-ion battery [13,14].

All parameters in equivalent circuit model are actually functions of SOC, temperature and even cycle history. We accept these parameters as a function of SOC only since, constant temperature operation is assumed and only short term responses are desired. Battery capacity is function of temperature, current and cycle history. However it is assumed constant for energy optimal solution. Battery capacity can be modeled as function of temperature and current history in order to preserve battery capacity through optimal control of range extender for battery life extension.

$R_{self\text{-}discharge}$ is a function of SOC and temperature and is used for modeling energy loss of the battery when battery is stored for a long time. It can be simplified as a large resistor, but due to insignificant short-term effects, it can be ignored for energy optimal solutions.

Although there are several methods to estimate SOC of a battery, equivalent circuit model imposes use of current integration model. Only problem with current integration method is that even small errors in estimation may lead to a significant drift from reality in the long run, since error is integrated as well.

There are some other models which employ usage of stochastic models and Kalman filter. These models account for measurement errors while estimating SOC as well as cycle history. However, complex solutions are not desirable at the moment. General form of SOC estimation via current integration is given in Equation 2.5.

$$SOC\left[i_{bat}(t), T(t), n_{cycle}, t\right] = \quad SOC_{initial} + \frac{1}{C_{cap}} \int_0^t f_1[i_{bat}(t)] \times f_2[T(t)] \times f_3[n_{cycle}] \times i_{bat}(t)dt \tag{2.5}$$

SOC estimation becomes as given by Equation 2.6 after neglecting charge acceptance functions f_1, f_2 and f_3 which are dependent on current, temperature and cycle history respectively. Power loss is modeled as dissipated power by resistances.

$$SOC[i_{bat}(t), t] = SOC_{initial} + \frac{1}{C_{cap}} \int_0^t \left[i_{bat}(t) - \frac{P_{loss}}{V_{terminal}}\right] dt \tag{2.6}$$

Change of terminal voltage under current is modeled using two different time constants. Voltages on capacitances, which are used for modeling time constants are given by Equations 2.7, 2.8 and 2.9.

$$V_{C_{ts}} = \frac{1}{C_{ts}} \int_0^t \left[i_{R_{ts}}(t) - i_{bat}(t)\right] \tag{2.7}$$

$$V_{C_{tl}} = \frac{1}{C_{tl}} \int_0^t \left[i_{R_{tl}}(t) - i_{bat}(t)\right] \tag{2.8}$$

$$\begin{bmatrix} \dot{V_{C_{ts}}} \\ \dot{V_{C_{tl}}} \end{bmatrix} = \begin{bmatrix} (R_{ts}C_{ts})^{-1} & 0 \\ 0 & (R_{tl}C_{tl})^{-1} \end{bmatrix} \begin{bmatrix} V_{C_{ts}} \\ V_{C_{tl}} \end{bmatrix} + \begin{bmatrix} -{C_{ts}}^{-1} \\ -{C_{tl}}^{-1} \end{bmatrix} I_{bat} \tag{2.9}$$

Terminal voltage is given by Equation 2.10, which is open circuit voltage subtracted by voltage drop caused by series resistance and two RC couples (long & short).

$$V_{terminal} = V_{oc}(SOC) - i_{bat}(t) \times R_{series}(SOC) - V_{C_{ts}}(SOC, i_{bat}(t)) - V_{C_{tl}}(SOC, i_{bat}(t)) \tag{2.10}$$

The procedure of obtaining resistance and capacitance values from test data can be found in [10]. Open circuit voltage (V_{oc}), series resistance (R_{series}) and parameters of time constants (R_{ts}, C_{ts}, R_{tl}, C_{tl}) can be fitted as polynomial functions of SOC [17].

$$V_{oc}(SOC) = a_0 + a_1.SOC + a_2.SOC^2 + a_3.SOC^3 + a_4.SOC^4 + a_5.SOC^5$$
$$R_{Series}(SOC) = a_0 + a_1.SOC + a_2.SOC^2 + a_3.SOC^3 \quad (2.11)$$

Addition of exponential terms helps modeling parameters at low and high SOC [13]. Plot of equivalent circuit parameters versus SOC can be observed in Figure 2.6.

$$V_{oc}(SOC) = a_0 + a_1.SOC + a_2.SOC^2 + a_3.SOC^3 + E_0.\exp(e_0.SOC)$$
$$R_{Series}(SOC) = a_0 + E_0.\exp(e_0.SOC) \quad (2.12)$$

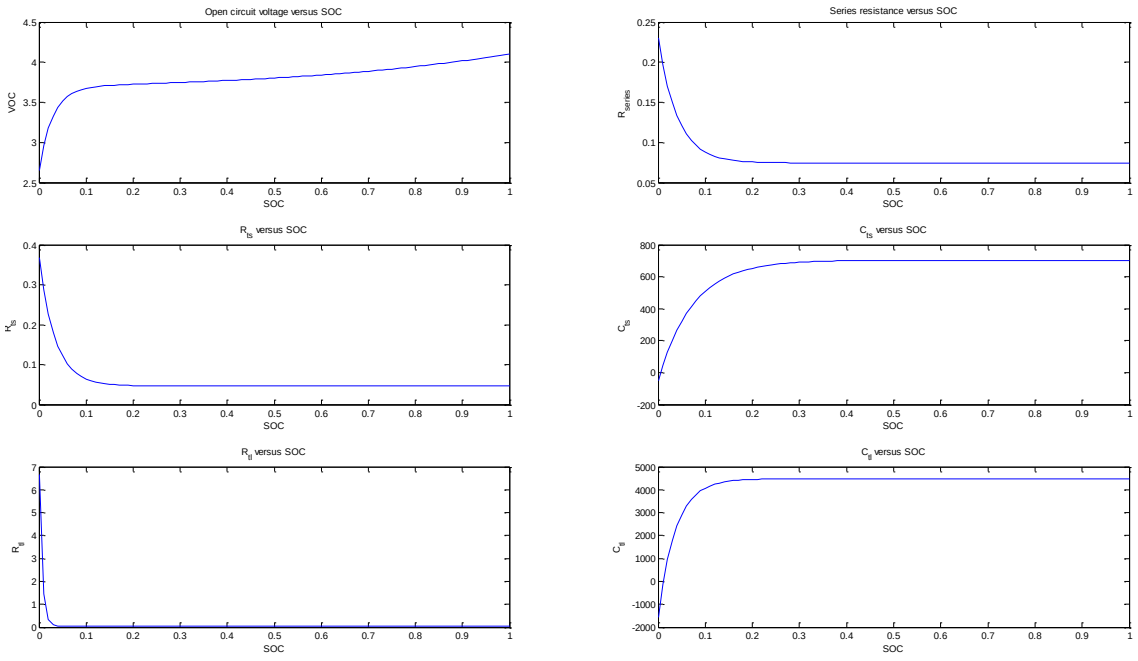

Figure 2.6. Plots of equivalent circuit parameters and open circuit voltage against SOC. Extracted from [13].

Implemented Simulink model is shown in Figure 2.7. Further details of the Simulink model can be found in the Appendix A. Results of the battery simulation are shown in Figure 2.8.

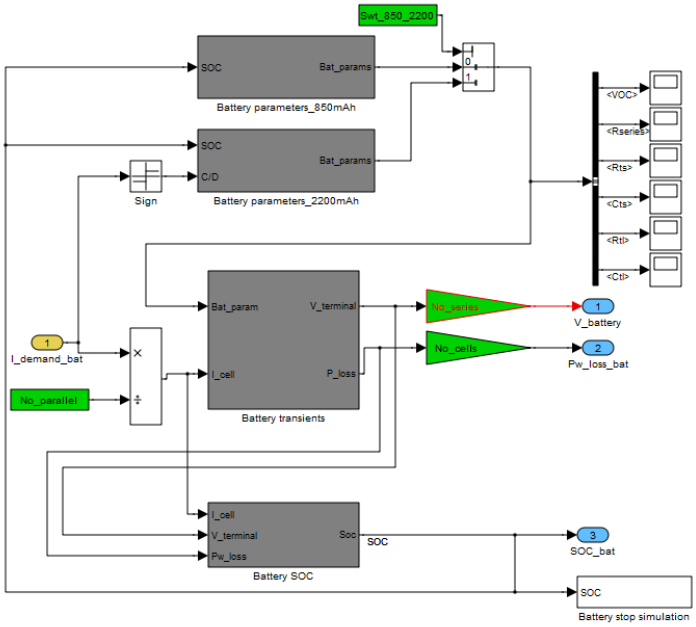

Figure 2.7. Overview of Simulink model of the battery.

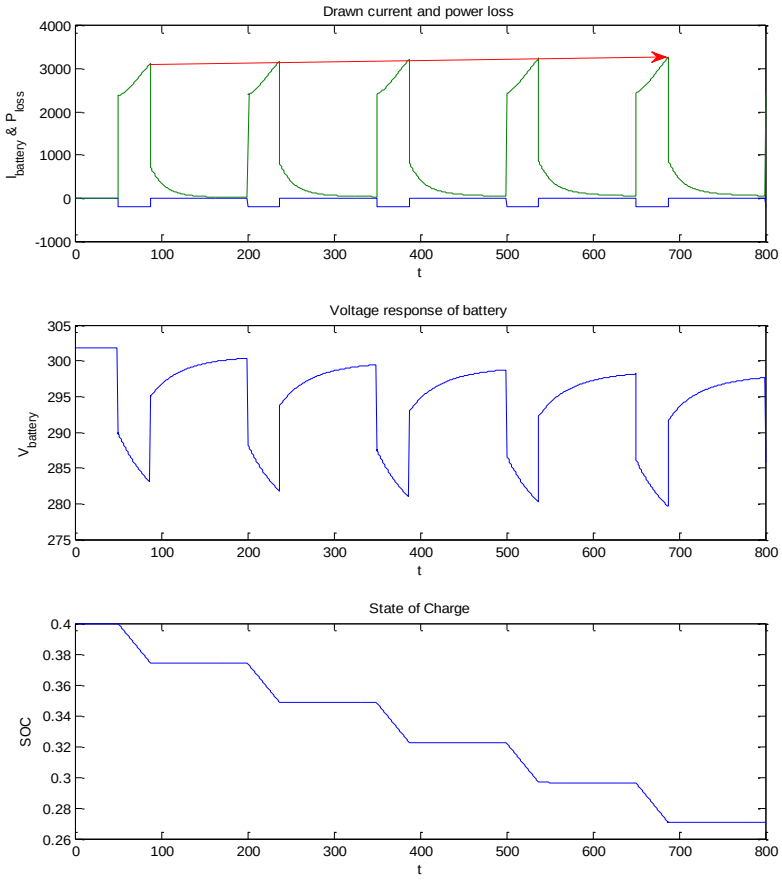

Figure 2.8. Simulation results for 200A discharge, increasing trend in power loss can be observed by red arrow as SOC of the battery decreases.

2.1.4 Modeling State of Health and Degradation of the Battery

Models for estimating other features of the battery such as temperature, SOC, cycle history, age, etc. are available in literature. Modeling state of health (SOH) of the battery requires laborious tests and yet most of them are far from being accurate in modeling decay of battery capacity and power over time.

Depth of discharge (DoD) shows what percentage of nominal battery capacity has been used between one charging period to another. If a battery is discharged until 10% and charged back to 90%, DoD is 80%. DoD has significant effect on battery life, such that most of the batteries can endure for twice the cycle life, if depth of discharge is kept low. Equation 2.13 gives number of cycles a battery can endure in an application with given average depth of discharge [9].

$$\mathrm{LIFE} = \mathrm{LIFE}_{\mathrm{zero}} \mathrm{e}^{\mathrm{m}*\mathrm{DoD}} \tag{2.13}$$

Where LIFE is the number of cycles in life at given DoD. $\mathrm{LIFE}_{\mathrm{zero}}$ is the number of cycles in life at zero DoD, obtained by extrapolating cycle-life data. m is the slope of natural logarithm of LIFE/ $\mathrm{LIFE}_{\mathrm{zero}}$ versus DoD.

Another method for modeling degeneration of the battery is given in [18]. This method punishes variation of SOC from SOC mean. SOC mean is calculated using mean value filter [10].

$$\mathrm{Degeneration(t)} = \mathrm{k}.\int_0^{\mathrm{t}} (\mathrm{SOC(t)} - \mathrm{SOC}_{\mathrm{mean}}(\mathrm{t}))^2 \mathrm{dt} \tag{2.14}$$

Value of k, in Equation 2.14, depends on battery type and can be found as 3/250000 for Li-ion [18]. Li-ion can withstand 1500 cycles at 80% DoD. However it may increase up to 200000 cycles for 5% DoD, which makes Li-ion suitable for RE-EV applications. Battery SOC is expected to vary from the lower limit by 5% to 10% during extended range operation. For extended range of 500 km, more than 50 cycles are expected at 10% DoD.

2.2 Electric Motor

Electric machines are used for converting electrical energy to mechanical energy or vice versa. In a SHEV, there are two electric machines. One of them is used as traction motor, which is the only source of traction in a SHEV and directly connected to wheels. In most of the applications, transmission is avoided due to wide speed range of electric motors. Traction motor is connected to wheels with a single ratio, as most authors call it, the final drive ratio. Traction motor in a SHEV is also responsible for recuperative braking. Other electric machine is used as generator, which is mechanically coupled to the ICE. Although this electric machine operates as generator, it also handles the task of starting and igniting the ICE.

Basically, there are two types of electric motors (EM) which are classified according to their driving current. DC motor is driven by direct current whereas an AC motor is driven by alternating current. Figure 2.9 illustrates various types of AC motors, which can be classified into two main groups, asynchronous and synchronous. In a synchronous machine, rotor speed is synchronized with the frequency of AC supply current whereas an asynchronous machine needs 'slip' in order to produce torque, therefore rotor speed is not synchronized to AC supply current.

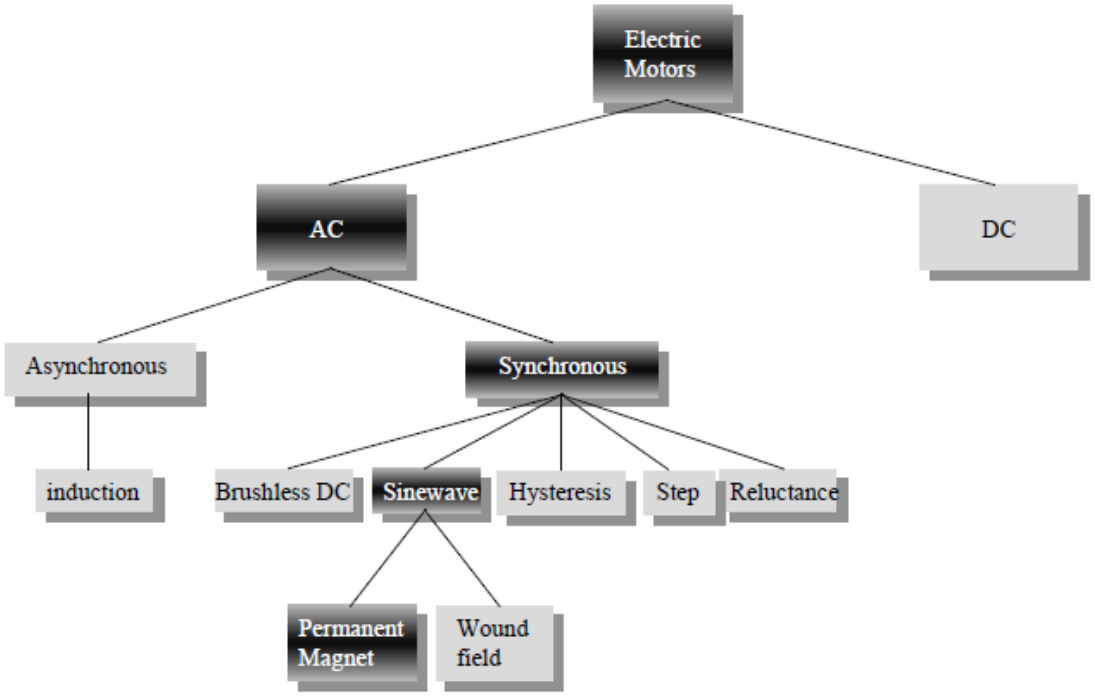

Figure 2.9. Types of electric machines [20].

Use of DC motors, are not common in electric vehicles as traction motors due to high maintenance cost (brushes), medium life span and low power density (kW/kg). AC motors are preferred due to their high power density and maintenance free operation.

Three types of AC motors are commonly used as traction motors in SHEV applications, which are:

- AC Induction Machine (IM)
- Switched Reluctance Machine (SRM)
- Permanent Magnet Synchronous Machine (PMSM)

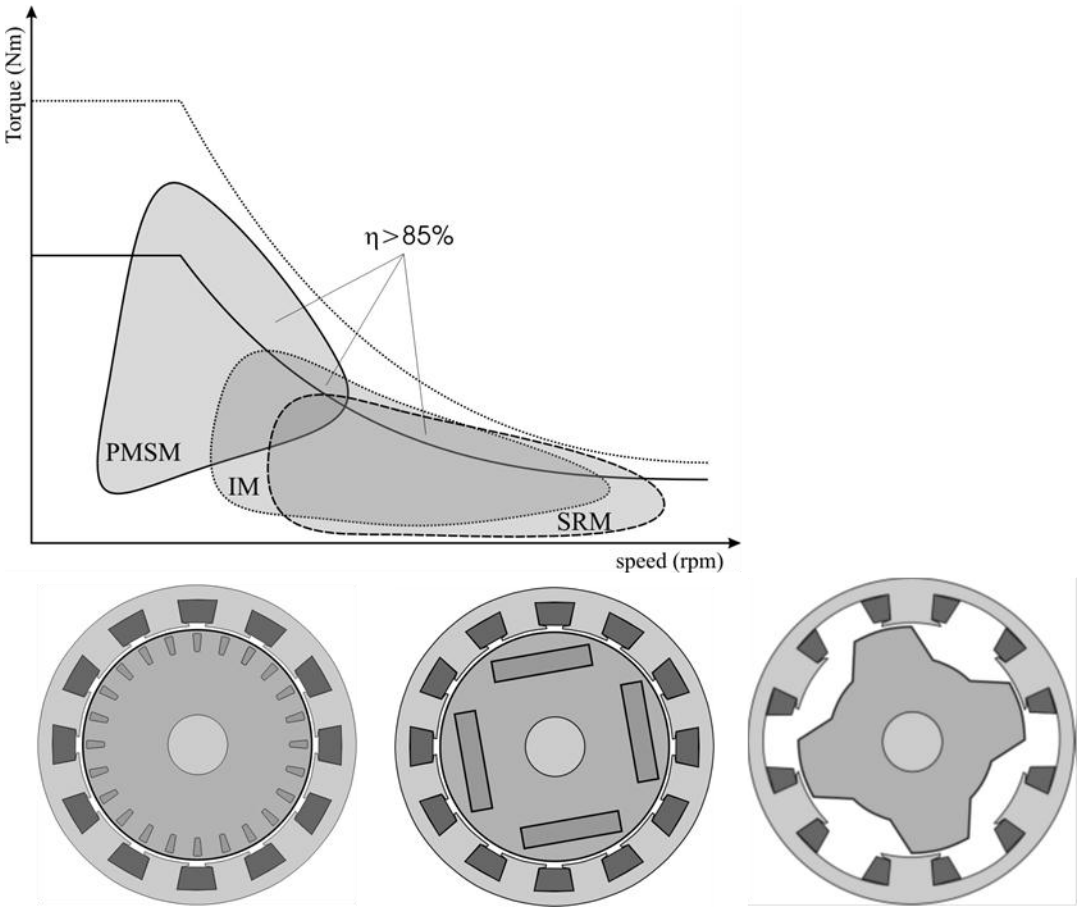

Figure 2.10. High efficiency operating regions for SRM, IM and PMSM. From left to right: IM, PMSM, SRM.

Induction Machine (IM): Power is supplied to the rotor through electromagnetic induction. A rotating stator field is created by alternating current. Rotor of the IM rotates at

a slower speed than the stator field, which results in varying magnetic flux through the rotor. Since windings of IM rotor contains closed loops of wire, varying magnetic flux induces voltage which in return generates current flow through rotor windings. As stated by Lenz's law, rotor current creates a magnetic field which opposes the change in magnetic flux that induced voltage in the first place. Hence torque is produced because rotor magneto motive force (mmf) is trying to follow and align with stator mmf.

Induction motors are preferred in EV and HEV application because of their simple and rugged design, robust operation and low cost. IMs are not common in EV & HEV passenger cars due to their low power density and low efficiency compared to PMSM. Their applications are mostly hybrid truck and buses, where space is no longer a constraint. High efficiency operating region of an IM along with its cross section can be observed in Figure 2.10.

Switched Reluctance Machine (SRM): Stator of a reluctance motor consists of electromagnetic poles formed by windings. These poles act like a magnet when coils are energized. The rotor of the SRM is constructed from soft magnetic material and just like its stator there are salient poles on the rotor. SRM operates with same principle as solenoids, when stator poles are energized, rotor poles are attracted to the nearest active stator pole, moving to a point with less reluctance. In Figure 2.10, SRM with 6 stator poles and 4 rotor poles can be observed. Stator poles are always more than rotor poles, in order to sustain torque at all times by preventing alignment of rotor and stator teeth. In order to sustain rotation and torque, stator poles shall rotate in advance of the rotor poles. Hence coils of the stator shall be activated synchronously, in a fashion to produce maximum torque per ampere [10,11].

SRMs are not very common in EV and HEV industry due to significant torque and electrical ripple. In order to avoid damage to electrical equipment a large HV capacitor is necessary. Another important drawback is the acoustic noise. Control of SRM, with low torque ripple, is quite complex but still it is easier compared to IM and PMSM [2]. SRMs may be preferred in the future for EV applications since they are durable, cheap, low cost and highly efficient.

Permanent Magnet Synchronous Machine (PMSM): Electric Machines that use permanent magnets to create air-gap magnetic flux are called Permanent magnet machines. The field mmf is created by permanent magnets located either on the rotor or buried inside the rotor. These machines are called synchronous, since these are capable of producing torque when rotor speed is synchronized to the speed of stator field.

Permanent magnets are positioned and shaped in a fashion to create a sinusoidal rotor flux linkage. Depending on the position and shape of the permanent magnets at the rotor, PMSMs can be classified into 4 main groups [25] which are:

- Surface mounted PM synchronous machine (SPM)
- Surface inset PM synchronous machine (SIPM)
- Interior PM synchronous machine (IPM)
- Interior PM with circumferential orientation synchronous machine

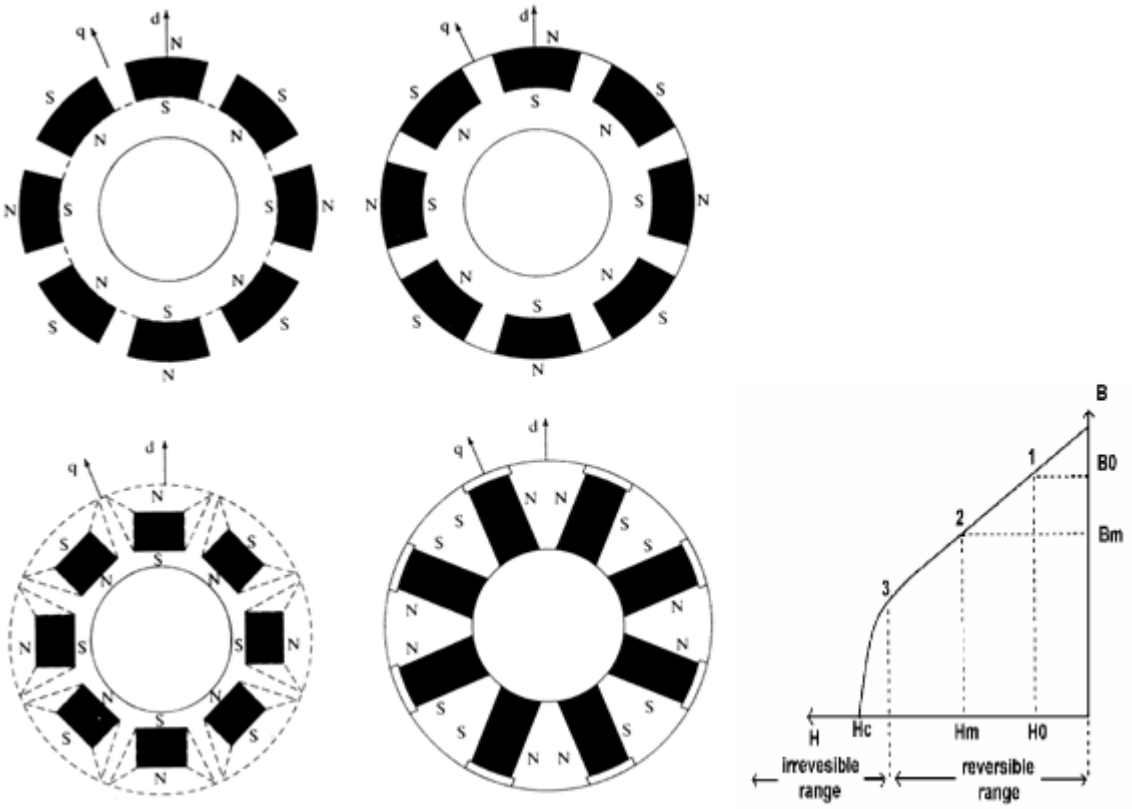

Figure 2.11. Types of permanent magnet synchronous machines and a typical B-H curve [25,26].

All of the PMSM types can yield high efficiency rates since no current is flowing through the rotor hence copper losses are reduced significantly. Also cooling needs due to high rotor currents is not an issue. The only significant drawback of PMSM is that permanent magnets can lose their features when they are exposed to high temperature or high load. Large magnetic fields, opposing the rotor magnetic field may cause irreversible demagnetization. The limits of operation depend on the magnet type. Common types are SmCo, NdFeB, Ferrite and Alnico. Linear region of the B-H curves of these materials indicate reversible operating region for these materials, see Figure 2.11.

Efficiency of SPMs are significantly low compared to IPMs, especially in higher speeds. Since copper loss and core losses are higher in SPMs at higher speeds. Another drawback of SPMs is that they exhibit low field weakening capacity, which in return decreases the maximum available speed of the motor. Both SPM and SIPM machines are not preferred in HEV applications due to narrow constant power region, compared to IPMs. Since use of gearbox is not desired, especially in EV applications, wider constant power range is desired. Due to their good torque & power density and high efficiency, IPMs became the most popular choice for traction motors in today's light vehicles and passenger cars.

2.2.1 Dynamic Motor Model – IPM

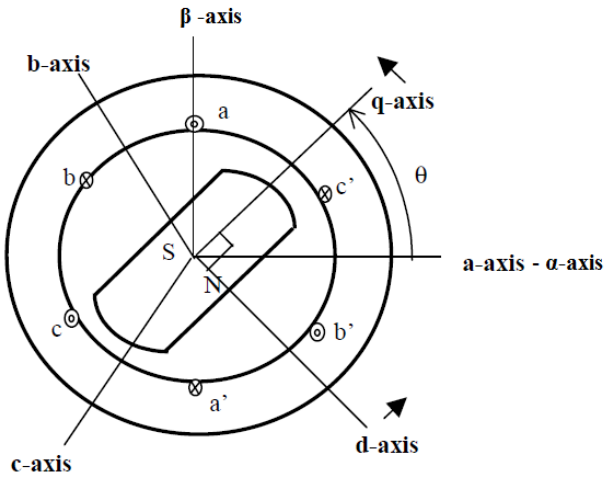

Figure 2.12. Stationary and synchronous frames for a PMSM [26].

A 3-phase PMSM shown in Figure 2.12, can be analyzed in one of the 3 reference frames, which are:

- abc axes frame: Stationary reference frame with respect to stator, abc are aligned with 3-phases of the motor.
- α-β axes frame: Stationary reference frame with respect to stator, where α-axis is in the same direction with a-axis and β -axis lags α-axis by 90°.
- d-q axes frame: Synchronous reference frame, fixed to rotor frame. Where d-axis is in the same direction with air-gap flux vector and q-axis lags d-axis by 90°.

Transformations between these reference frames are straight forward and together they serve as the basis of a very good and popular motor control technique, Field Oriented Control (FOC). Transformation from abc axes to α-β axes is called Clarke Transformation, which is used for transforming a 3-phase system into a 2-phase system. Equations of Clarke transformation is given in Equation 2.15 and it can be observed in Figure 2.13.

$$\begin{bmatrix}\alpha\\ \beta\end{bmatrix} = \begin{bmatrix} 2/3 & -1/3 & -1/3 \\ 0 & 1/\sqrt{3} & -1/\sqrt{3} \end{bmatrix} \begin{bmatrix} a \\ b \\ c \end{bmatrix} \tag{2.15}$$

Transformation from stationary α-β axes to d-q axes is achieved by Park transformation. d-q frame is called synchronous frame because d-axis is aligned with air-gap flux of the rotor, which means d-q frame is fixed to the rotor. Since stator field is synchronous to the rotor, an AC current vector at stator is simply transformed into a DC current vector at the fixed d-q frame. Equation 2.16 represents the Park transformation, where ϑ_{field} is the rotor angle.

$$\begin{bmatrix} d \\ q \end{bmatrix} = \begin{bmatrix} \cos(\vartheta_{field}) & \sin(\vartheta_{field}) \\ -\sin(\vartheta_{field}) & \cos(\vartheta_{field}) \end{bmatrix} \begin{bmatrix}\alpha\\ \beta\end{bmatrix} \tag{2.16}$$

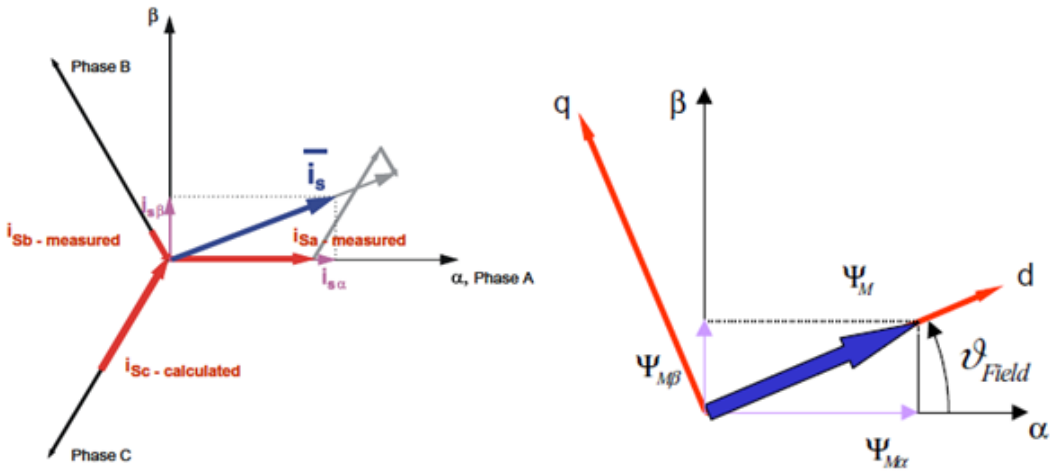

Figure 2.13. Clarke and Park transformations, Clarke is on the left and Park is on the right [27].

PMSM can be modeled in d-q frame with equivalent circuits given in Figure 2.14. Flux linkage vectors are shown in Figure 2.15. Basically resistances are used for modeling resistive (copper) losses at the stator. Inductances are used for modeling flux linkage formed by stator currents. And controlled voltage sources represent the back-emf which is product of flux linkage and electrical speed. Transforming back into abc frame, one can observe back emf of a PMSM is sinusoidal. Core losses, leakage inductances and mutual inductances are ignored in this model.

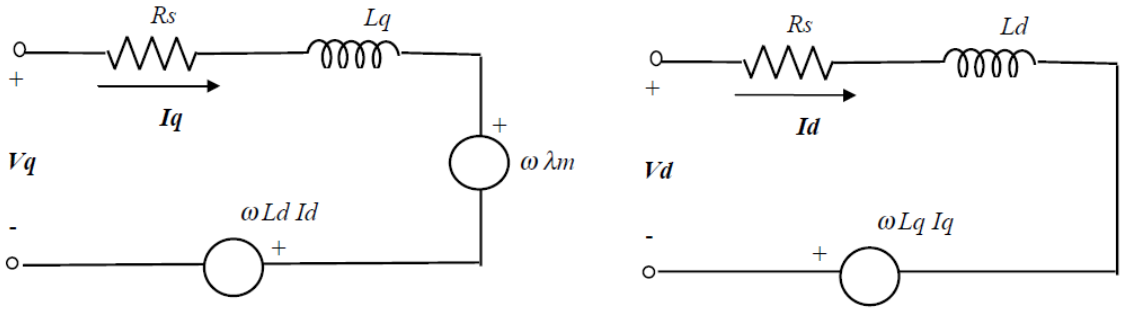

Figure 2.14. Equivalent circuit of PM Synchronous motor, left circuit represents q-axis and right circuit represents d-axis [26].

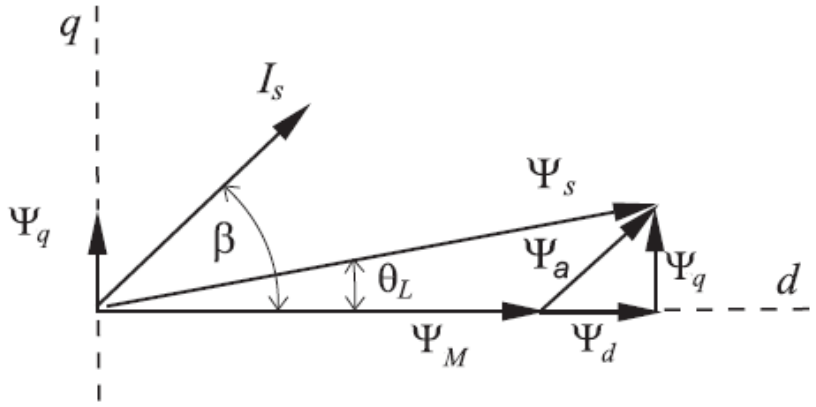

Figure 2.15. Flux linkage vectors of IPM, overall flux linkage is vector addition of flux linkage by permanent magnets and flux linkage by stator currents.

where ψ_M is the flux linkage of the permanent magnets. ψ_d is the flux linkage due to d-axis current ($\psi_d = L_d\, i_d$). ψ_q is the flux linkage due to q-axis current ($\psi_q = L_q\, i_q$). Ψ_s is the overall flux linkage. β is the angle of stator current to direct axis current. θ_L is the angle of flux linkage vector. I_d , I_q are stator currents in dq frame. L_d, L_q are magnetizing inductance components for d and q axis respectively, Stator flux linkage is normally LI_s, where L is a 2x2 matrix. But mutual inductances are ignored, only diagonal inductances L_d, L_q are considered. ω is the electrical speed , $\omega = p\,\omega_m$ is the mechanical speed (rotor speed). R_s is the stator resistance. p is the number of pole pairs and V_d, V_q are the stator voltage components of d-q axis, which can be calculated through Equation 2.17 and 2.18.

$$V_d = R_s i_d + L_d \frac{di_d}{dt} - \omega L_q i_q \tag{2.17}$$

$$V_q = R_s i_q + L_q \frac{di_q}{dt} + \omega L_d i_d + \omega \psi_M \tag{2.18}$$

V_d, V_q are control inputs of the PMSM, they are transformed into V_a, V_b and V_c, which are then applied to the terminals of the electric motor by the inverter. The controlled states of the PMSM are stator currents of the electric machine that generate torque. The state equations of d-q axis currents are given in Equation 2.19 below:

$$\begin{bmatrix} \dot{i}_d \\ \dot{i}_q \end{bmatrix} = \begin{bmatrix} -R_s/L_d & \omega L_q/L_d \\ -\omega L_d/L_q & -R_s/L_q \end{bmatrix} \begin{bmatrix} i_d \\ i_q \end{bmatrix} + \begin{bmatrix} 1/L_d & 0 \\ 0 & 1/L_q \end{bmatrix} \begin{bmatrix} V_d \\ V_q \end{bmatrix} + \begin{bmatrix} 0 \\ -\omega\psi_M/L_q \end{bmatrix} \quad (2.19)$$

Torque of an IPM can be represented as cross product of 2 space vectors ψ_S and I_s, current and flux linkage vector.

$$T = \frac{3}{2} p \left(\psi_d i_q - \psi_q i_d\right) = \frac{3}{2} p \left(\psi_M i_q + (L_d - L_q) i_d i_q\right) \quad (2.20)$$

For a surface mounted PMSM, direct and quadrature axis inductances, L_d and L_q are approximately equal due to equal path permeability around the rotor circumference ($L_q > L_d$). However for an IPM quadrature axis inductance is always greater than direct axis inductance. As can be observed from Equation 2.20, second term vanishes in SPMs where as it can be used for generating torque in IPMs. Torque is related directly to quadrature axis current in SPM machines, so controlling torque is much easier. Whereas for IPMs, torque depends on both axis currents, hence control becomes more complex.

Output power of the IPM can be considered as torque multiplied by speed. However input power includes copper losses and magnetic power in windings. Equations of input power of IPM are given in 2.20, 2.21 and 2.22, considering a 3-phase machine [28,23]. Since Park and Clarke transformations are carried out in a fashion to preserve power per phase, the power equation in d-q axis can be simply given as follows:

$$P_{in} = V_a I_a + V_b I_b + V_c I_c$$
$$P_{in} = \frac{3}{2}\{V_d I_d + V_q I_q\} \quad (2.21)$$

Components of input power can be observed in Equation 2.22. First part represents copper losses, second part represents magnetic power stored in windings and third part represents the mechanical power or output power of the EM. Overall efficiency is given in Equation 2.23.

$$P_{in} = \frac{3}{2} R_s \left({i_d}^2 + {i_q}^2 \right) + \frac{3}{2} \left(i_d \frac{d\psi_d}{dt} + i_d \frac{d\psi_M}{dt} + i_q \frac{d\psi_q}{dt} \right) + \frac{3}{2} p\omega_m \left(\psi_d i_q - \psi_q i_d \right) \tag{2.22}$$

The logic of ignoring iron losses can be better explained here. Even though core losses depend on overall flux linkage, they depend mostly on angular frequency. And since we don't have control over the angular frequency, we don't have control over hysteresis losses that are proportional to ω or eddy current losses which are proportional to ω^2. The power loss function including core losses is given in Equation 2.24 [29].

As can be observed from Equation 2.22, efficiency of IPM depends on copper losses, which in return depend on square of stator current, I_s given by Equation 2.25. Power of windings do not affect the efficiency since inductances do not consume power, they act as very small reservoirs and can be ignored in efficiency analysis. So in order to minimize power loss of an IPM or any kind of PMSM, one shall minimize armature current for the demanded torque. Maximum torque per ampere control (MTPA) has proven to be the most promising technique for minimizing power loss, until base speed is reached. After base speed is exceeded, field weakening becomes necessary due to increasing terminal voltage

$$\eta_{motor} = \frac{P_{in} - P_{loss}}{P_{in}} = \frac{T\omega}{\frac{3}{2}\left(V_d I_d + V_q I_q \right)} \tag{2.23}$$

$$P_{loss} = {}^{3}/_{2}\, R_s \left({i_d}^2 + {i_q}^2 \right) + a(\omega) \left[\left(L_q i_q + \psi_M \right)^2 + \left(L_q i_q \right)^2 \right] \tag{2.24}$$

$$P_{loss} \cong {}^{3}/_{2}\, R_s \left({i_d}^2 + {i_q}^2 \right) = {}^{3}/_{2}\, R_s {i_s}^2 \tag{2.25}$$

Block diagram of the PMSM can be seen in Figure 2.16. Matlab implementation of the PMSM can be observed in Figure 2.17. The parameters of IPM, for 50kW traction motor can be found in Appendix A along with detailed overview of the Simulink model.

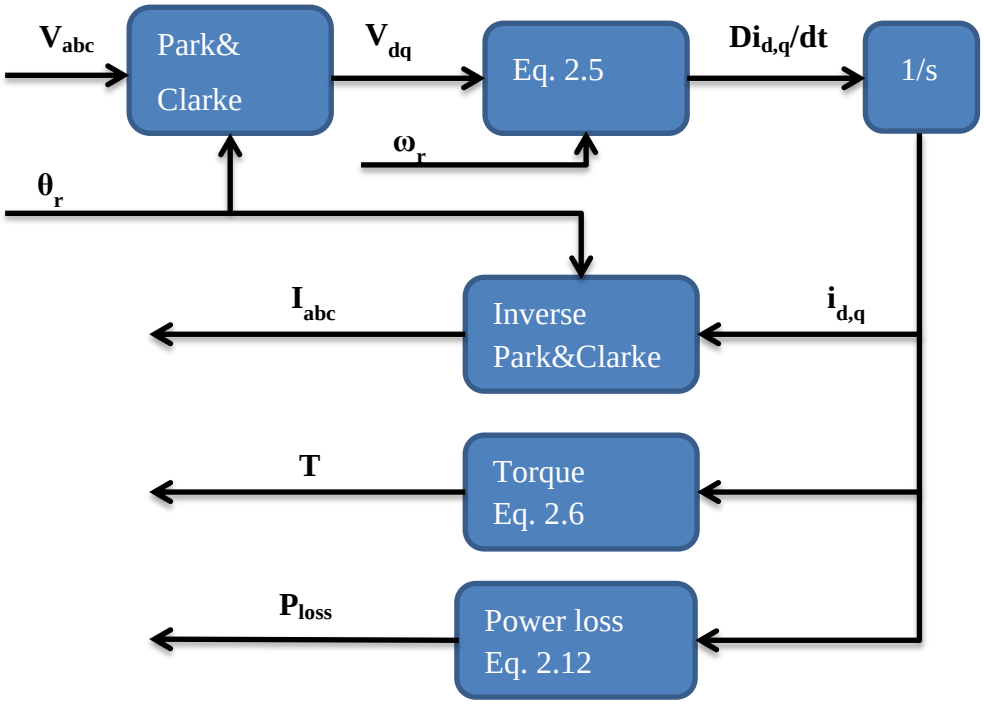

Figure 2.16. Block diagram of PMSM.

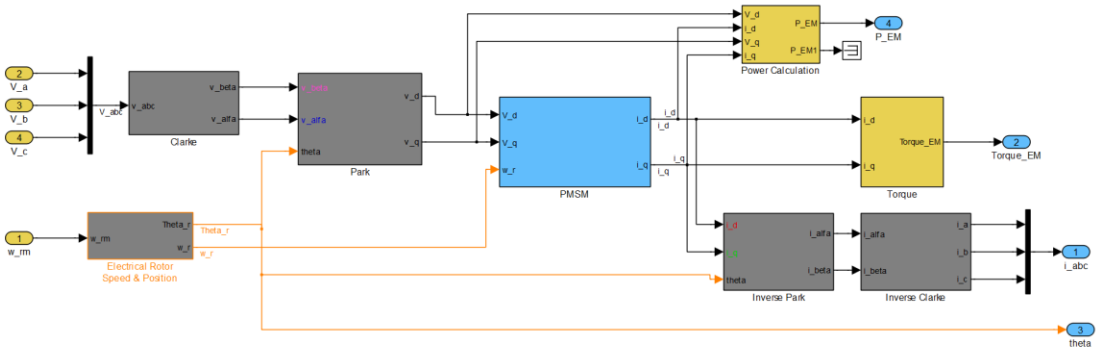

Figure 2.17. Simulink model of PMSM.

2.2.2 Control & Optimum Operation of IPM

Voltage and current limitations are imposed on IPMs due to motor and inverter size, insulation material, power loss limit, temperature limit… etc. The optimum operation problem can be defined as minimizing power loss by determining d-q axis current references for a given torque, speed, maximum voltage and current limits. Operation of an IPM can be analyzed in three different regions, which are:

- Constant torque range
- Partial field weakening range
- Field weakening range

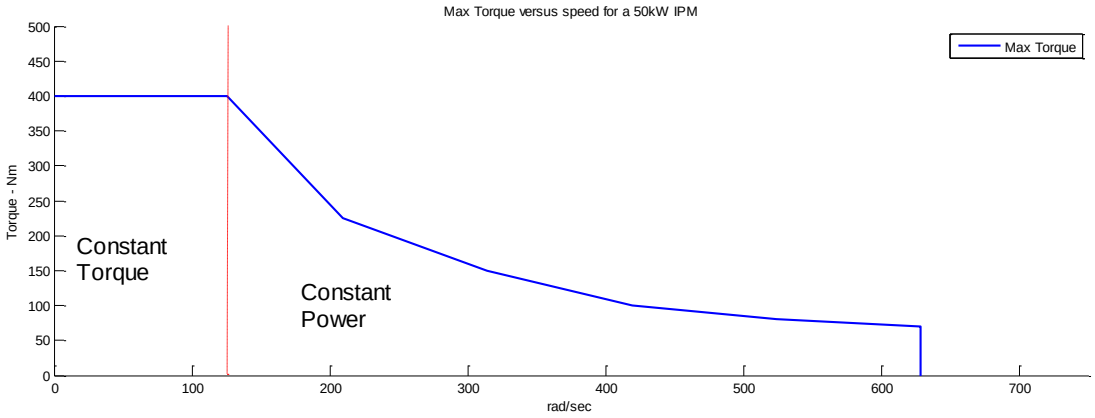

Figure 2.18. Maximum Torque versus speed curve of 50kW – 400Nm IPM.

$$\sqrt{{i_d}^2 + {i_q}^2} \leq I_{max} \tag{2.26}$$

$$\sqrt{{V_d}^2 + {V_q}^2} \leq V_{max} \tag{2.27}$$

$$\sqrt{(\psi_M + L_d i_d)^2 + (L_q i_q)^2} \leq {V_{max}}/{\omega} = \psi_{max}(\omega) \tag{2.28}$$

In constant torque range until ω_1, red dashed line in Figure 2.18, is reached only current limits given be Equation 2.26 are taken into account since terminal voltage or flux linkage are not the limiting factors. Back emf, which is proportional to speed, does not build up to voltage limits of the inverter in this region. Maximum torque curve, T_1, is tangent to maximum current circle at points C_1 and F_1. So as long as speed is below ω_1, F_1-G_1-A_1-B_1-C_1 curve given in Figure 2.19 represents maximum torque per current or MTPA. This curve can be used for calculating optimum quadrature and direct axis currents [30].

Partial field weakening range is defined for speeds greater than ω_1. Maximum flux curve, ψ_{max} (ω, V_{max}), for given speed and DC bus voltage, is defined by Equation 2.28. In

this region maximum torque can be generated at intersection of maximum current circle and maximum flux ellipse. Obviously, optimum current path depends on rotor speed in this region. For example, optimum path when $\omega = \omega_2$ is given by the curve E_1-G_1-A_1-B_1-D_1. As can be observed from Figure 2.19, for torques smaller than T_3, MTPA control can still be used (G_1-A_1-B_1). Because constant torque curves which are smaller than T_3 cross the MTPA curve inside the maximum flux ellipse for given speed. This is the reason for calling this region as partial field weakening; higher demagnetizing current (d-axis current) may or may not be necessary depending on torque reference [30].

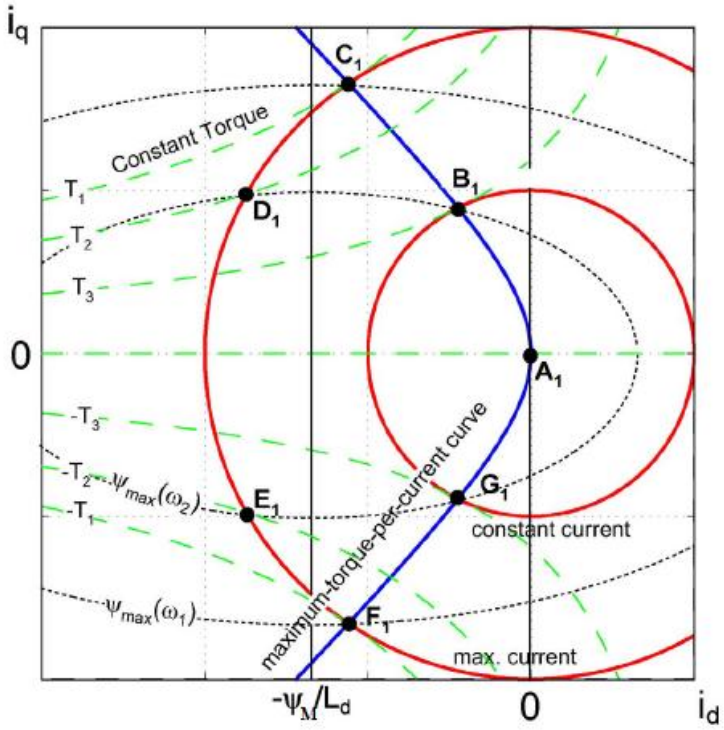

Figure 2.19. Current limit circle (red), flux limit ellipse (dotted black), constant torque curves (striped green) [30].

Field weakening range is entered when speed exceeds a limit, such that maximum torque at that speed is not generated at the intersection of maximum flux ellipse and maximum current circle. See Figure 2.20, field weakening range is entered when speed is greater than ω_4. For flux ellipses corresponding to greater speeds than ω_4, maximum torque can be generated by using maximum torque per flux curve (MTPF). Observe Figure 2.20 for an example, maximum achievable torque at speed of ω_5 is B_2 or C_2, but optimal current curve is C_2-A_2-B_2 for torque range of 0 to T_5. For any speed over ω_4, current optimal

operating point for a given torque reference, can be defined as the intersection of maximum flux ellipse and given torque curve.

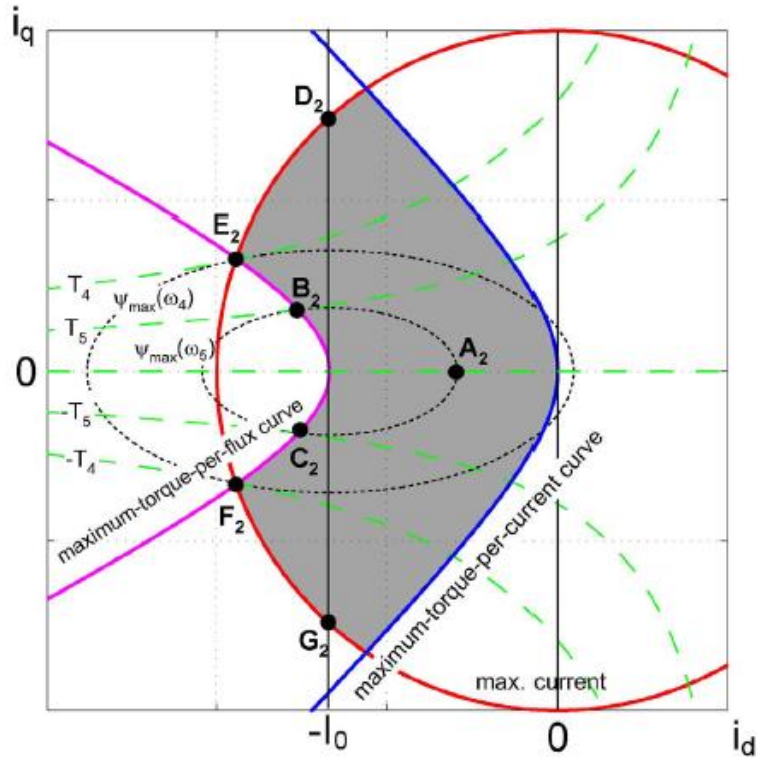

Figure 2.20. Field weakening region, current optimal operating path for speed ω_5 is C_2-A_2-B_2 [30].

2.2.2.1 Implementation of Maximum Torque per Ampere Control (MTPA). The optimization problem is defined as finding the maximum torque for a given stator current magnitude (I_S). Keeping stator current magnitude constant, the angle (β) is altered in order to find maximum possible torque for that current magnitude. See Figure 2.15, direct and quadrature axis currents can be expressed in terms of stator current magnitude and angle.

$$I_S \sin\beta = I_q \ , \quad I_S \cos\beta = I_d \tag{2.29}$$

Expressing torque in terms of stator current, magnitude and angle, see Equation 2.30 [25]. Differentiating torque with respect to β and equating to zero, optimal condition for angle can be found as in Equation 2.31 [25].

$$T = \frac{3}{2} p \left(\psi_M i_S \sin\beta + \frac{1}{2}(L_d - L_q) {i_S}^2 \sin 2\beta \right) \tag{2.30}$$

$$\frac{dT}{d\beta} = 0 \rightarrow \beta_{opt} = \cos^{-1}\left\{ \frac{-1}{4(L_d - L_q) I_S} - \sqrt{\left(\frac{1}{4(L_d - L_q) I_S} \right)^2 + \frac{1}{2}} \right\} \tag{2.31}$$

Then i_d-i_q curve for MTPA can be derived as follows:

$$I_{d\_mtpa} = \frac{\psi_M - \sqrt{{\psi_M}^2 + 4(L_d - L_q)^2 {I_{q\_mtpa}}^2}}{2(L_d - L_q)} \tag{2.32}$$

For a given torque reference, quadrature axis current cannot be calculated directly. Equation 2.33, showing relationship between q-axis current and torque can be found by substituting Equation 2.32 into Equation 2.19.

$$T = \frac{3}{2} p \, I_{q\_mtpa} \left\{ \frac{\psi_M + \sqrt{{\psi_M}^2 + 4\left(L_d - L_q\right)^2 {I_{q\_mtpa}}^2}}{2} \right\} \tag{2.33}$$

Optimal quadrature axis current equation is extracted from Equation 2.33, after suitable manipulations as:

$$f\left(I_{q\_mtpa}\right) = {I_{q\_mtpa}}^4 \left(L_d - L_q\right)^2 + \frac{T \, I_{q\_mtpa} \, \psi_M}{3/2 \, p} - \left(\frac{T}{3/2 \, p} \right)^2 = 0 \tag{2.34}$$

However analytical solution of Equation 2.34 is complex and computationally expensive, therefore I_{q_mtpa} is calculated offline for feasible torque range of IPM using a numerical method such as Newton's, as proposed by [31]. Details of iteration can be found in [31], I_{q_mtpa} is plotted against feasible torque range in Figure 2.21. Direct axis current for

MTPA, I_{d_mtpa}, can be calculated by substituting I_{q_mtpa} into Equation 2.32, which is also plotted in Figure 2.21.

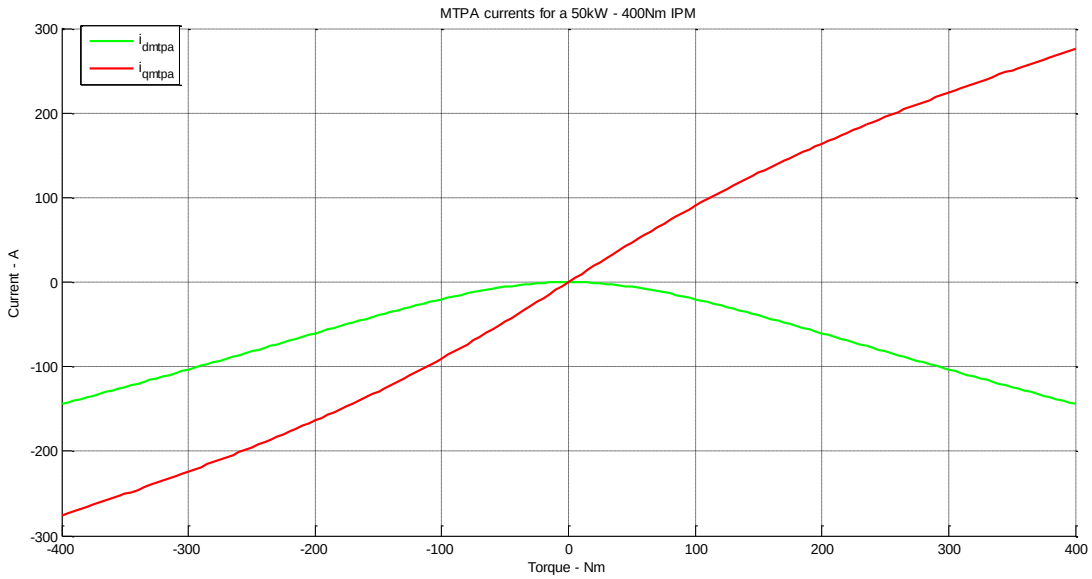

Figure 2.21. Offline calculated d-q axis currents for MTPA control (Feasible torque range of IPM, -400 to 400).

2.2.2.2 Implementation of Optimal Field Weakening Range Control. As mentioned, back-emf of an IPM is proportional to speed, where co-efficient is the flux-linkage. Hence after a certain speed, flux linkage should be decreased in order to prevent back-emf from building up to a level where pushing current to the motor is no longer possible. Hence after a certain speed, overall flux linkage is decreased by creating a flux vector opposing the permanent magnet's flux vector. Observe Figure 2.19 and Figure 2.20, maximum value of flux vector shrinks as speed increases. Overall flux vector of an IPM is given by Equation 2.35 and flux vector during field weakening is shown in Figure 2.22.

$$\overrightarrow{\psi_S} = \overrightarrow{\psi_M} + \overrightarrow{\psi_d} + \overrightarrow{\psi_q} \tag{2.35}$$

Maximum flux limit given by Equation 2.28 and maximum voltage limit given by Equation 2.27 are active during whole flux weakening range. The current limit is however may or may not be active, depending on field weakening region, partial or full. During partial field weakening, current limit given by Equation 2.26 is also active as can be

observed from Figure 2.22. The maximum torque in this region is generated at intersection of flux limit ellipse and current limit circle. If speed increases further, full field weakening region is entered, where current limit is no longer an active limitation. Maximum torque in this region is defined by MTPF curve, see Figure 2.20.

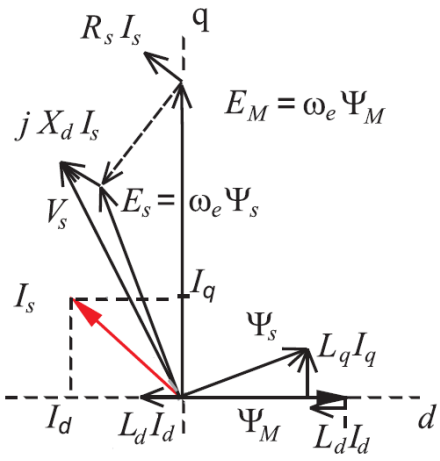

Figure 2.22. Phasor diagram of IPM in field weakening region. Also valid for MTPA, demagnetization due to d-axis current is more significant in field weakening region.

In partial field weakening region direct axis current, i_d, becomes smaller than MTPA current, hence overall flux linkage vector is reduced by direct axis current. In partial field weakening region, MTPA current references can be used for torque values that fall inside flux limit ellipse, see Figure 2.19, A_1-G_1 or A_1-B_1. For higher torque at that speed, d-q axis currents are calculated for the path shown in Figure 2.19, G_1-E_1or B_1-D_1. Optimal d-q axis currents in partial field weakening region can be calculated for a certain speed and DC-bus voltage using Equations 2.36 to 2.39, proposed by [30,31]. In partial field weakening, quadrature and direct axis current references are set as I_{q_corr} and I_{d_fw} respectively.

$$I_{d\_fw} = -\frac{\psi_M}{L_d} + \frac{1}{L_d}\sqrt{\frac{V_{max}{}^2}{3\omega^2} - L_q{}^2 I_{q\_mtpa}^2} \tag{2.36}$$

$$\Delta I_d = I_{d\_fw} - I_{d\_mtpa} \tag{2.37}$$

$$\Delta I_q = \frac{(L_q - L_d)\,\Delta I_d\, I_{q\_mtpa}}{\psi_M + (L_d - L_q) I_{d\_fw}} \tag{2.38}$$

$$I_{q\_corr} = \Delta I_q + I_{q\_mtpa} \tag{2.39}$$

In full field weakening range, current limit is no longer active and optimal d-q axis currents are set as I_{q_fw} and I_{d_fw}. Optimal I_{q_fw} can be calculated through Equation 2.40.

$$I_{q\_fw} = \frac{1}{L_q}\sqrt{\frac{{V_{max}}^2}{3\omega^2} - \left(L_d i_{d\_fw} + \psi_M\right)^2} \tag{2.40}$$

Transition between MTPA, partial and full field weakening regions are presented by the flowchart in Figure 2.23, which is proposed by [31]. Simpler transition rules depending only on speed can be extracted but without considering torque reference, however optimality for all operating points cannot be achieved with this simpler approach. Proposed methodology by [31] suggests comparing current references I_{d_mtpa}, I_{q_mtpa}, I_{q_corr}, I_{q_fw} and I_{d_fw} in order to obtain the optimal operation for given speed and torque reference.

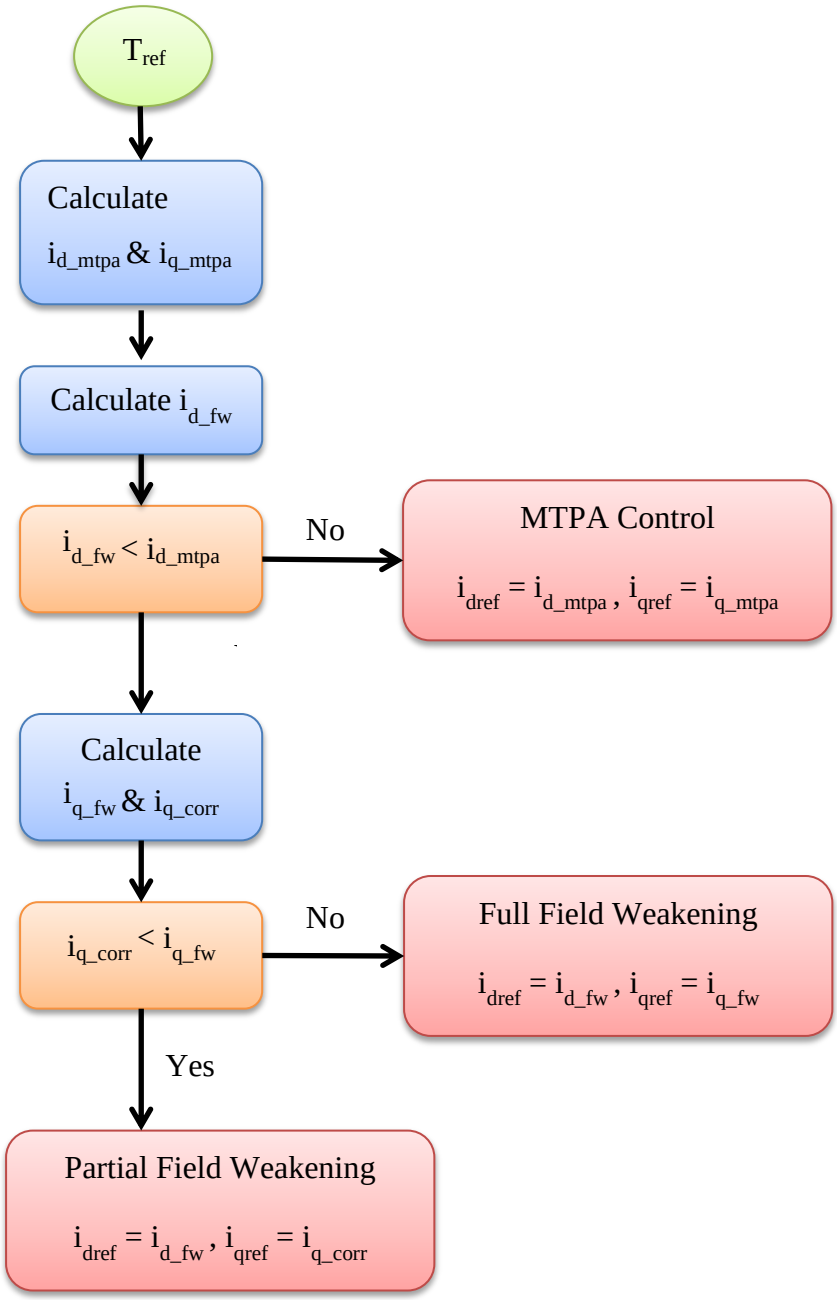

Figure 2.23. Flowchart for reference current for whole torque range of IPM, [15] Current reference controller.

Current reference controller proposed by [31] is implemented in Simulink along with the PMSM model. However, this controller only generates reference currents. PI controllers are also implemented as shown in Figure 2.24 [32]. As proposed in [32], decoupling terms are introduced in order to control i_d and i_q separately. Transient response is significantly improved and PI coefficients are easily tuned when two loops are decoupled. Outputs of PI controller are the reference voltages V_d and V_q.

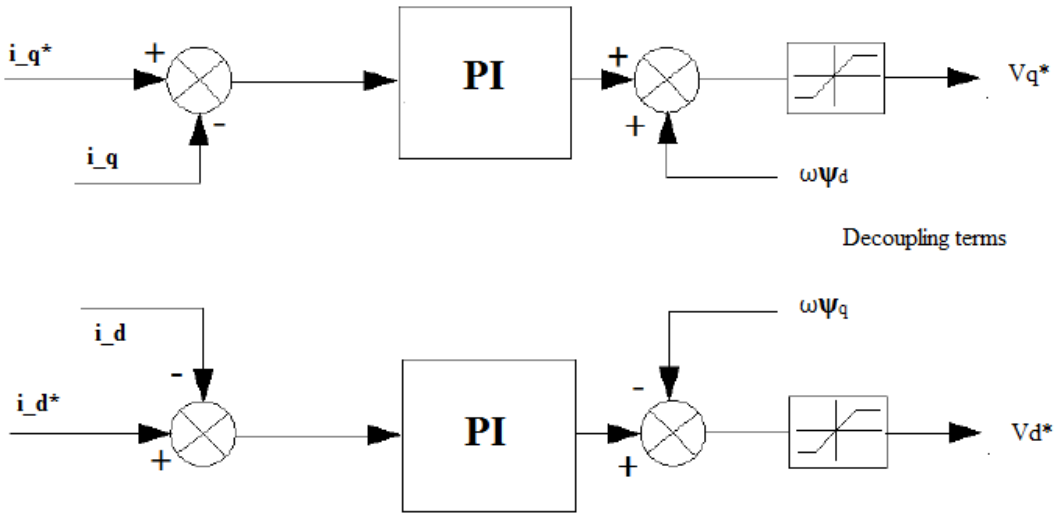

Figure 2.24. PI control loop for i_d & i_q. Current tracking controller.

Reference voltages are then applied to the terminals of the IPM after inverse Park & Clarke transformations. One of the most popular and efficient technique is called Space vector pulse width modulation (SVPWM). Details of Simulink implementation of IPM and controllers in closed loop form can be found in Appendix A.

2.2.3 Closed loop current control & simulation of IPM

Closed loop torque control is implemented as shown in Figure 2.25. Reference torque is first limited using maximum torque curve of the machine. Then optimal references for quadrature and direct axis currents, i_d, i_q, are calculated. Decoupled PI controller calculates the quadrature and direct axis voltages, V_d, V_q. Calculated voltages are then applied to terminals of IPM after inverse Park and Clarke transformations. SVPWM inverter model is avoided for reducing complexity and calculation cost of the model. However inverter power loss is calculated as presented in the next chapter and added to the cost function. This is used for modeling change in inverter loss due to battery voltage level or equivalently, the SOC of the battery.

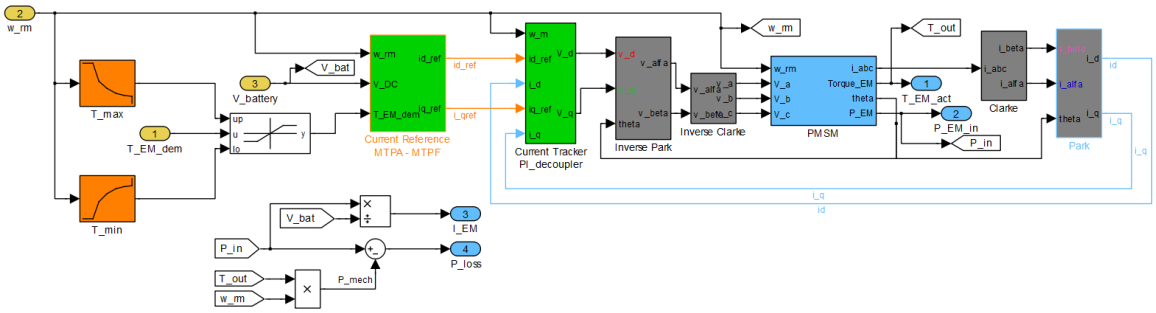

Figure 2.25. Overview of IPM and controllers in closed loop form. Torque request, speed and battery voltage are the inputs. Actual torque, battery current, power and power loss are the outputs.

Simulation results for MTPA and MPTF control are shown in Figure 2.26 and 2.27 respectively. Actual torque tracks the reference torque perfectly with decoupling control, settling time of the IPM is observed to be below 5 milliseconds as expected.

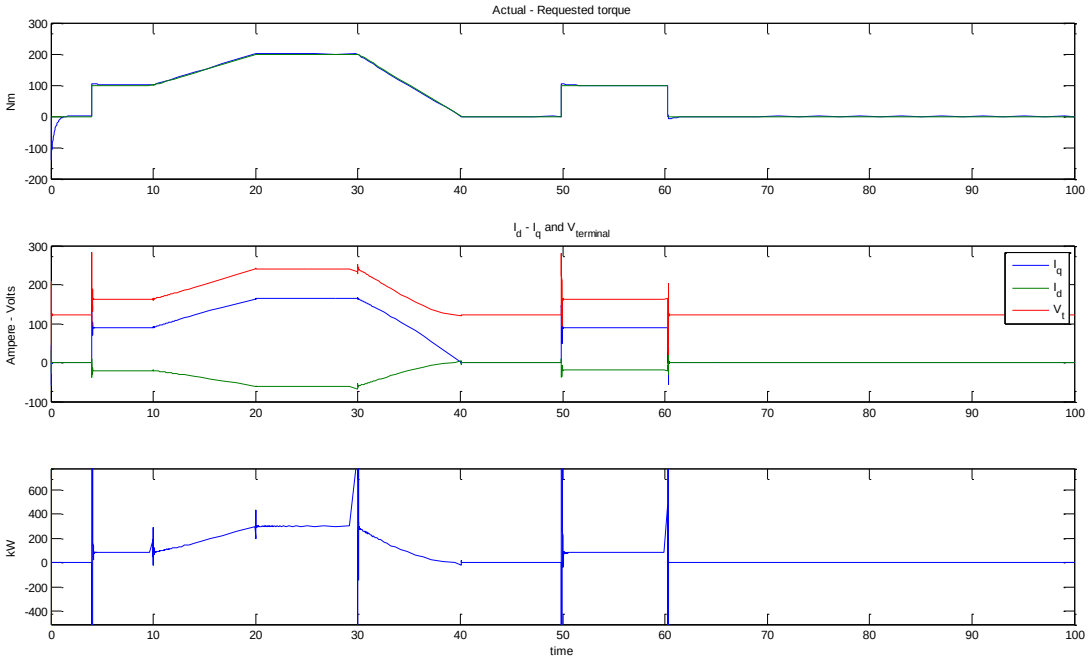

Figure 2.26. Simulation of IPM below base speed, MTPA control.

Peak errors can be observed at times of rapid torque reference changes. This is due to decoupling control strategy; decoupling logic should be improved in a way to reduce peak errors. Voltage references shall be corrected or filtered at the time of torque reference changes.

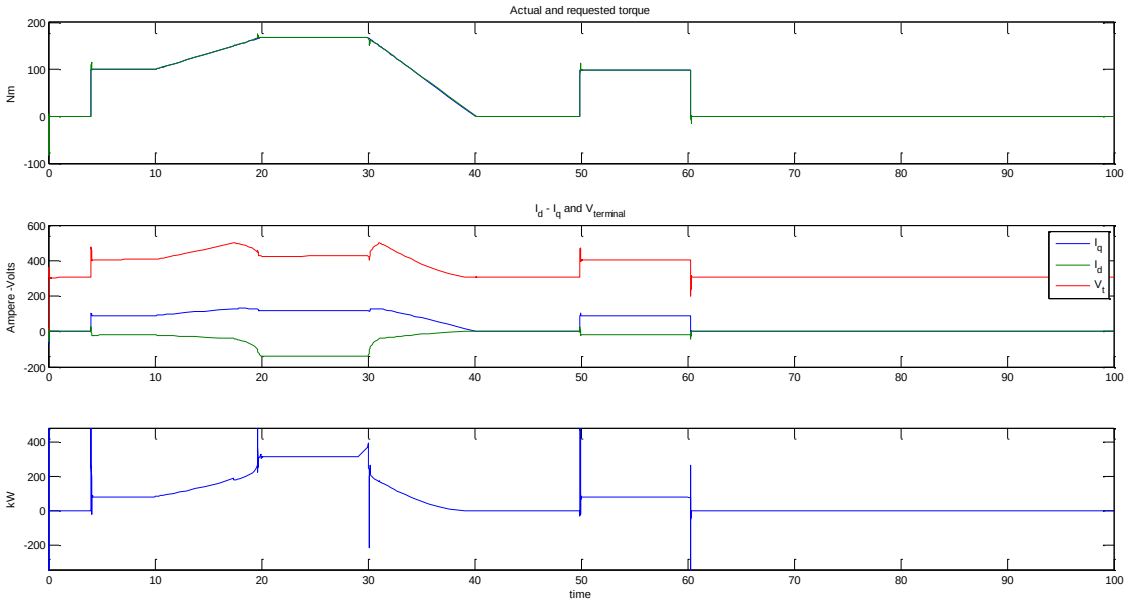

Figure 2.27. Simulation of IPM above base speed, MTPF control.

2.3 Inverter

In most HEV applications, inverters are implemented in a way to provide duplex operation. Which means inverter can push power to the EM or receive power from the electric motor. See Figure 2.28, there are 4 quadrants of operation of an EM. Inverter of the traction EM shall support at least 3 quadrants; forward driving (I), forward regenerative braking (II) and reverse driving (III). Reverse regenerative braking is not a binding requirement for a HEV but any inverter supporting first 3 quadrants will also support the 4^{th} quadrant.

DC voltage at the battery side of the inverter is converted to AC voltage at the EM side, through pulse width modulation (PWM) techniques. Direction of power flow depends on phase difference between voltage and current, given by Equation 2.41. ϕ is the angle between voltage and current vectors. By convention angle ϕ is positive when current lags voltage. In 1^{st} and 3^{rd} quadrants, power is positive and EM is receiving power whereas in 2^{nd} and 4^{rd} quadrants power is negative EM is delivering power.

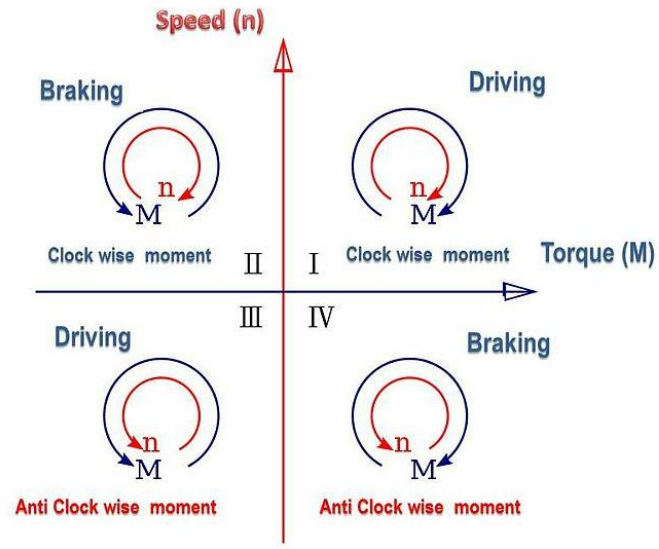

Figure 2.28. 4 quadrants of operation of an EM, EM receives power from the battery during driving and delivers power to the battery during braking [33].

$$P = {}^{3}/_{2}\, VI \cos\varphi \tag{2.41}$$

Inverters used for driving any 3-phase AC machine, including PMSM consist of 3 half bridges, as shown in Figure 2.29. Two transistors of each bridge always work as complement to each other, if the upper one is turned on, lower one should be turned off in order to avoid short circuit. Since turn-off time of a power transistor is longer than its turn-on time, dead time should be inserted when switching the complementary transistors. In order to avoid further complexity, dead time is not modeled.

In the previous chapter, voltage references; V_d* and V_q* are calculated using field oriented control techniques. Which are then converted to V_a*, V_b* and V_c* using inverse Park & Clarke transformations. A modulation scheme called space-vector PWM (SVPWM) will be used for controlling the switches, which will allow phase voltages to track its references. SVPWM is famous for its efficiency. It can also yield higher effective voltages at the terminals of EM than conventional PWM techniques.

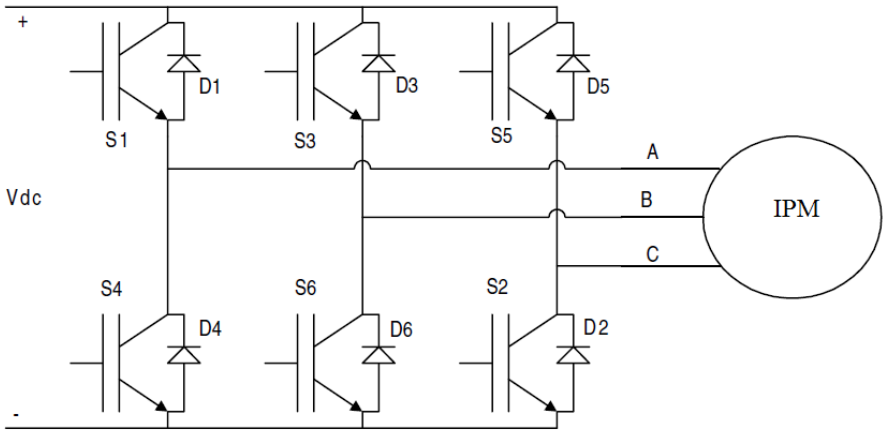

Figure 2.29. 3-phase inverter with 3 half bridges. S1-S4, S3-S6 and S2-S5 are complementary.

2.3.1 Space Vector Pulse Width Modulation (SVPWM)

A 3-phase inverter has 8 possible states, switch configurations, as shown in Figure 2.30. For 6 of these switch configurations, a voltage vector is applied to the terminals of the EM. However for 2 switch configurations no voltage is applied to the EM, since all terminals of EM are either connected to ground or high voltage [35].

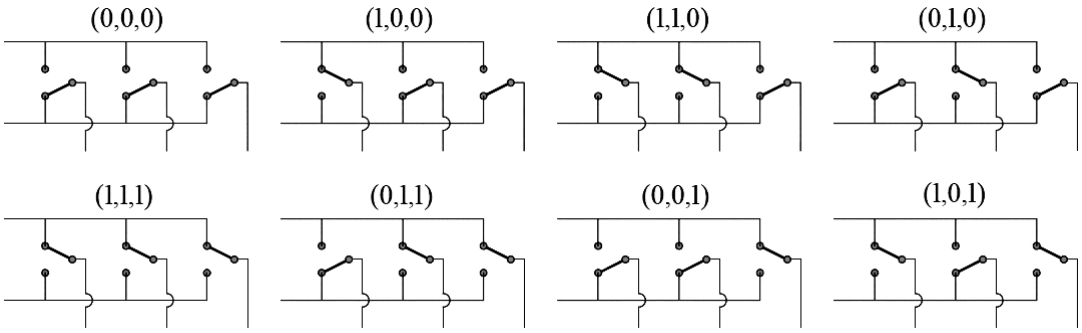

Figure 3.30. 8 switch states of the inverter, 1 stands for opening upper transistor and 0 stands for opening lower transistor [34].

Voltage vectors for 6 possible configurations for which voltage is applied to EM terminals are shown in Figure 2.31, using these fundamental voltage vectors any voltage vector with magnitude smaller than V_{DC} can be created. Voltage vector is created in a manner that it rotates synchronously with the rotor magnetic field in PMSMs. In order to

generate voltages at high speeds, high switching frequencies are utilized. Since every switching of transistor introduces more power loss, Symmetric SVPWM pulse generation technique is introduced in order to minimize number of switching hence the power loss.

Symmetric pulse generation for sector 1 is also shown in Figure 2.31. Time periods, t_a and t_b for applying fundamental vectors V_{100} and V_{110} and time period, t_0, for applying zero vectors V_{111} and V_{000} can be calculated through Equations 2.42 to 2.47. Details of calculations can be found in [35].

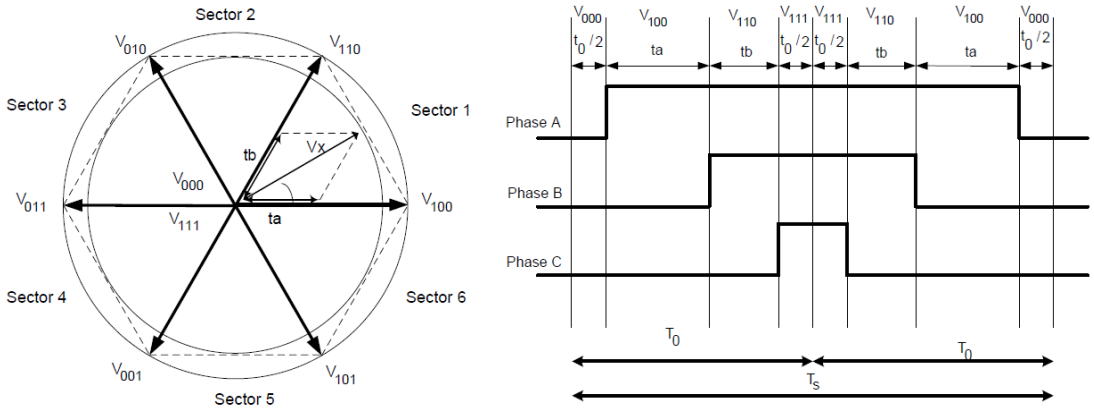

Figure 2.31. Fundamental voltage vectors for 6-possible switch configurations showed on the left. Symmetrical SVPWM pulse generation for sector 1 showed on the right.

$$V_a = \frac{2}{\sqrt{3}} V_x \sin\left(\frac{\pi}{3} - \alpha\right) \tag{2.42}$$

$$V_b = \frac{2}{\sqrt{3}} V_x \sin\alpha \tag{2.43}$$

Where V_a and V_b are projection of V_x on to the fundamental vectors V_{100} and V_{110} and α is the angle between V_{100} and V_x. So for a period of T_0, V_x can be achieved by applying fundamental vectors V_{100} and V_{110} for time periods t_a and t_b, see Equation 2.45. Zero voltage is applied for the rest of the period.

$$t_0 = T_0 - t_a - t_b \tag{2.44}$$

$$\overrightarrow{V_x} = \overrightarrow{V_a} + \overrightarrow{V_b} = \frac{t_a}{T_0}\overrightarrow{V_{100}} + \frac{t_b}{T_0}\overrightarrow{V_{110}} + \frac{t_0}{2T_0}\overrightarrow{V_{000}} + \frac{t_0}{2T_0}\overrightarrow{V_{111}} \quad (2.45)$$

Finally t_a and t_b can be calculated and symmetrical pulse is generated for two consecutive periods of T_0. See Figure 2.31, T_S depends on the PWM carrier frequency, which is usually between than 10-20 kHz for PMSM drives. $T_S = 1/f_S$ is then between 50μs to 100μs.

$$t_a = \frac{T_0 V_x}{V_{100}}\left[\cos\alpha - \frac{1}{\sqrt{3}}\sin\alpha\right] \quad (46)$$

$$t_b = \frac{2}{\sqrt{3}}\frac{T_0 V_x}{V_{110}}\sin\alpha \quad (47)$$

2.3.2 Modeling Inverter loss for SVPWM control

Inverter losses consist of switching losses and on-state losses. Power loss can be modeled easily as momentary voltage over the transistor times the current. Both switching and on-state losses depend heavily on the type of transistors that are being used. MOSFET transistors have shorter switching times, hence lower switching losses compared to IGBTs. But on-state losses of IGBTs are much lower compared to MOSFETs [12]. Switching loss also depends on the type of switching that is being utilized, hard or soft switching. For soft switching, either voltage or current is kept close to zero during switching in order to minimize switching losses [12]. Hard switching is easier to implement but results in much larger power losses as shown in Figure 2.32.

Switching and on-state power losses are given by Equations 2.48 and 2.49 respectively. Where f_S is the switching frequency, $T_S = 1/f_S$ is the switching period, V_{off} is the voltage on the transistor when it is off. I_{on} is the on-state current and V_{on} is the voltage on the transistor when it is on. T_S is the period and t_{on} is the on time. Finally $t_c(on)$ and $t_c(off)$ are the switching on and off times.

$$P_{sw\_loss} = {}^1\!/_2\, V_{off} I_{on} f_S\left(t_c(on) + t_c(off)\right) \quad (2.48)$$

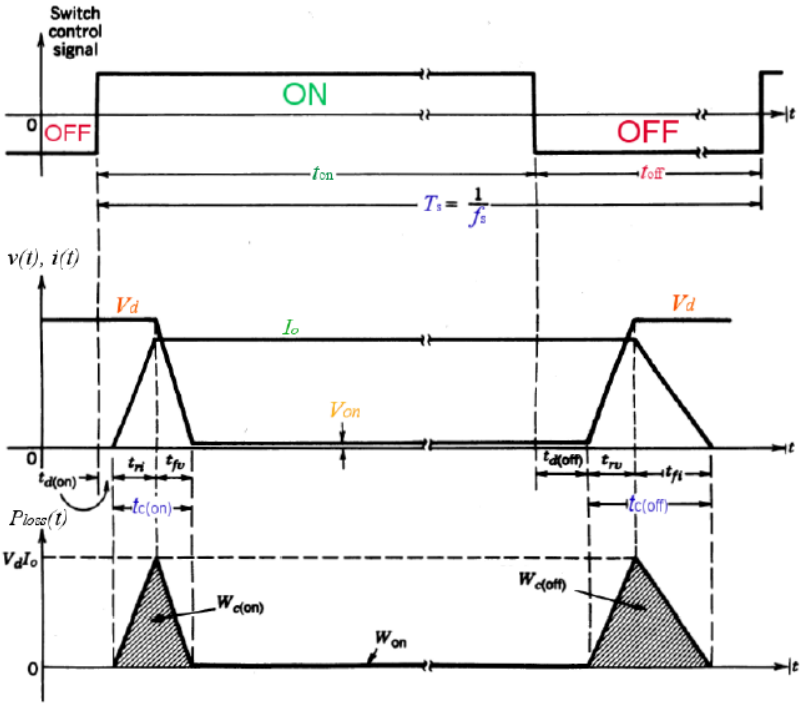

Figure 2.32. Transistor losses during hard switching [12].

$$P_{on\_loss} = V_{on} I_{on} \frac{t_{on}}{T_S} \tag{2.49}$$

Observe Figure 2.28 and Figure 2.29, for SVPWM 3 transistors are always on and 3 are off. Hence on-state losses can be easily formulated. However switching losses are hard to evaluate since voltage on transistor during off state is hard to formulate. But for simplicity voltage on the transistor during off state is accepted as equal to DC bus voltage, $V_{off} = V_{dc}$. All 6 transistors switch on and off for once during period T_S. So power loss for SVPWM technique is given by equation 2.50. I_{on} is the magnitude of the current at each phase at that time.

$$P_{SVPWM\_loss} \approx 3\, V_{on} I_{on} + 3\, V_{dc} I_{on} f_S \left(t_c(on) + t_c(off)\right) \tag{2.50}$$

Efficiency of an inverter for an EV application is typically higher than 96%. Inverter efficiency can be accepted as constant since operating points does not change efficiency dramatically [12]. Analyzing Equation 2.50, left hand side of the loss is not affected by the controllable operating point of the inverter. Controllable operating point is defined by input and output voltage of the inverter (V_{in}-V_{out}, $V_{in} = V_{dc} = V_{bat}$). Only right hand side of the

loss equation is affected by the operating point (voltage or SOC level of the battery), if switching scheme is hard switching. For soft switching scheme, right hand side of the equation is significantly lower and independent of operating point. For a modern inverter utilizing soft switching scheme, loss does not vary significantly with input operating point, the battery voltage level.

Simulation results also indicate that inverter loss is varies according to operating point of the electric motor, rather than voltage level of the battery. Operating point of the EM depends on the drive cycle and vehicle demand. Hence it cannot be altered, if driver request is to be covered. Therefore power loss of the inverter cannot be minimized by varying the state of the system, SOC level of the battery. Inverter power loss doesn't need to be included in overall cost function at the time.

2.4 Range Extender Unit

Internal combustion engines (ICE) act as the primary power source in most SHEVs. However as battery capacity of a SHEV increases, ICE starts acting as a secondary power source, delivering power only when SOC is low or traction power demand is high. As is the case for REEVs, battery is charged from the grid and battery energy alone is sufficient for more than 80-90 percent of the time.

There are two types of ICEs, spark ignition (SI) and compression ignition (CI). CI engines create combustion by compressing diesel and air mixture to high pressures. SI engines compress gasoline and air mixture just like CI engines, however compression ratio is much lower thus combustion is started by spark plugs.

CI engines operate at higher efficiencies, in terms of MJ per liter. However there are strict regulations on NO_x emissions and even more strict ones are on the way. In order to comply with these restrictions, complex after treatment systems shall be implemented, which occupy large spaces. Also ICE will be turned on and off trying to maintain SOC at levels of high efficiency, which will also cause increased NO_x emissions. CI engines may be suitable for SHEV applications where space limitation is not an issue, such as hybrid

bus or truck. Due to higher power density and lower complexity, SI engines are more suitable for REEVs.

Most common and developed SI engine is the four stroke Otto-cycle. Operating principle of a SI engine can be explained by Figure 2.33 and Figure 2.34.

- Intake (induction) stroke 5 -> 1: Gasoline vapor and air mixture is drawn into combustion chamber, suction for the process is created by expanding the volume.
- Compression stroke 1-> 2 : Gasoline vapor and air mixture is compressed, both temperature and pressure is increased.
- Combustion and power stroke (Ignition): Combustion happens in a very short time period, essentially constant volume 2->3, and then power stroke takes place, where high pressure is converted to mechanical work through expansion 3-> 4. Some part of 4 -> 1 is also included in this stroke where some of the heat is transferred to reservoirs.
- Exhaust stroke: Exhaust valve opens and burned fuel and air mixture is pushed out of the combustion chamber 1 -> 5. Includes the rest of the 4 -> 1, heat loss.

Control of the ICE in range extended vehicles is much easier compared to regular gasoline powered vehicles since ICE is not connected to drive shaft in series hybrid configuration. Hence operating points of ICE can be limited such that points of instability, low efficiency and high emissions can be avoided. Also smaller ICEs can be used in REEVs since ICE is no longer responsible for short-term high power demands. 45 kW SI engine is used as range extender, maximum torque and power versus speed curve is given in Figure 2.35.

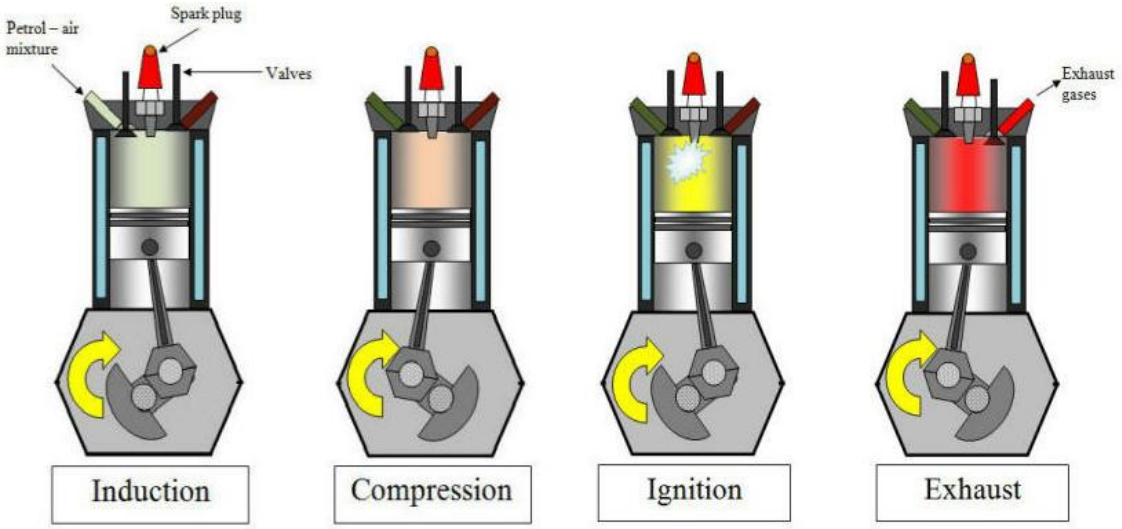

Figure 2.33. Four-stroke otto-cycle diagram [36].

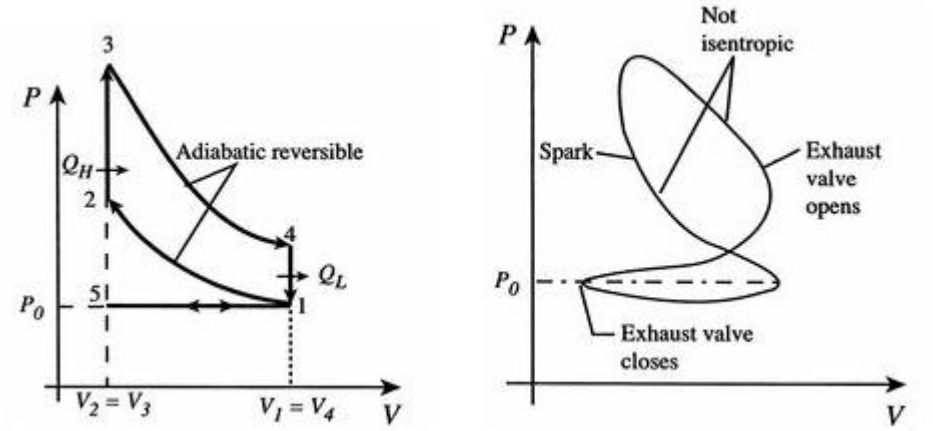

Figure 2.34. P-V diagram for ideal Otto-cycle and actual Otto-cycle respectively [36].

Efficiency contour of the 45 kW SI engine is given in Figure 2.36. As mentioned, expectation from the ICE in a series hybrid configuration is only electrical power. Rest of the vehicle does not care how the necessary power is generated. Hence when a power request (P_{req}) is made by the supervisory controller, optimal torque-speed can be calculated using constant power curves as shown in Figure 2.36.

Ignoring issues regarding emissions and stability for now, on a constant power curve T-ω point with highest efficiency will be selected as the optimal operating point (T^*-ω^*). The optimal operating path is fitted to 2^{nd} order polynomial, as given by equations

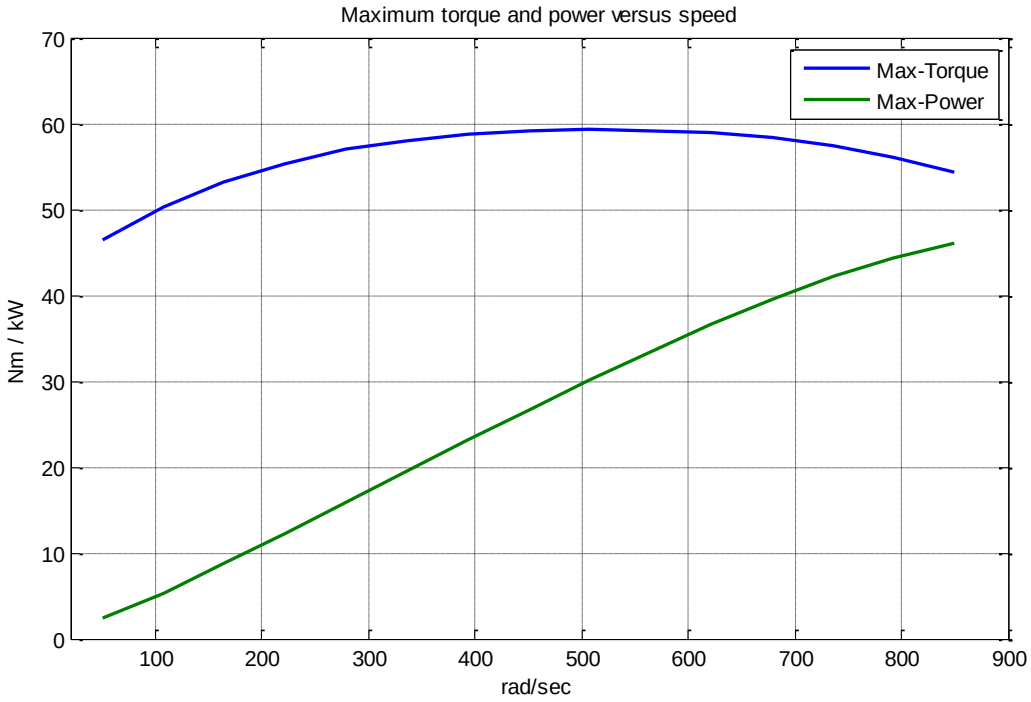

Figure 2.35. 45kW SI engine, Max power @ 800 rad/sec and Max torque @ 500 rad/sec.

$$\eta(T_{ICE}, \omega_{ICE}) \leq \eta(T_{ICE}^{*}, \omega_{ICE}^{*}), \forall\, T_{ICE}\omega_{ICE} = P_{req} \tag{2.51}$$

For a given speed, optimal operating torque is given by:

$$T_{ICE}^{*} = -6.704e-005 * \omega^2 + 0.07982 * \omega + 34.43 \tag{2.52}$$

Supervisory controller does not have to know about the operating point. But power loss versus ICE output power relation must be known by the supervisory controller in order for it to minimize the power loss of the whole system. Hence efficiency versus output power curve is fitted to 3rd order polynomial as given by Equation 2.53. This can be converted to power loss versus output power form using simple manipulations.

$$\eta(P_{ICE}) = -1.616e-006 * {P_{ICE}}^3 + .13e-005 * {P_{ICE}}^2 + 0.001259 * P_{ICE} + 0.3128 \tag{2.53}$$

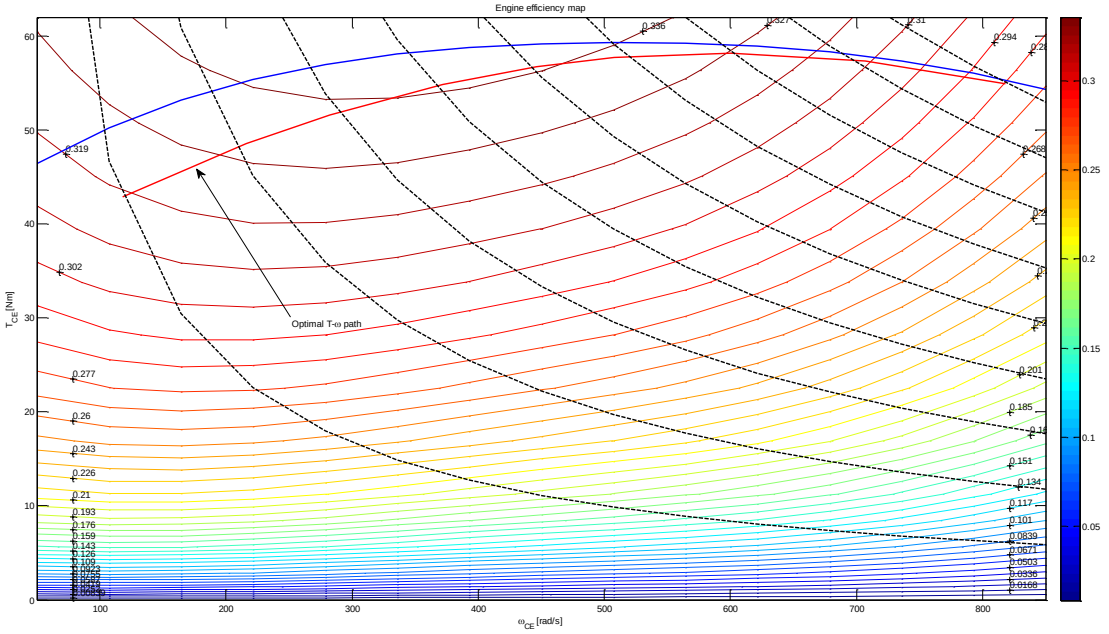

Figure 2.36. Efficiency contour of 45 kW SI engine, dashed black lines represent constant power curves and red solid line shows the optimal operating path (T-ω) [3].

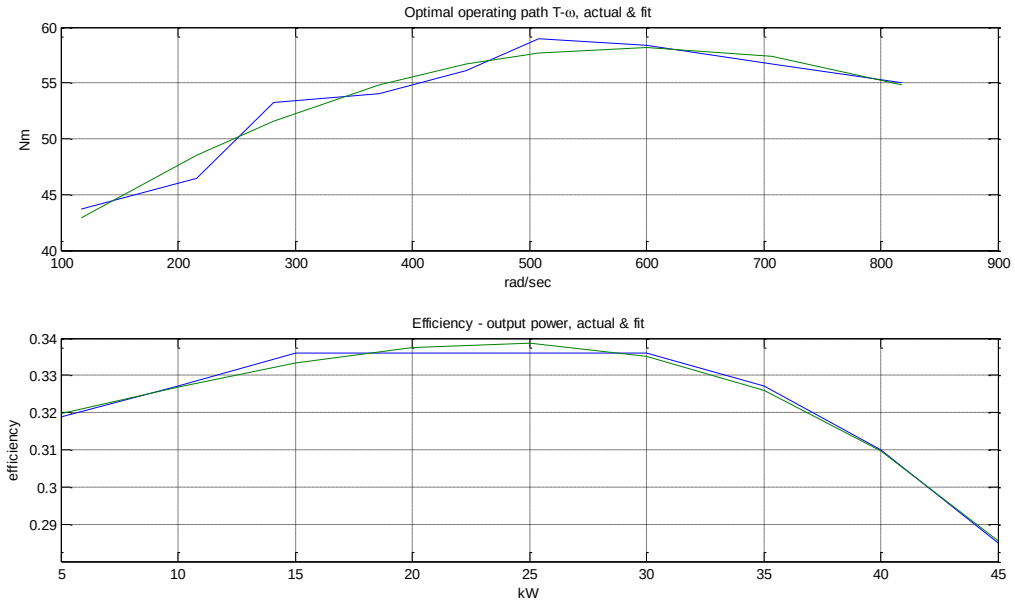

Figure 2.37. Actual and fitted data for optimal operating path and efficiency versus output power.

2.4.1 Quasi-static Modeling of ICE and Generator set

Several methodologies exist for modeling dynamics of internal combustion engine. Mean value modeling and discrete event modeling techniques are mentioned in [37]. In a regular gasoline vehicle these modeling techniques are used for minimizing fuel consumption, torque ripple, emissions while generating requested torque at given speed determined by wheel speed and gear ratio.

Even though operation of Range Extender, ICE-generator set, is limited to certain high efficiency points (T-ω), low level controllers are necessary. Fueling rate, throttle valve, three-way catalytic converter, and exhaust gas recirculation valve shall be controlled in a way to reduce hydrocarbon (HC), carbon monoxide (CO) and nitrogen oxide (NO_x) emissions.

Dynamic modeling of ICE is omitted, because it is too complex, it would require even more complex controllers and increased complexity will not improve the performance of the supervisory controller. Also it will not be feasible to include these complex dynamics in the optimal energy management problem.

Unlike other parts of the vehicle, RE is modeled with using quasi-static approach proposed by [3]. Engine efficiency versus operating point contour given in previous section is coupled with generator in way to maximize efficiency via a gear ratio. Optimal gear ratio, coupling ICE and generator, can be determined by simulation. Drive cycle distribution can be constructed and gear ratio can be optimized globally. But an easier assumption can be made here: Since ICE will be used as a secondary power source it can operate only at power levels which support highest efficiencies. Lower power levels (average over an hour) can be achieved by on-off operation, much like duty cycle but with longer period. Hence, highest efficiency region of generator and ICE needs to be coincided, such that a region with highest possible efficiency is formed. Efficiency in most other operating points may be affected badly, since object is to maximize only the peak value of the RE efficiency map.

High efficiency and high power regions should also coincide, since it is possible to operate at lower power levels with the same efficiency, via on-off operation. However it will not possible to operate at highest efficiency in high power levels if highest efficiency region is coincided with low power regions. Efficiency contour of the electric motor in 4th quadrature, refer to SVPWM chapter, along with maximum torque curve is given in Figure 2.38.

Gear ratio between ICE and generator is determined after several observations as 0.66, placing 30-35 kW output power to highest efficiency region. Overall efficiency contour of RE with gear ratio of 0.6 is given in Figure 2.39, which is calculated as given by Equation 2.54.

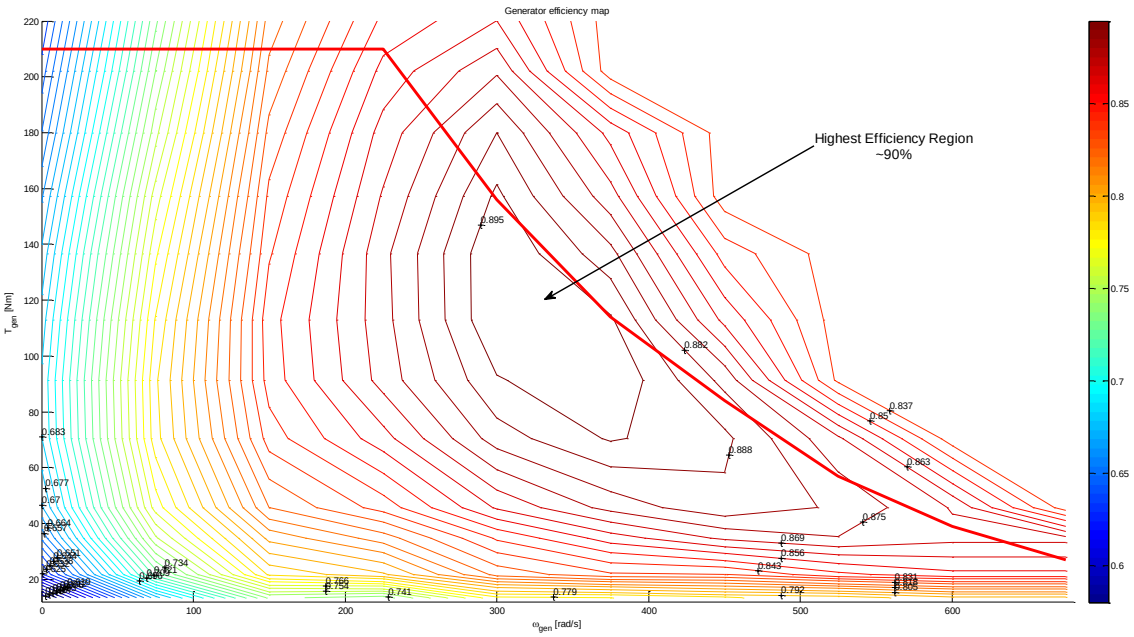

Figure 2.38. Efficiency contour of a 48kW – 210Nm electric machine in 4th quadrant, acting as generator. Solid red line represents maximum torque at given speed.

$$\eta_{RE}(T,\omega) = \eta_{ICE}(T,\omega)\,\eta_{GEN}(T,\omega) \tag{2.54}$$

Optimal operation path is found through use of constant power curves. Optimal operating point (T^*-ω^*) is the T-ω point with highest efficiency on o constant power curve. Results can be observed in Figure 2.40. Maximum available power that can be generated

by RE is now limited to 39kW * 0.884 = 34.4kW, which is another result of efficiency region optimization that some power range is lost.

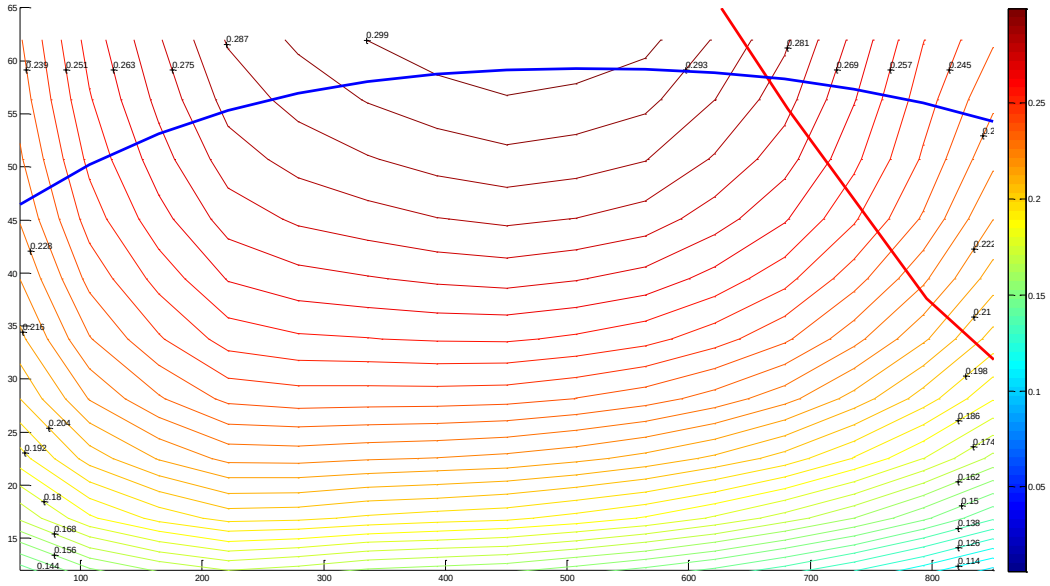

Figure 2.39. Overall efficiency contour of RE with gear ratio of 0.66, η> 0.3 is achieved for power ranges of 23-33kW.

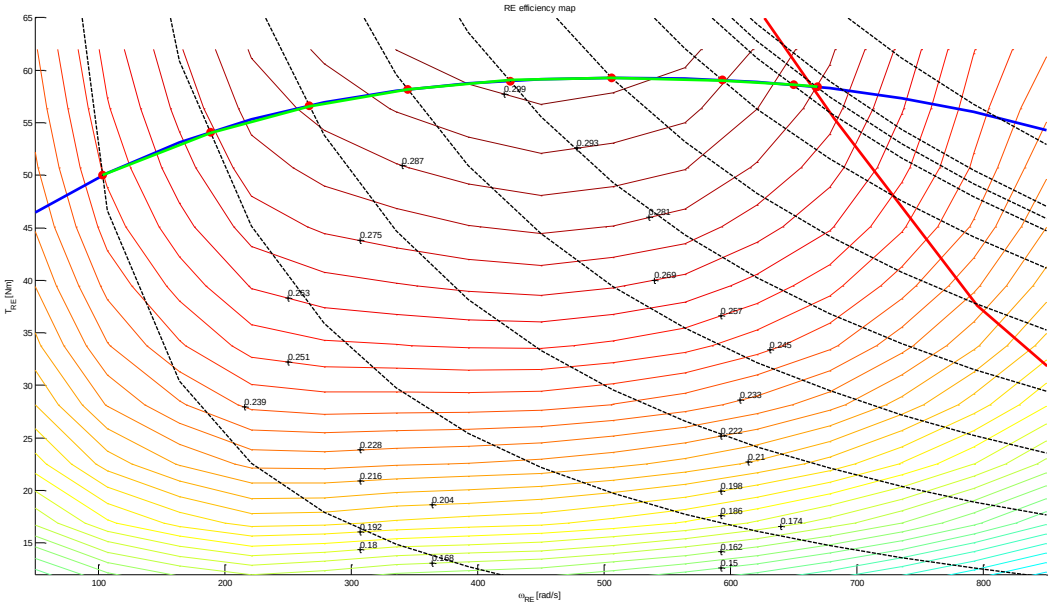

Figure 2.40. Optimal operating path for RE, red ‘o’ represent the data points with highest efficiency for a given constant power curve, green solid line is the fitted 3rd order polynomial.

Observe that optimal operation is on the maximum torque curve of the ICE, which is dictated by efficiency contour of the ICE. However in reality optimal operation region for ICE is below the maximum torque curve.

3rd order polynomial is used for fitting the optimal operation points. 4th order polynomial is used for fitting efficiency versus power data. Polynomials are given by Equations 2.55 and 2.56 respectively. Plots of data and polynomial fits are given in Figure 2.41.

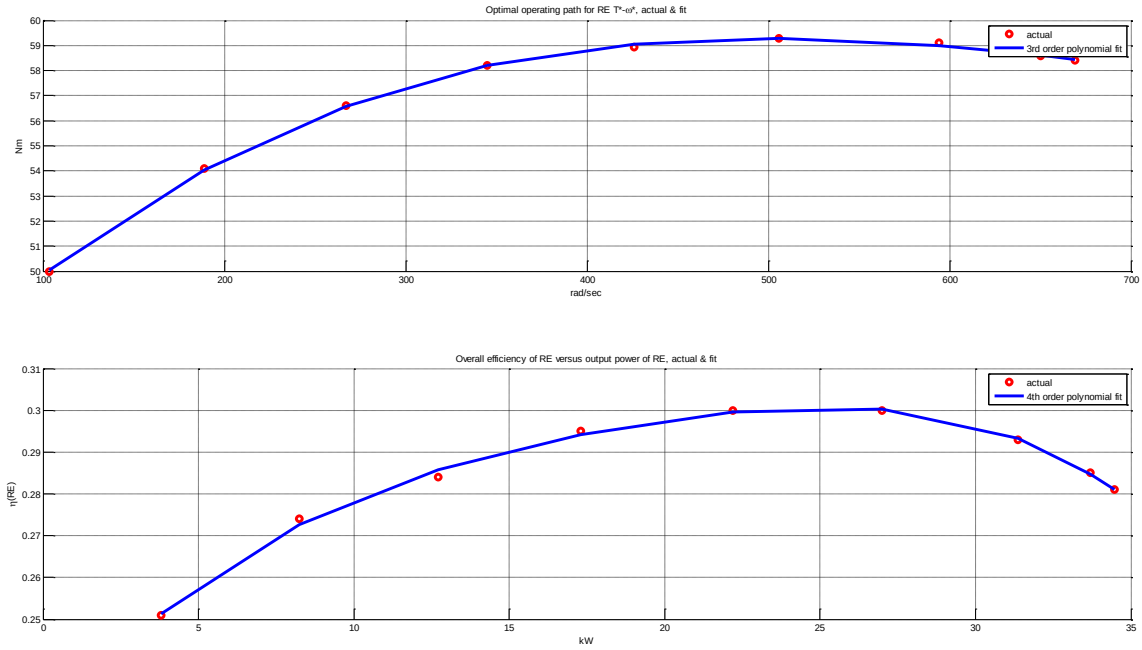

Figure 2.41. Top, optimal operating path for RE – (T*-ω*). Bottom is the efficiency versus output power curve for RE. Red 'o' represent data and solid blue lines are the polynomial fitted curves.

$$T_{RE}{}^{*} = 5.405e-008 * \omega^3 + -0.0001188 * \omega^2 + 0.07812 * \omega + 43.16 \quad (2.55)$$

$$\eta(P_{RE}) = -2.374e-007 * P_{RE}{}^{4} + 1.717e-005 * P_{RE}{}^{3} - 0.0005379 * P_{RE}{}^{2} + 0.009587 * P_{RE} + 0.2218 \quad (2.56)$$

Equation 2.56 is further simplified, data is fitted with 2nd order polynomial, see Figure 2.42. Power loss is calculated by Equation 2.58. Efficiency versus power data is fitted to 2nd order polynomial, Equation 2.57.

$$\eta\left(P_{RE\_out}\right) = -0.0001327 * {P_{RE\_out}}^2 + 0.006104 * P_{RE\_out} + 0.2302 \quad (2.57)$$

$$P_{loss}(t) = \frac{P_{RE_{out}}(t)}{\eta\left(P_{RE_{out}}(t)\right)} - P_{RE_{out}}(t)$$

$$= \frac{P_{RE\_out} + 0.0001327 * {P_{RE_{out}}}^3 - 0.006104 * {P_{RE_{out}}}^2 - 0.2302 * P_{RE\_out}}{-0.0001327 * {P_{RE\_out}}^2 + 0.006104 * P_{RE\_out} + 0.2302} \quad (2.58)$$

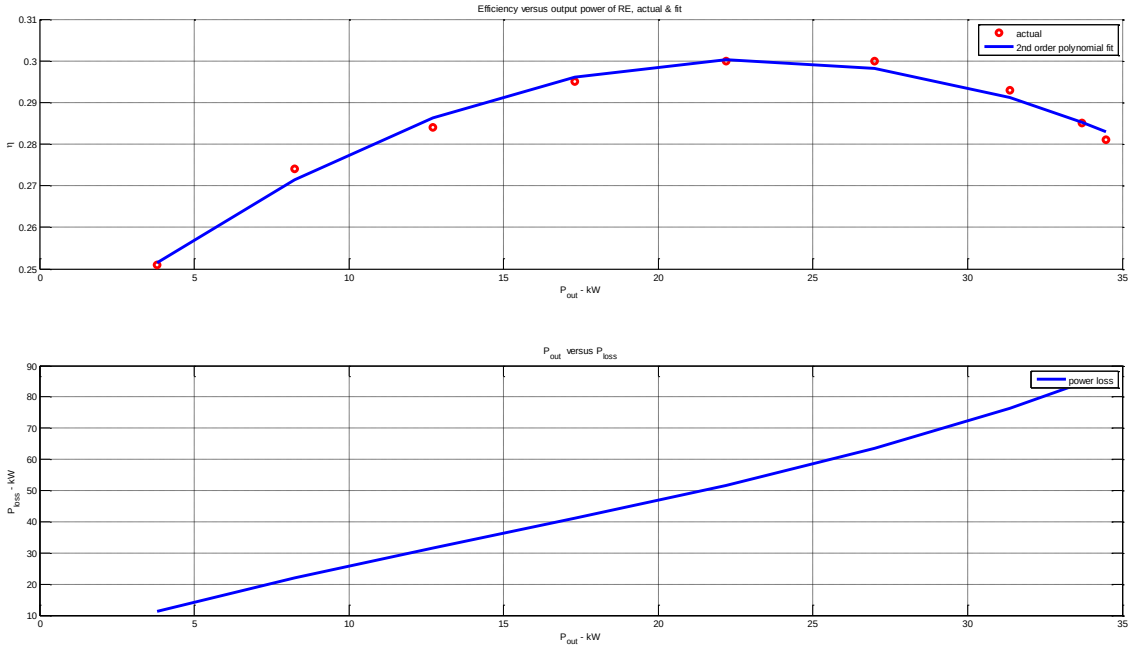

Figure 2.42. Top, efficiency data fitted with 2nd order polynomial. Bottom, total power loss of the RE plot for various output power levels.

Simulink Model for Range Extender is given in Figure 2.43. First power request from the RE is converted to power request from engine via generator efficiency map. Then optimal operating point (T^*-ω^*) is calculated from the engine power request. Finally fuel consumption is extracted from the look-up table and integrated in order to model fuel

consumption. Engine output power can also be generated from multiplication of consumption, efficiency and lower heating value.

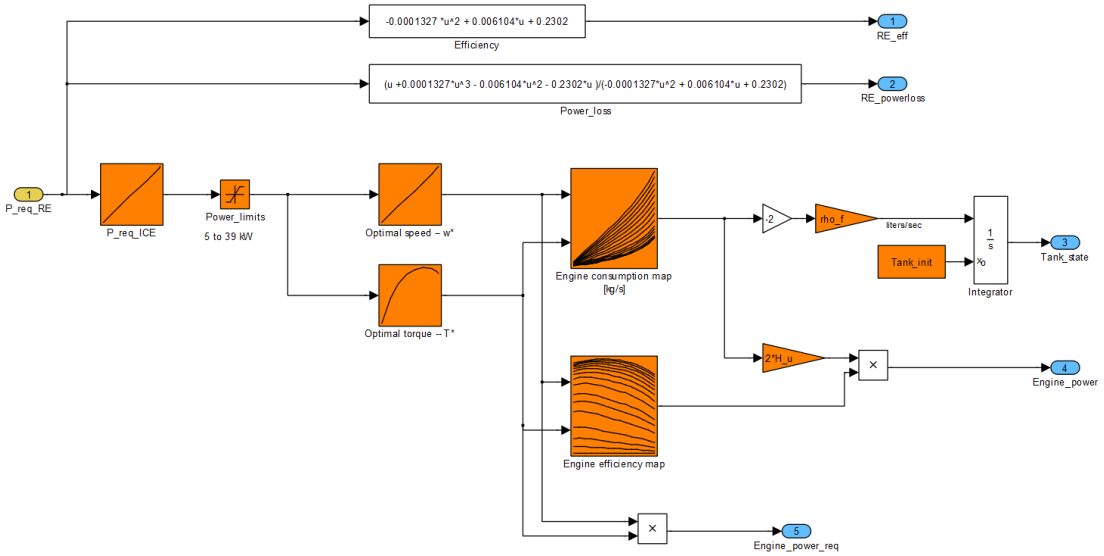

Figure 2.43. Simulink model of the Range Extender. Unlike other parts of the vehicle, ICE and generator of RE are modeled via look-up tables.

2.5 Vehicle Model

Four major forces act on a moving vehicle other than traction force. These forces are:

- Aerodynamic friction forces (F_{aero})
- Rolling friction forces ($F_{Rolling}$)
- Uphill/downhill driving forces ($F_{Gravity}$)
- Inertial forces ($F_{Inertial}$)

$$m_v \frac{d}{dt} v(t) = F_{traction} - F_{aero} - F_{rolling} - F_{gravity} - F_{inertial} \quad (2.59)$$

Longitudinal dynamics of a vehicle can be modeled as given by Equation 2.59. m_v is the mass and v is the speed of the vehicle. Forces can be observed on body diagram in Figure 2.44. As can be imagined, aerodynamic friction force and rolling friction force are not conservative; these two forces are used for representing losses due to air drag and

rolling resistance. However, uphill driving and inertial forces are conservative, one represents kinetic energy and other one represents potential energy. It may be possible to recover them via electric machine.

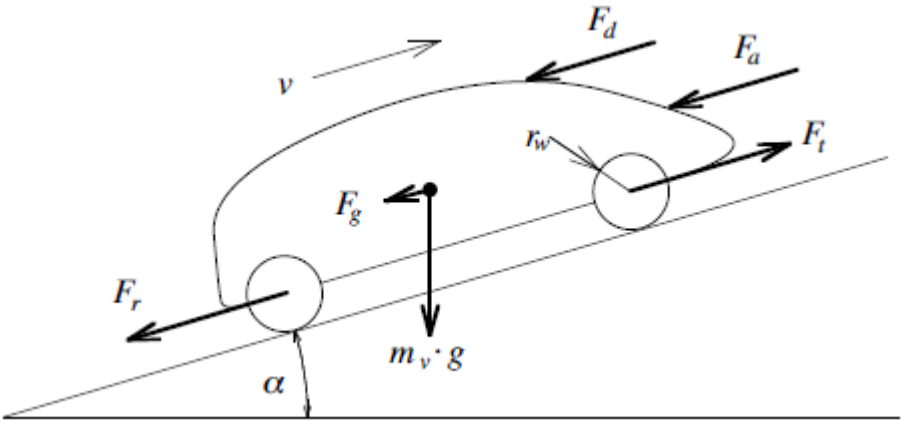

Figure 2.44. Forces acting on a vehicle in motion [7].

2.5.1 Aerodynamic friction losses

Air drag force consists of two main components [12], shape drag and skin friction. Shape drag force is caused by the pressure difference between the front and the rear of the vehicle. Skin friction is created due to the fact that air molecules moving with different speeds create friction. Air molecules closer to vehicle body will move faster than the air far away, hence friction will be created.

$$F_{aero} = \frac{1}{2} \cdot \rho_a \cdot A_f \cdot c_d \cdot v^2 \tag{2.60}$$

Aerodynamic force is modeled by simplifying vehicle to a prismatic body as given by Equation 2.60. A_f represents frontal area of the vehicle. ρ_a is the density of ambient air, v is the vehicle speed and c_d is the aerodynamic drag coefficient, which characterizes the shape of the vehicle. It varies between 0.15 for an optimum car to 0.5 for an off-road car.

2.5.2 Rolling friction losses

Rolling friction force is modeled as given by Equation 2.61. C_r is the friction constant, m_v is the mass of the vehicle and g is the gravitational constant.

$$F_{rolling} = C_r \, . \, m_v \, . g \tag{2.61}$$

Friction constant Cr depends on many parameters such as material of the tire, temperature, tire pressure, road material and conditions etc.

2.5.3 Uphill/downhill driving forces

As shown in Figure 2.44, uphill/downhill force represents the gravitational force when vehicle is moving on a non-flat surface. Depending on the slope and direction of motion, it may oppose or contribute to motion. This force can be considered as conservative since it builds up potential energy of the vehicle. Uphill/downhill driving force is given by Equation 2.62. m_v is the mass of the vehicle and g is the gravitational constant and α is the road angle in radians.

$$F_{Gravity =} \, m_v \, . \, g \, . \, \sin \alpha \tag{2.62}$$

2.5.4 Inertial forces

For simplicity all inertial forces and vehicle mass are added together after suitable transformations. All other forces are also converted to torque, which allows modeling dynamics of the vehicle in torque domain. Conversion to torque domain requires assumption of slip free operation, such that vehicle speed can be directly related to rotational speeds. Equivalent inertia, I_{eq}, of the whole vehicle is given by Equation 2.63.

$$I_{eq} = m_v \, . \, r_{wheel}{}^2 + I_{wheel} + I_{shaft\_out} + GR_{fd}{}^2 * (I_{EM} + I_{shaft\_in}) \tag{2.63}$$

Where r_{wheel} is the radius of the wheels in meters, I_{wheel} is the total inertia of 4 wheels, I_{shaft_out} is the total inertia of the output shaft, after final drive, I_{shaft_in} is the inertia of the input shaft, before final drive, I_{EM} is the inertia of the traction motor andGR_{fd} is the final drive ratio, gear ratio between EM and wheels

2.5.5 Vehicle Dynamics

Dynamics of the vehicle in torque domain can be given as in Equation 2.64 after calculation of equivalent overall inertia. T_{EM} is the torque generated by the traction motor and T_{brake} is the mechanical brake torque. Implemented simulink model is shown in Figure 2.45, vehicle parameters are from [3].

$$\frac{d}{dt}\omega(t) = \frac{1}{I_{eq}}\left[GR_{fd}.T_{EM} - T_{brake} - r_{wheel}\left(\frac{1}{2}.\rho_a.A_f.c_d.v^2 - m_v.g.\sin(\alpha) - C_r.m_v.g\right)\right] \tag{2.64}$$

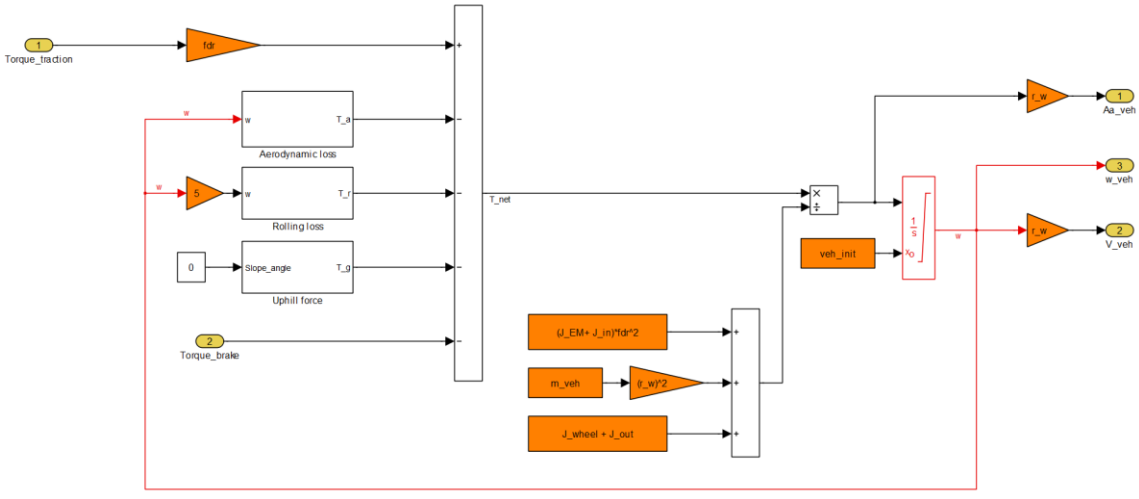

Figure 2.45. Longitudinal dynamics of the vehicle, inputs are torque electric motor and brake torque, output is the rotational speed of the output shaft, in radians per seconds.

2.6 Driver and Torque Manager

2.6.1 Driver Model

Driver model receives reference speed from the selected drive cycle (NEDC) and actual speed from the vehicle dynamics. Driver is responsible for tracking the reference speed by controlling brake pedal and accelerator pedal. Driver is modeled and implemented as shown in Figure 2.46. Driver behavior is modeled with a PI controller, where error is the difference between reference speed and actual speed is the input of the PI controller.

Assuming an ideal driver, brake pedal and accelerator pedal should never be pressed at the same time. Hence if the output of the PI controller is positive, accelerator pedal position set to output of PI controller and brake pedal is set to zero. However if output of the PI controller is negative, reference speed smaller than actual, brake pedal position is to the output of the PI controller and accelerator pedal is set to zero.

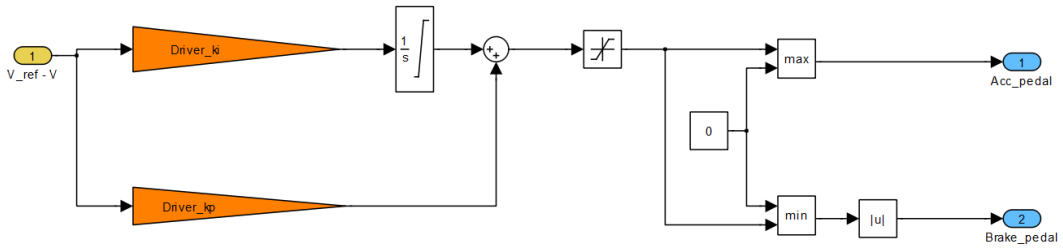

Figure 2.46. Simulink model of the driver.

2.6.2 Torque Manager

Most HEV applications accommodate torque managers in order to control traction motor of the vehicle while satisfying constraints imposed by powertrain components. In real applications torque managers are responsible for limiting electric motor torque reference due to several constraints such as:

- Battery Temperature: Available battery power diminishes as the temperature of battery deviates from optimum operating temperature. For example, available battery power diminishes significantly for temperatures lower 0 C°. For regenerative braking, temperature of the battery limits acceptable power.
- Battery SOC: Available battery power diminishes significantly at low SOC levels. Drawing high currents from the battery at low SOC levels can also cause permanent capacity loss. Battery SOC also determines acceptable power. Acceptable power is zero after certain SOC levels in order to prevent capacity loss. Acceptable power is also low at low SOC levels; it would take significantly longer time if battery is discharged to a very low SOC.
- Temperature of Electric Motor and Inverter: Temperature of EM and its inverter limit available traction power due to current limits. Torque request of the driver is limited if temperature limitation is imposed by motor or inverter.

Even though more complex torque managers are necessary for real time applications, however for simulation purposes temperature effects and limitations are neglected. Torque manager is implemented in Simulink, with following properties:

- Driver torque request is calculated from accelerator and brake pedals, for simplicity accelerator pedal position is multiplied by 4 and brake pedal is multiplied by -4. Value of 4 is selected for requesting maximum torque of the EM (400Nm). In real applications, look-up tables are used for converting pedal inputs to torque references.
- When driver torque request is positive: Torque request from the EM is limited by maximum torque versus speed curve of the traction motor (IPM) at 1^{st} quadrant.
- When driver torque request is negative, EM acts as a generator: Torque request from the EM is calculated by maximum negative torque versus speed curve. If negative torque request of the driver cannot be met by the traction motor, mechanical brake is used for applying the remaining torque. In order to maximize regeneration rate, mechanical brake is limited to cases where regenerative brake of traction motor is not sufficient on its own.

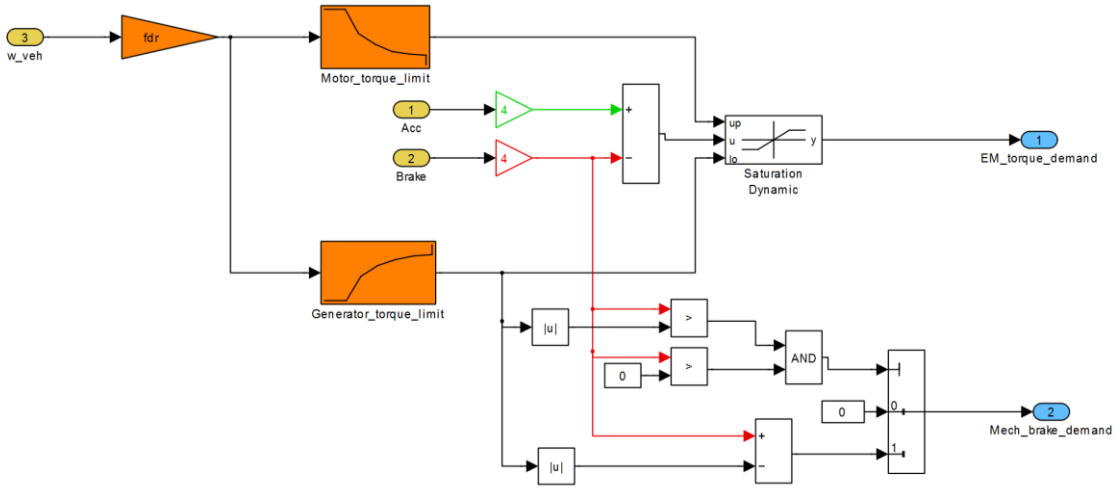

Figure 2.47 Simulink model of the Torque manager, accelerator and brake pedal is multiplied by 4 in order to achieve peak torque value, 400Nm, of the traction motor (IPM).

In simulation environment, torque manager's main duty is to split the deceleration torque request into regenerative and dissipative torque. Regenerative part is requested from EM and dissipative is requested from brake discs. As mentioned above, in real applications there are many other limitations on regenerative torque.

3. OPTIMAL CONTROLLER DESIGN

Optimal control problem is defined as finding the optimal control u*(t) which minimizes the objective function, J(u).

$$J(u) = h[x(t_f), t_f] + \int_0^{t_f} g(x(t), u(t), t)\, dt \tag{3.1}$$

where $h[x(t_f), t_f]$ represent the cost associated with the final state and $g(x(t), u(t), t)$ represent the cost of applying control u(t) at time t when state is x(t). Where the state update function is defined by

$$\dot{x}(t) = a\,(x(t), u(t), t) \tag{3.2}$$

Although there are several ways to solve above mentioned problems, two solution techniques are the most common and developed for such problems. Which are:

- Minimum Principle: Through use of calculation of variations above problem is turned into a two-point boundary value problem, which can be solved by iterative numerical methods.
- Dynamic Programming: Problem can be transformed into a sequence of single-stage processes. Starting from the final state and final time optimal controls for previous time step for different states are determined. Moving backwards in time, optimal controls for all admissible states are found for all time steps [21].

3.1 Dynamic Programming

Problem defined by Equations 3.1 and 3.2 are transformed to discrete form in order to allow use of dynamic programming. Details of dynamic programming will not be presented in this thesis, interested reader can find the details in [21].

State of the system is defined as a function of previous state and control

$$x(k+1) = a_D(x(k), u(k)) \tag{3.3}$$

Cost function is then updated to discrete form, where N is the final time, h is the function of final state cost and g_D is cost to go function.

$$J = h\big(x(N)\big) + \sum_{k=0}^{N-1} g_D(x(k), u(k)) \tag{3.4}$$

Recurrence relation for Equations 3.3 and 3.4 can be derived [21], which also summarizes the dynamic programming approach. Control that minimizes objective function at time step N-k for a state is formulated as

$$J^*_{N-K,\ N}\big(x(N-k)\big) = \min_{u(N-k)} \left\{ g_D\big(x(k), u(k)\big) + J^*_{N-K+1,\ N}(a_D(x(N-k), u(N-k))) \right\} \tag{3.5}$$

In order to apply recurrence relation to an optimal control problem, system states and admissible controls must be quantized. If there are systems states are quantized into M discrete values, optimal control matrix with size N x M is calculated in a backwards fashion, starting from the final state, through Equation 3.5.

3.2 Optimal Control Problem in SHEV

Optimal control problem for a series HEV can be presented as follows, where battery losses due to time constant resistors are neglected.

$$\dot{x}(t) = \dot{SOC}(t) = \frac{1}{C_{cap}} \frac{V_{OC}\, i_{bat}}{V_{OC} + i_{bat}.R_s} \tag{3.6}$$

$$J(u) = \frac{E_{nom}}{\eta_{charging}\eta_{grid}} \left(SOC(t_f) - SOC(t_0)\right) + \int_0^{t_f} \frac{P_{RE}}{\eta(P_{RE})}\, dt \tag{3.7}$$

Where $\eta_{charging}$ is the charging efficiency, η_{grid} is the average grid efficiency for electricity generation, E_{nom} is the nominal energy of the battery, C_{nom} is the nominal charge of the battery, P_{RE} is the requested power from RE, $\eta(P_{RE})$ is the overall efficiency of the RE.

Final state cost is a function of difference between initial and final SOC times, which is weighted according to grid and charging efficiency. Cost to go is defined as the power requested from RE divided by overall efficiency of the RE.

Using Equations 3.6 and 3.7, discrete state and cost functions can be derived as follows:

$$x(k+1) = SOC(k+1) = SOC(k) - \frac{V_{OC} - \sqrt{{V_{OC}}^2 - 4\,R_s P_{bat}}}{2R_s C_{nom}} \tag{3.8}$$

Where $P_{bat} = P_{RE} - P_{EM}$ and $u(k) = P_{RE}(k)$,

$$J = C_{eq}\left(SOC(N) - SOC(0)\right) + \sum_{k=0}^{N-1} g_D(SOC(k), P_{RE}(k), P_{EM}(k)) \tag{3.9}$$

Selection of C_{eq} indicates importance of the final SOC level. If it is chosen too small, RE will not operate unless state limits are reached. If it is too high, RE will try to overcharge the battery. It can be done according to CO_2 emissions, electricity generation efficiency or even price of the grid electricity. Pseudo code is given below.

for *k = N to 1* **do**
  for *i = 1 to M* **do**
    $VOC_{N-k} \leftarrow VOC(SOC_{N-k+1})$ // update parameters of the battery
    $Rs_{N-k} \leftarrow Rs(SOC_{N-k+1})$
    for *j = 1 to U* **do**
      $SOC_{N-K} \leftarrow f(SOC_{N-k+1}, Pre_j, Pem_{N-k})$
      $G_{N-k,\,j} \leftarrow G(SOC_{N-k}, Pre_j)$
      Interpolate $J^*_{N-k+1,\,N}$
      $J_{N-k,\,N} \leftarrow G_{N-k,\,j} + J^*_{N-k+1,\,N}$
      if $J_{N-k,\,N} < COSTMIN_{N-k,\,M}$ **then**
        $COSTMIN_{N-k,\,M} \leftarrow J_{N-k,\,N}$ // Minimum cost is set to new value
        $U\_OPT_{N-k,\,M} \leftarrow Pre_j$
      end if
    end for
  end for
end for

Figure 3.1. Dynamic Programming algorithm applied to SHEV.

Another equivalent cost function can be formed as in Equation 3.10. Power losses of drive train after inverter cannot be controlled. Hence instead of minimizing overall energy consumption, we can minimize power loss induced in RE and battery.

$$J(u) = \frac{E_{nom}}{\eta_{charging}\eta_{grid}}\left(SOC(t_f) - SOC(t_0)\right) + \int_0^{t_f} P_{RE_{loss}} + P_{bat_{loss}}\, dt \tag{3.10}$$

4. SIMULATION RESULTS AND CONCLUSION

In order to evaluate performance of the optimal controller proposed in 3rd chapter, vehicle model is simulated with a simple controller first. Controller is an on-off controller with a single operating point supplying 25 kW of power. Simple hysteresis logic is constructed such that RE starts to operate if SOC level falls below 0.24 and stops working if SOC level goes above 0.26. Complete vehicle model is shown in Figure 4.1. Simulation results are given in Figures 4.3 to 4.7.

Vehicle control logic is updated for simulating optimal control as shown in Figure 4.2, optimal controller operates offline so reference power for RE is input to the model. Results of the simulation can be found in Figures 4.8 to 4.12.

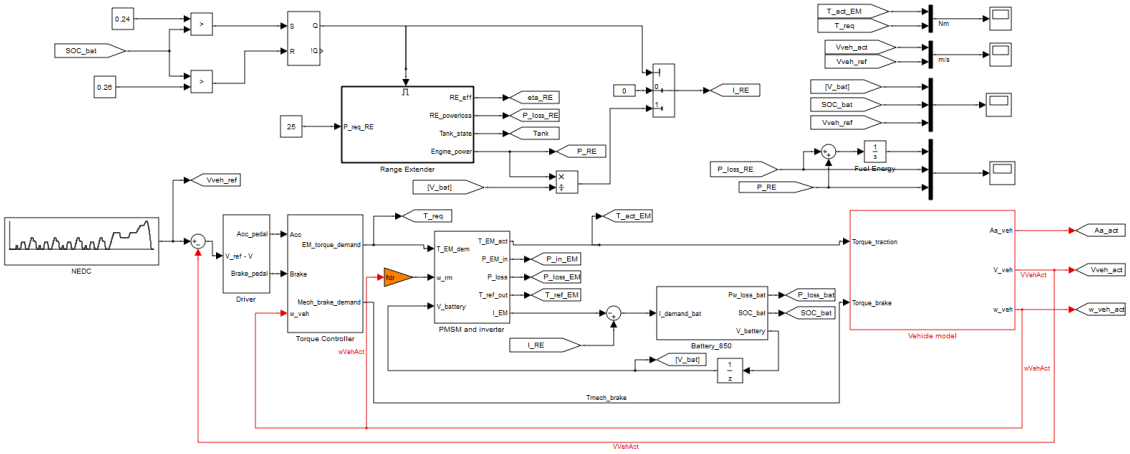

Figure 4.1. Overview of the SHEV model in Simulink with hysteresis on/off control.

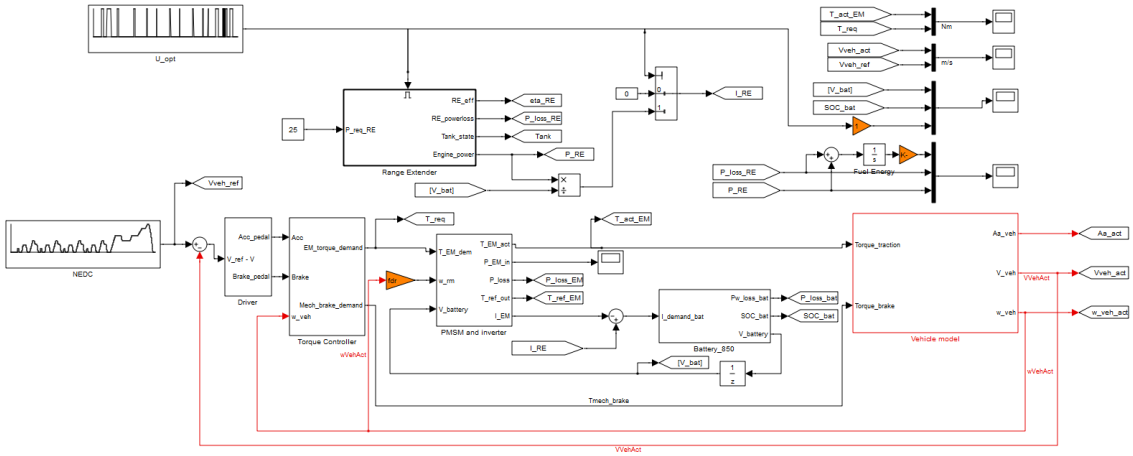

Figure 4.2. Overview of SHEV model in Simulink with offline optimal control input.

4.1 Simulation Results for On/Off Hysteresis Controller

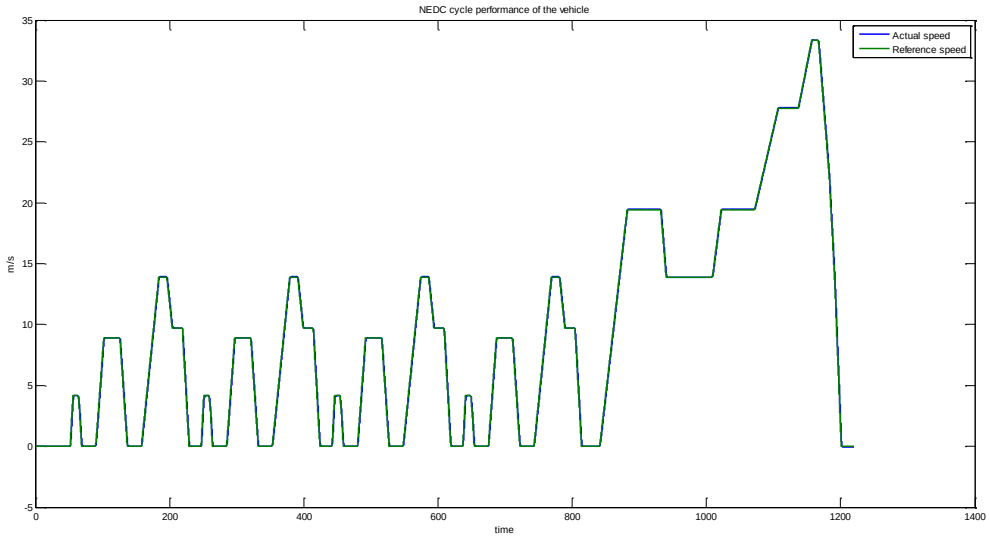

Figure 4.3. NEDC reference and actual speed.

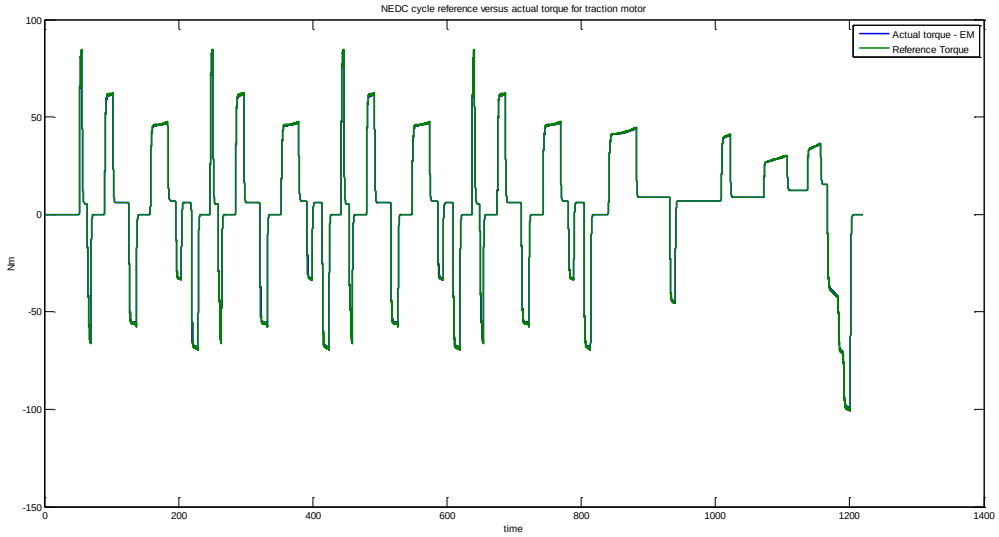

Figure 4.4. NEDC reference torque and actual torque of IPM.

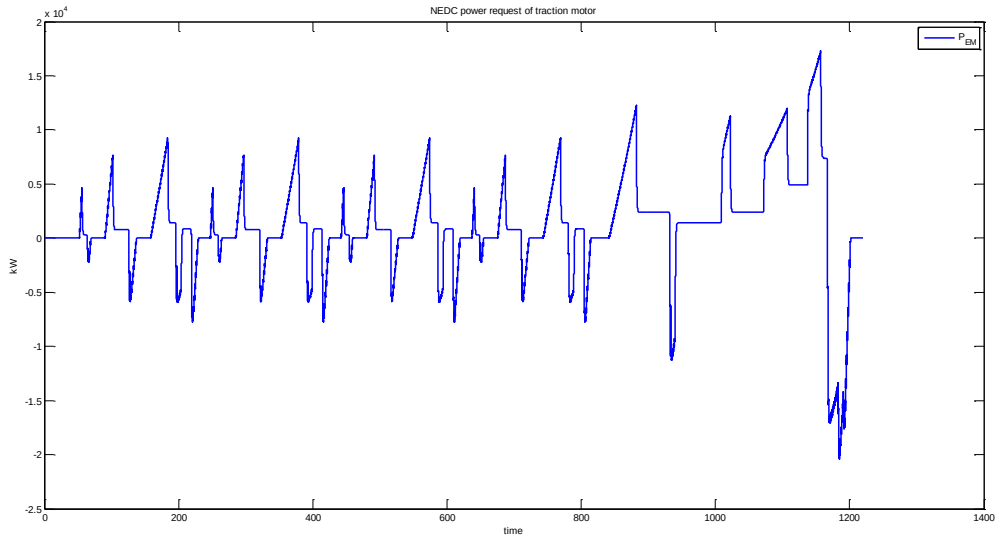

Figure 4.5. Power demand of electric motor (IPM) during NEDC.

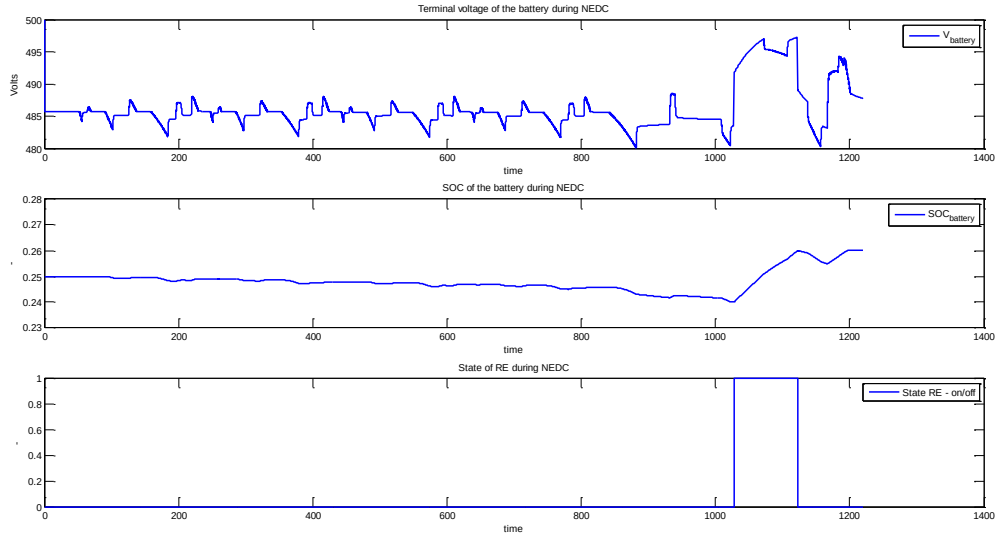

Figure 4.6. Battery SOC and voltage during NEDC.

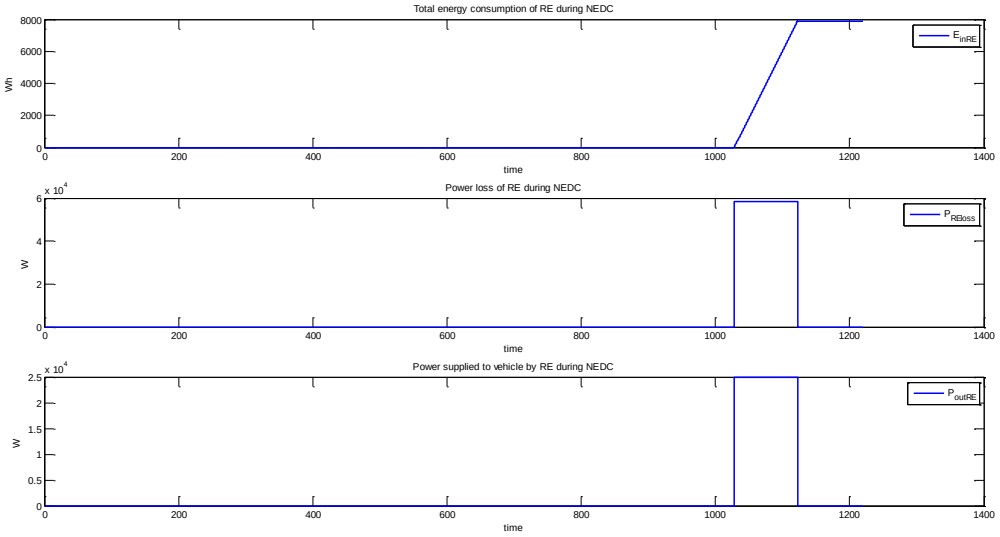

Figure 4.7. Range Extender behavior for simple on-off hysteresis controller. On limit is 0.24 and off-limit is 0.26. From top to bottom: total energy consumption, power loss and output power of Range Extender.

Cumulative cost is simulated as 7.87 using vehicle simulation with hysteresis on/off controller. Cost can be decreased by lowering the hysteresis gap. However it will lead too much engine start-stop, which may cause ICE wear-off. Also emissions are always higher during start and warm-up cycles. A time threshold may also be defined instead of SOC

threshold. A minimum time limit for engine on and engine off state, which means engine cannot be stopped for some time if it has just started working or engine cannot start working for some time if it has just stopped.

4.2 Simulation Results for Offline Optimal Controller

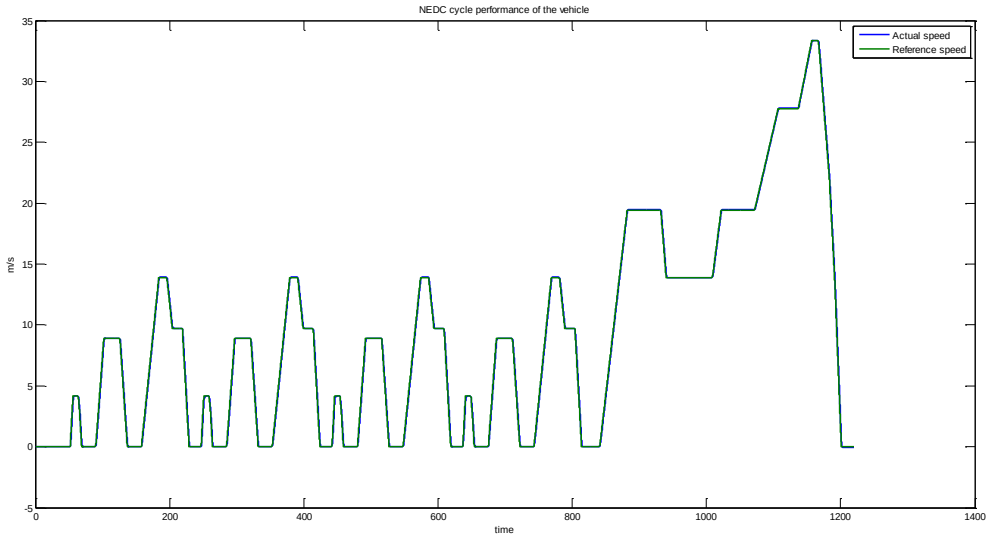

Figure 4.8. NEDC reference and actual speed, optimal controller.

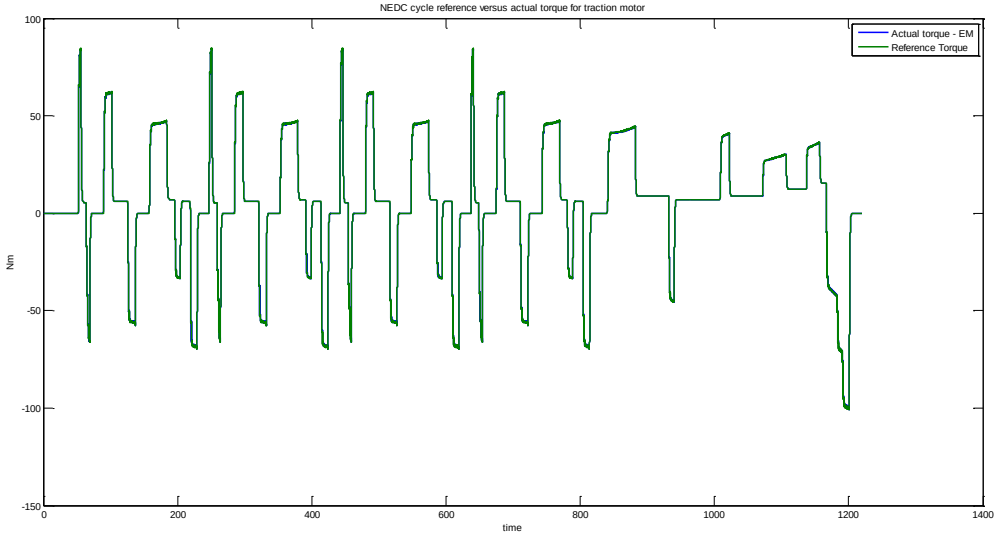

Figure 4.9. NEDC reference torque and actual torque of IPM, optimal controller.

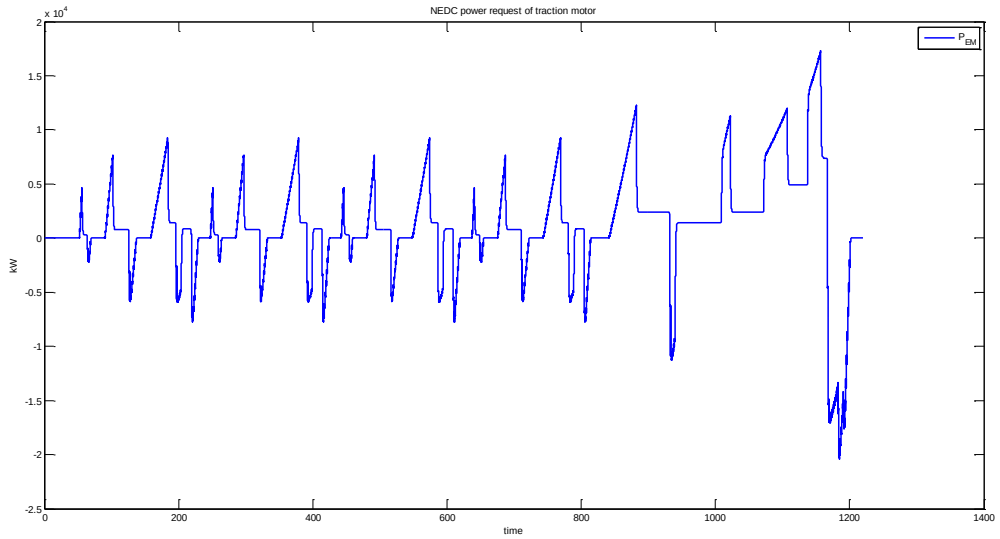

Figure 4..10. Power demand of electric motor (IPM) during NEDC, optimal controller.

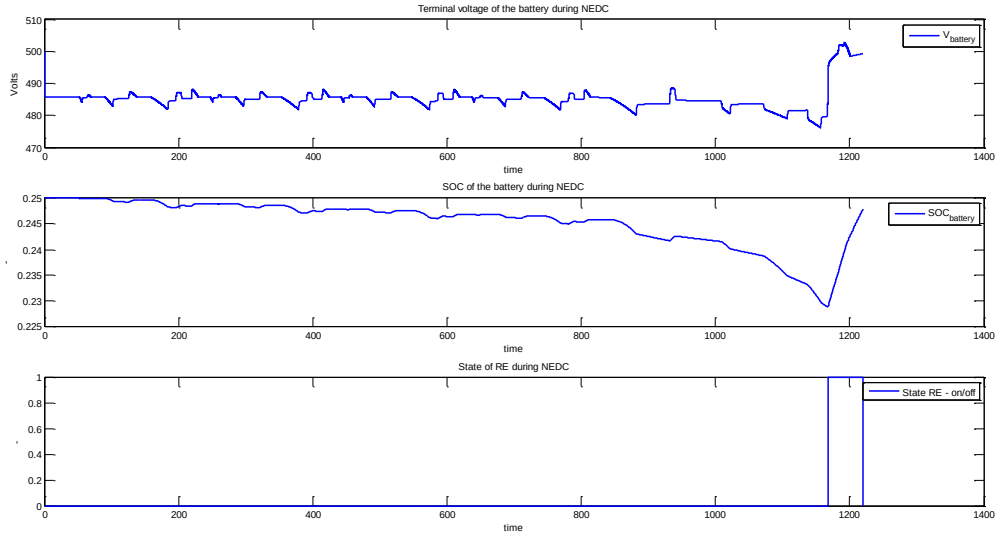

Figure 4.11. Battery voltage and SOC during NEDC when optimal controller is active.

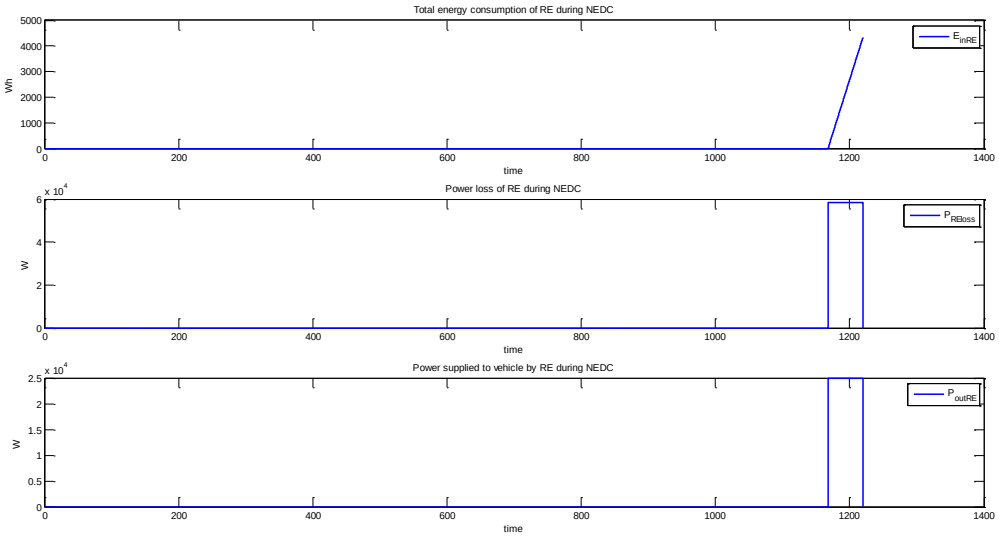

Figure 4.12. From top to bottom RE total energy consumption, power loss and output power during NEDC when optimal controller is used.

Cumulative cost is simulated as 4.34 according using vehicle model with optimal controller. As expected the energy consumption decreased significantly. However performance of the optimal controller can be further increased if fuel equivalence factor is optimized. Resolution of dynamic programming shall be increased for improving the performance.

Including the losses caused by battery time constant resistors in supervisory controller may also increase the performance, since optimal controller will be able to capture time period in which high power is demanded by traction motor.

4.3 Conclusion

Main issue with the application of dynamic programming to energy management problem of the SHEV is that recurrence relation given by Equation 3.5 is actually intended for time-invariant systems. However our cost to go equation given by Equation 3.9 depends on power request of the traction motor at the time, which has no relationship to previous state or control. The power demand introduces time invariance, which acts as a disturbance. Even though results of dynamic programming show significant improvements in fuel economy, global optimality cannot be guaranteed.

Global optimality can be guaranteed when speed of the vehicle constant, since power demand of the traction motor can be removed from the cost function in that case. For a global optimal solution, dynamic programming methods for time-invariant systems shall be employed. This may be addressed as a follow-up study along with addition of switching costs. Addition of switching cost, turning ICE on or off, to optimal control problem will be another follow-up study.

Further study on construction of drive cycle from GPS, GIS and traffic should be made in order to adjust the proposed controller to real world applications. If driver wishes to enter the destination, drive cycle can be constructed and proposed offline optimal control strategy can be applied.

Even though energy management is an important issue, component life especially battery life is a more pressing issue. Proposed optimal control strategy can be applied for protection of battery life and energy management at the same time. Objective function shall be adjusted in a way to penalize battery abuse. Including terms in objective function for protecting ICE and power electronics along with battery can even be a better solution. However weighting the functions will require a lot of data and statistical study.

APPENDIX A: MODEL

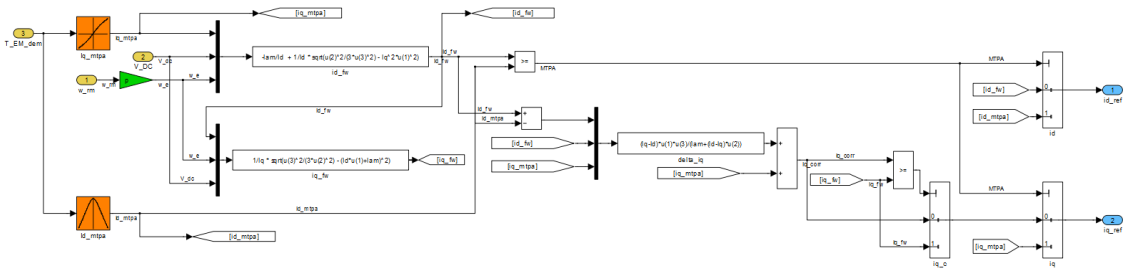

Figure A.1. MTPA &MTPF control.

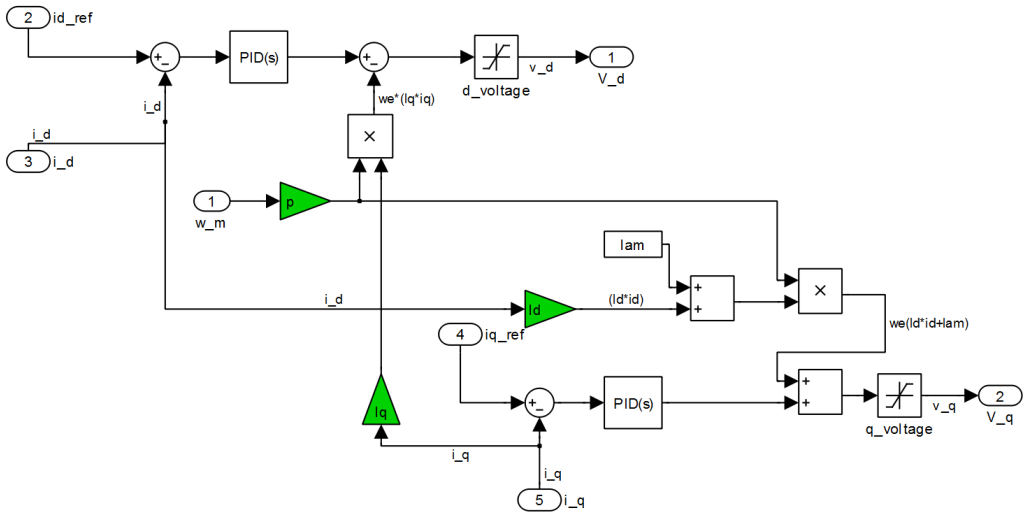

Figure A.2. PI controller with decoupling.

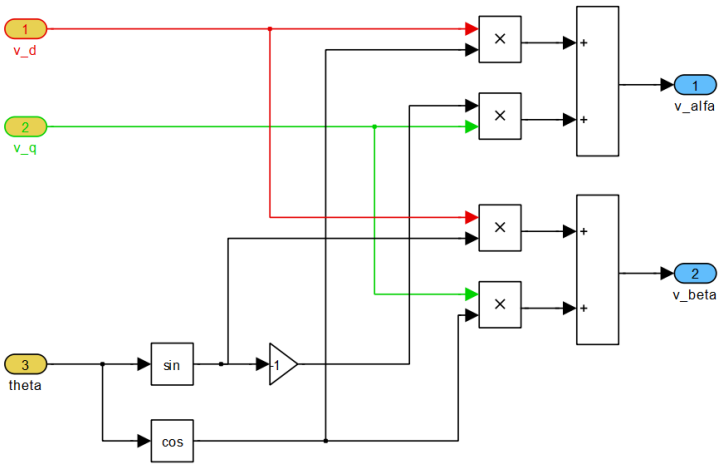

Figure A.3. Inverse Park transformation.

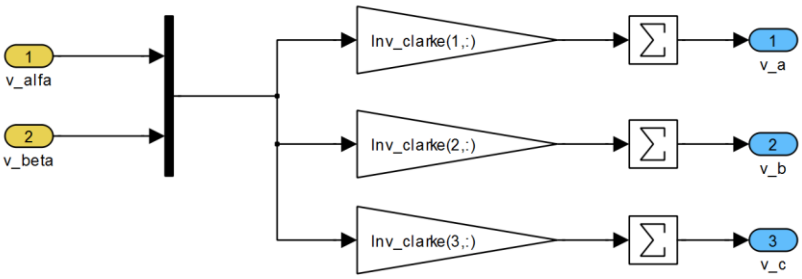

Figure A.4. Inverse Clarke transformation.

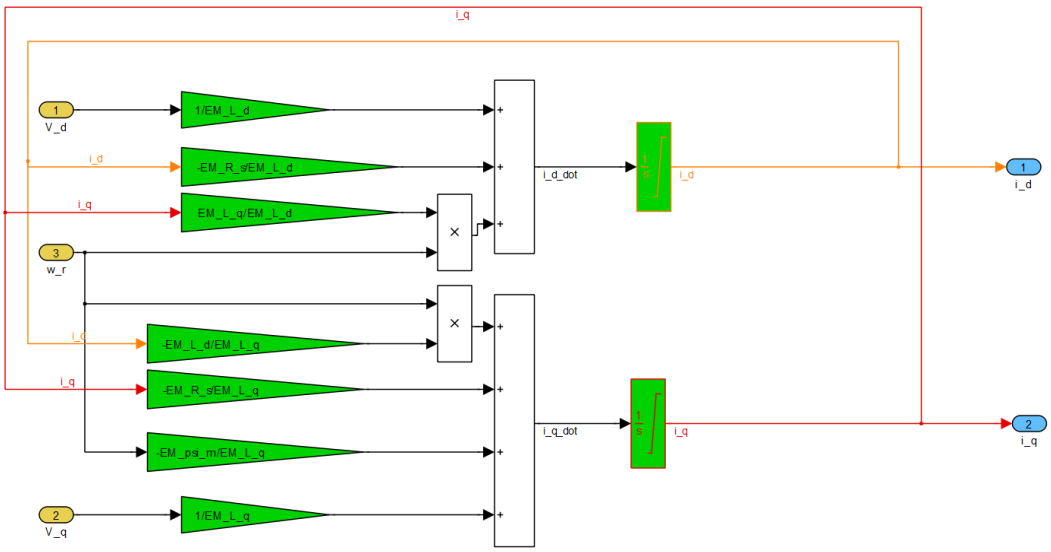

Figure A.5. Inside of PMSM model.

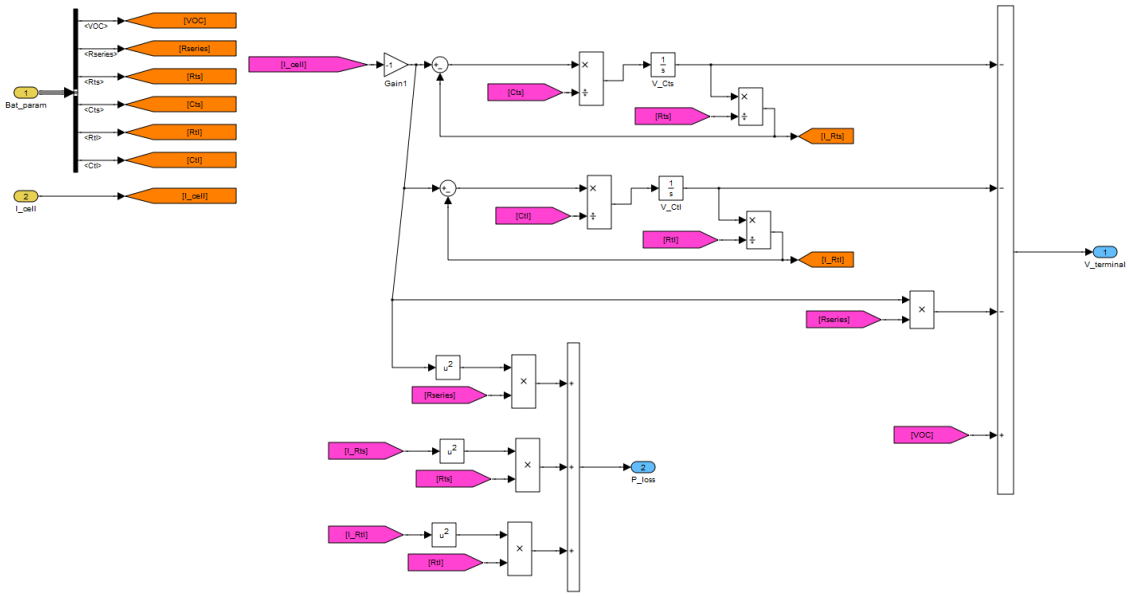

Figure A.6. Inside of battery transients block.

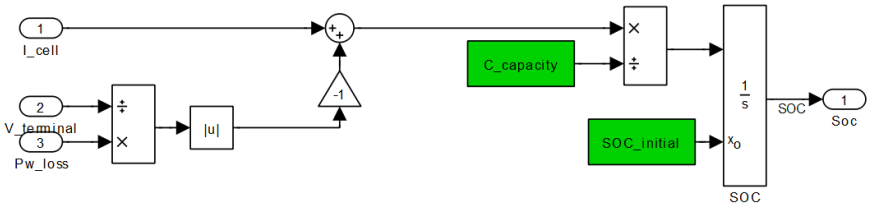

Figure A.7. Inside of battery SOC block.

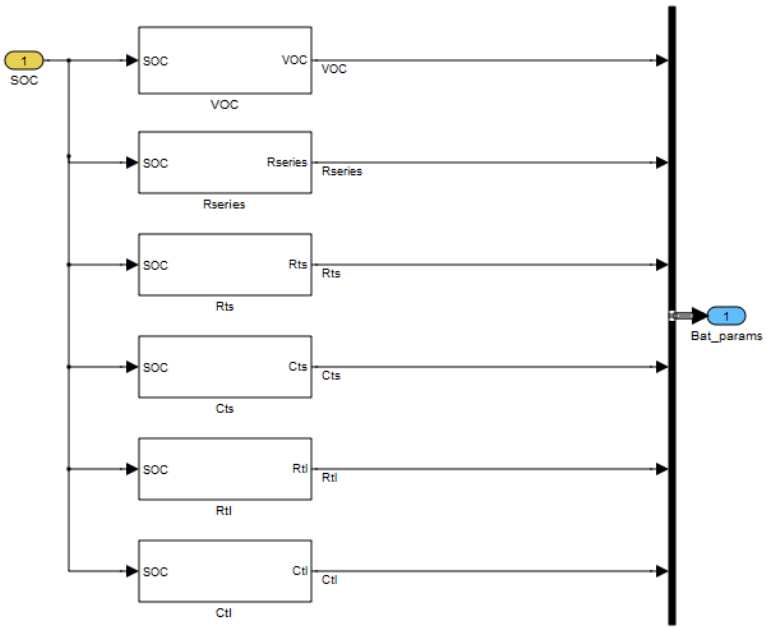

Figure A.8. Inside of battery parameters 850mAh – data from [13]

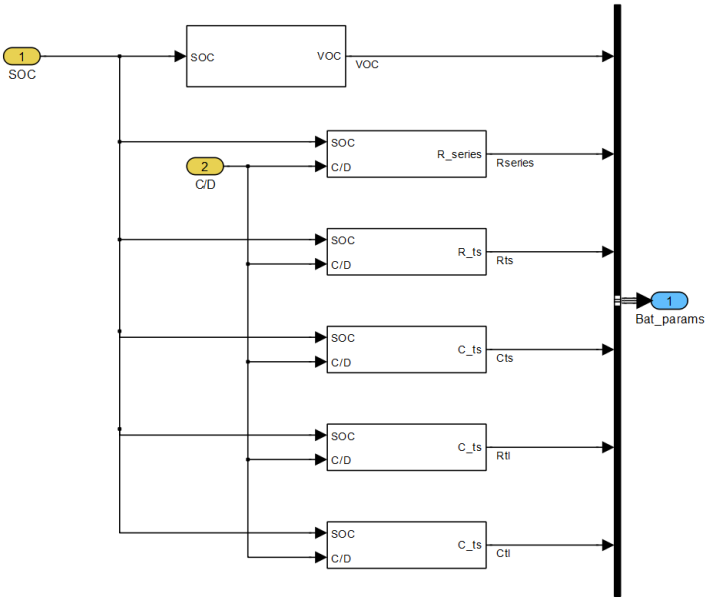

Figure A.9. Inside of battery parameters 2200mAh – data from [17].

REFERENCES

1. Environmental Protection Agency, *Inventory of U.S. Greenhouse Gas Emissions and Sinks*, CRC press, Washington, U.S., 2008.
2. Ehsani, M., Y. Gao, A. Emadi, *Modern Electric, Hybrid Electric and Fuel Cell Systems*, CRC press, Florida, 2010.
3. Guzzella, L., A. Amstutz, *QSS Toolbox Manual*, IMRT press, Zurich, 2005.
4. Stockar, S., V. Marano, M. Canova, G. Rizzoni, L. Guzzella, "Energy-Optimal Control of Plug-in Hybrid Electric Vehicles for Real-World Driving Cycles," *Vehicular Technology, IEEE Transactions on* , Vol. 60, No. 7, pp. 2949-2962, 2011.
5. Sciarretta, A., M. Back, L. Guzzella, "Optimal Control of Parallel Hybrid Electric Vehicles," *Control Systems Technology, IEEE Transactions on*, Vol. 12, No. 3, pp. 352- 363, 2004.
6. Qiuming, G., L. Yaoyu, P. Zhong-Ren, "Trip-Based Optimal Power Management of Plug-in Hybrid Electric Vehicles," *Vehicular Technology, IEEE Transactions on,* Vol. 57, No. 6, pp. 3393-3401, 2011.
7. Guzzella, L., A. Sciarretta, *Vehicle Propulsion Systems*, Springer, Zurich, Switzerland, 2005.
8. Ripaccioli, G., D. Bernardini, S. Di Cairano, A. Bemporad, I.V. Kolmanovsky, "A Stochastic Model Predictive Control Approach for Series Hybrid Electric Vehicle Power Management," *American Control Conference*, pp. 5844-5849, 2010.
9. *Lithium-ion battery*, 2009, http://en.wikipedia.org/wiki/Lithium-ion_battery, accessed at April 2012.
10. Iqbal, H., *Electric and Hybrid Vehicles Design Fundamentals*, CRC press, Florida, U.S., 2005.
11. Miller, J. M., *Propulsion Systems for Hybrid Vehicles*, IEE press, Cornwall, UK, 2003.
12. Grunditz, E., E. Jansson, *Modeling and Simulation of a Hybrid Electric Vehicle for Shell Eco-marathon and Electric Go-kart*, M.S. Thesis, Chalmers University of Technology, Sweden, 2009.

13. Min, C., G.A. Rincon-Mora, "Accurate Electrical Battery Model Capable of Predicting Runtime and I-V Performance," *IEEE Transactions on Energy Conversion* , Vol. 21, No. 2, pp. 504- 511, 2006.
14. Knauff, M.C., C.J. Dafis, D. Niebur, H.G. Kwatny, C.O. Nwankpa, "Simulink Model for Hybrid Power System Test-bed," *Electric Ship Technologies Symposium, ESTS '07. IEEE*, pp. 421-427, 2007.
15. Duong, Q., T. Richardson, *USABC Goals for Advanced Batteries for EVs*, U.S. Department of Energy, Washington D.C., 2009.
16. Gerssen-Gondelach, S. J., A.P.C. Faaij, "Performance of Batteries for Electric Vehicles on Short and Longer Term", *Journal of Power Sources*, Vol. 212, pp. 111-129, 2012.
17. Kroeze, R.C., P.T. Krein, *Electrical Battery Model for Use in Dynamic Electric Vehicle Simulations*, M.S. Thesis, University of Illinois, 2005.
18. Tallner, C., S. Lannetoft, *Batteries or Supercapacitors as Energy Storage in HEVs*, M.S. Thesis, Lund University, 2005.
19. *Digital Signal Processing Solution for Permanent Magnet Synchronous Motor*, TI Press, Austin, Texas, 1997.
20. *Electric Motor*, 2008, http://en.wikipedia.org/wiki/Electric_motor, accessed at May 2012.
21. Kirk, D.E., *Optimal Control Theory an Introduction*, Dover Publications, New York, 2004.
22. Morimoto, S., Y. Takeda, T. Hirasa, K. Taniguchi, "Expansion of Operating Limits for Permanent Magnet Motor by Current Vector Control Considering Inverter Capacity", *IEEE Transactions on Industry Applications*, Vol. 26, No. 5, pp. 886, 1990.
23. Kirtley, J.L., *Permanent Magnet Brushless DC Motors*, 6.685 Electric Machines Class Notes 7, Massachusetts Institute of Technology, Boston, 2005.
24. Chapman, P.L., *Permanent Magnet Synchronous Machine Drives Power Electronics Handbook*, CRC press, U.S., 2002.
25. Krishnan, R., *Electric Motor Driver*, Prentice Hall, New Jersey, 2001.
26. Ohm, D.Y., *Dynamic Model of PM Synchronous Motors*, 1997, http://www.drivetechinc.com/articles/IM97PM_Rev1forPDF.pdf, accessed at April 2012.

27. *3-Phase PM Synchronous Motor Vector Control Using a 56F80x, 56F8100, or56F8300 Device*, Freescale semiconductor, Austin, Texas, 2005.
28. Wu, T., *dq Theory for Permanent Magnet Synchronous Machine (PMSM)*, 2009, http://www.eecs.ucf.edu/~tomwu/course/eel6208/notes, accessed at May 2012.
29. Luukko, J., *Direct Torque Control of Permanent Magnet Synchronous Machines – Analysis and Implementation*, Ph.D. Thesis, University of Lappeenranta, 2000.
30. Meyer, M., J. Bocker, "Optimum Control for Interior Permanent Magnet Synchronous Motors (IPMSM) in Constant Torque and Flux Weakening Range," *Power Electronics and Motion Control Conference, EPE-PEMC 2006. 12th International*, pp. 282-286, 2006.
31. Gusyev, I., *Maximum Torque Per Ampere Control with Optimal Field Weakening Strategy for Torque, Speed and Voltage Control of Interior Mounted Permanent Magnet Synchronous Motor*, 2009, http://www.nbuv.gov.ua/portal/natural/Ikszt-/2009_5/5_2009_7.pdf , accessed at April 2012.
32. Capitan, C., *Torque Control in Field Weakening Mode, Institute of energy technology*, M.S. thesis, Aalborg University, 2009.
33. *Four Quadrant Motion Control of a Motor*, 2007, http://en.wikipedia.org/wiki/File-Four_quadrant_motion_control_of_a_motor.jpg, accessed at May 2012.
34. Alakula, M., *Modulation of 3-phase converters*, M.S. Thesis, Industrial Engineering and Automation Lund University, Sweden, 2012.
35. Gajdusek, P., *Programmable Laboratory Inverter and Space Vector PWM*, Ph.D. Thesis, Dept. of Electrical Power Engineering, FEEC, VUT, 2005.
36. Quattrochi, D., *Internal Combustion Engines*, 2006, http://web.mit.edu/16.unified/-www/SPRING/propulsion/notes/node25.html, May 2012.
37. Guzzella, L., C.H. Onder, *Introduction to Modeling and Control of Internal Combustion Engine Systems*, Springer, Berlin, 2010.